Development and Applications of Advanced Ultrasound Techniques for Characterization and Stimulation of Engineered Tissues

by

Xiaowei Hong

A dissertation submitted in partial fulfillment
of the requirements for the degree of
Doctor of Philosophy
(Biomedical Engineering)
in the University of Michigan
2018

Doctoral Committee:

Professor Cheri X. Deng, Co-Chair
Professor Jan P. Stegemann, Co-Chair
Assistant Professor Rhima Coleman
Professor J. Brian Fowlkes

Xiaowei Hong

xho@umich.edu

ORCID iD: 0000-0002-7833-1665

DEDICATION

To my family: Linghui Hong, Tianbo Hong, Xiaofang Hong and Mingxin Hong

For all their love and support

ACKNOWLEDGEMENTS

I would like to first express my deepest gratitude towards to my thesis advisers, Professors Cheri X. Deng and Jan P. Stegemann. I cannot thank you enough for supporting and guiding me through my doctoral training with so much patience and care. Both of you have showed so much trust towards me and so much enthusiasm towards my work. You have said so many kind words to me that kept me motivated and got me through difficult times. Thank you for giving me the opportunity to build my skills, showing genuine care towards my future career and helping me build connections. I am so blessed to have both of you as my mentors and I would not have accomplished nearly as much without you.

Beside my advisers, I would also like to thank the rest of my thesis committee, Professors J. Brian Fowlkes and Rhima Coleman, for showing genuine interests in my work, taking time to meet with me, answering my questions, and giving me valuable feedback that has really strengthened my dissertation and inspired the future work.

I am also extremely grateful to have so many amazing collaborators, Dr. Benjamin Levi, Dr. Kavitha Ranganathan, Dr. Gustavo Rosania, Dr. Frank M. Bogun, Dr. Jianping Fu, Grace Bushnell, Xufeng Xue, Phillip Rzeczycki, who have brought so much fun and positive energy into my work. All of you have been so inspiring and thank you for all the knowledge you shared with me. It was a great pleasure to work with you and thank you for making my research experience so much more enjoyable.

I sincerely thank everyone in the Cell-Matrix Interactions & Tissue Engineering (CMITE) Laboratory and the Deng Laboratory. To Kelly Carnahan, Dr. Ram Rao, Dr. Joel Wise, Dr. Yi-

Sing Hsiao, Dr. Madhu Gudur, thank you for getting me started in the lab and sharing your knowledge and experience. To Ana Rioja, Brandan Walters, Dr. Ethan Daley, Dr. Paul Turner, Dr. Ramkumar TA, Dr. Zhenzhen Fan, Tugba Topal, Tyler Kemerer and Eric Hobson, I really enjoyed our discussions and there are so much that I want to learn from you. Thank you for helping me along the way and keeping me accompanied.

I am also very thankful to the Therapeutic Ultrasound group and all the staff in Biomedical Engineering Department, especially Kathleen McCrumb, Maria Steele, Chuck Nicholas and Dana Jackson. You have always been there when I needed your help, and I absolutely enjoy our conversations. To Dr. Zhen Xu, thank you for generously sharing your knowledge and personal experience.

Finally, to the most important people in my life, my family, I would not have made it so far without your support and encouragement. I am truly sorry for the limited time I could spent with you, even at difficult times. Thank you for understanding me and supporting me unconditionally. To my parent, even though you may never read this nor can you understand English, having you as my parents is the most fortunate thing in my life.

TABLE OF CONTENTS

LIST OF FIGURES

LIST OF TABLES

LIST OF APPENDICES

LIST OF ABBREVIATIONS

(Symbols, Numerical Order, Alphabetical Order)

°C	Celsius
2D	Two-dimensional
3D	Three-dimensional
AAC	Average acoustic concentration
AG	Agarose
ALP	Alkaline phosphatase
A-mode	Amplitude mode
ANOVA	Analysis of variance
ARF	Acoustic radiation force
ARFI	Acoustic radiation force impulse
ASD	Average scatterer diameter
B/T	Burn Injury/Achilles Tenotomy
B-mode	Brightness-mode
COL/FIB	Collagen/fibrin
CT	Computed tomography
DEX	Dexamethasone
DMEM	Dulbecco’s modified Eagle’s medium-low glucose
DUE	Dual-mode ultrasound elasticity
ECM	Extracellular matrix
FBS	Fetal bovine serum
FDA	Food and Drug Administration
FPAS	Focused Pulsed Acoustic Straining
FUS	Focused ultrasound
GAG	Glycosaminoglycan
GM	Growth medium

GS	Grayscale
H&E	Hematoxylin and eosin
HA	Hydroxyapatite
HIFU	High intensity focused ultrasound
hMSC	Human mesenchymal stem cell
HO	Heterotopic ossification
IBC	Integrated backscatter coefficient
IVUS	Intravascular ultrasound
LIPUS	Low intensity pulsed ultrasound
LOS	Line of sight
MBF	Mid-band fit
M-mode	Motion mode
MSC	Mesenchymal stem cell
MSSER	Steady-state excitation and recovery
MUVE	Multimode ultrasound viscoelastography
NAOH	Sodium hydroxide
OCPC	Orthocresolphthalein complex one
OM	Osteogenic medium
P/S	Penicillin and streptomycin
PBS	Phosphate buffered saline
PDMS	Polydimethylsiloxane
PRF	Pulse repetition frequency
QUS	Quantitative ultrasound
RF	Radio-frequency
ROI	Region of interest
SATA	Spatial average temporal average
SUSI	Spectral ultrasound imaging
UEI	Ultrasound elasticity imaging
β-GP	Beta-glycerol phosphate

ABSTRACT

Mechanobiology is central in the development, pathology, and regeneration of musculoskeletal tissues, in which mechanical factors play important roles. Therefore, there is a need for methods to characterize the composition and mechanical properties of developing musculoskeletal tissues over time. Ultrasound elastographic techniques have been developed for noninvasive imaging of spatial heterogeneity in tissue stiffness. However, their application for quantitative assessment of tissue mechanical properties, especially viscoelastic properties, has not been exploited. Additionally, ultrasound energy may be used to apply mechanical stimulation to engineered constructs at the microscale, and thereby to enhance tissue regeneration.

We have developed a multimode ultrasound viscoelastography (MUVE) system for assessing microscale mechanical properties of engineered hydrogels. MUVE uses focused ultrasound pulses to apply acoustic radiation force (ARF) to deform samples, while concurrently measuring sample dimensions using coaxial high frequency ultrasound imaging. We used MUVE to perform creep tests on agarose, collagen, and fibrin hydrogels of defined concentrations, as well as to monitor the mechanical properties of cell-seeded constructs over time. Local and bulk viscoelastic properties were extracted from strain-time curves through fitting of relevant constitutive models, showing clear differences between concentrations and materials. In particular, we showed that MUVE is capable of mapping heterogeneity of samples in 3D. Using inclusion of dense agarose microbeads within agarose, collagen and fibrin hydrogels, we determined the spatial resolution of MUVE to be approximately 200 μm in both the lateral and axial directions. Comparison of MUVE to nanoindentation and shear rheometry showed that our ultrasound-based

technique was superior in generating consistent, microscale data, particularly for very soft materials.

We have also adapted MUVE to generate localized cyclic compression, as a means to mechanically stimulate engineered tissue constructs at the microscale. Selected treatment protocols were shown to enhance the osteogenic differentiation of human mesenchymal stem cells in collagen-fibrin hydrogels. Constructs treated at 1 Hz at an acoustic pressure of 0.7 MPa for 30 minutes per day showed accelerated osteogenesis and increased mineralization by 10 to 30 percent, relative to unstimulated controls. In separate experiments, the ultrasound pulse intensity was increased over time to compensate for changes in matrix properties over time, and a 35 percent increase in mineralization was achieved.

We also extended the application of a previously-developed spectral ultrasound imaging (SUSI) technique to an animal model for early detection of heterotopic ossification (HO). The quantitative information on acoustic scatterer size and concentration derived from SUSI was used to differentiate tissue composition in a burn/tenotomy mice model from the control model. Importantly, HO foci were detected as early as one week after injury using SUSI, which is 3-5 weeks earlier than when using conventional micro-computed tomography.

Taken together, these results demonstrate that ultrasound-based techniques can non-invasively and quantitatively characterize viscoelastic properties of soft materials in 3D, as well as their composition over time. Ultrasound pulses can also be used to stimulate engineered constructs to promote musculoskeletal tissue formation. MUVE, SUSI, and ultrasound stimulation can be combined into an integrated system to investigate the roles of matrix composition, static mechanical environment, and dynamic mechanical stimuli in tissue regeneration, as well as the interactions of these factors and their evolution over time. Ultrasound-based techniques therefore

have promising potential in noninvasively characterizing the composition and biomechanics, as well as providing mechanical intervention in native and engineered tissues as they develop over time.

Chapter 1 Introduction

1.1 Background and Motivation

Since its emergence, tissue engineering has been an important field for developing biological alternatives to restore, replace or regenerate defective tissues. In tissue engineering, a scaffold analogous to extracellular matrix (ECM) in natural tissue is required to provide structural support and physical environment for cell adhesion and tissue development [1, 2]. With the development of tissue engineering, multiple approaches for scaffolding have been developed. Among them, cell encapsulated self-assembled hydrogel matrix has shown several advantages over other approaches and has wide applications for soft tissues since it provides an environment for more intimate cell-matrix interactions, and involves an simple fabrication and implantation procedure [3-6]. Other than the development of scaffold synthesis, a subfield of functional tissue engineering has grown, and increasing attention has been focused on incorporating biomechanical functions into engineered tissue constructs [7, 8]. It has become evident that the mechanobiological interactions between cells and scaffolds have significant impact on cell fate and function. In particular, the viscoelastic mechanical properties have recently been shown to be a determining factor in cell function and differentiation [9, 10]. In addition to the passive mechanical environment, external mechanical load also plays a critical role in tissue development and regeneration. Mechanical stimulation in various forms including tension, compression, fluid flow, vibration and microgravity have been shown to influence cell differentiation and tissue

regeneration and cyclic strain has been found to enhance osteogenic differentiation of stem cells [11-19]. On the hand, lack of mechanical stimulation can lead to cell apoptosis and loss of tissue function [20]. Therefore, there is a clear need for methods that can characterize of the mechanical properties, especially viscoelastic properties, of native tissue and engineered scaffolds and techniques that can provide dynamic mechanical stimulation for engineered tissue constructs. Despite the availability of some conventional mechanical testing and stimulation methods, these methods usually involve direct contact with the samples, which limits their applications *in vivo*.

Ultrasound has now become a powerful tool for diagnostic and therapeutic applications in regenerative medicine. As an imaging tool, ultrasound has mostly been used for real-time noninvasive diagnostic imaging. As ultrasound propagates through a material, reflected radio-frequency (RF) signal is generated when encountering mismatch in acoustic impedance. A single scan line showing the pulse-echo signals as a function of depth forms the amplitude mode (A-mode) ultrasound. Brightness-mode (B-mode) ultrasound is currently most widely used in diagnostic imaging and it provides two-dimensional gray-scale images. Volumetric and motion mode (M-mode) imaging can be also obtained from a series of scan lines in spatial or time domain [21, 22]. Based on these fundamental imaging modes, quantitative ultrasound for tissue and scaffolds characterization is in rapid development. To measure tissue mechanical properties noninvasively and nondestructively, ultrasound elastography techniques have been developed [23] and applied to assess variations in local tissue properties and change in tissue stiffness to detect tumor and evaluate response to therapies [24-26]. For therapeutic purposes, ultrasound has been commonly used in physiotherapy and lithotripsy procedures for tissue fragmentation. Moreover, a variety of tissue stimulation techniques have been developed to enhance tissue development and regeneration. A most studied and widely used ultrasound stimulation method is low intensity

pulsed ultrasound (LIPUS), which has been shown to accelerate fracture healing and treat nonunion by applying pulsed ultrasound with intensity in between diagnostic and fragmentation-induced-therapeutic ultrasound [27, 28].

Whereas ultrasound elastographic technique and LIPUS have proven advances in mechanical characterization and stimulation, there is still substantial potential in ultrasound that can be exploited for tissue engineering applications. Most applications of ultrasound elastography have been focused on providing information of the relative stiffness in native tissues, leaving the need for a noninvasive mechanical testing system that generates reliable quantitative measurement of viscoelasticity in engineered scaffolds unfulfilled. Additionally, there is also potential for developing a novel noninvasive stimulation technique to leverage benefits from cyclic strain at tissue level using conventional stimulation methods and microscale oscillatory strain with acoustic streaming using LIPUS [29] to further enhance tissue regeneration.

In the following sections, we will discuss established ultrasound-based compositional and mechanical characterization techniques and mechanical stimulation methods using contact forces and non-contact acoustic radiation force.

1.2 Ultrasound Characterization Techniques

Ultrasound imaging typically operates in pulse-echo mode, in which a transducer sends an ultrasound pulse and then receives the backscattered echo signals from the sample under examination. At a fixed location, the time domain echo (A-line) signals provide the locations of acoustic scatterers along the line of sight of the ultrasound pulse, as the signal arrival time from a scatterer is proportional to its distance from the transducer. The amplitudes of the echo signals generally represent the “strength” of the scatterers, which is related to the local acoustic properties. A two dimensional (2D) cross-sectional image, or grayscale B-mode image, is formed from a

collection of A-lines from consecutive locations across a region. A 3D volumetric image can be generated by stacking a set of adjacent 2D images.

The ability of ultrasound to penetrate a wide range of different tissue types and materials makes this technique suitable for noninvasive visualization of the bulk phase of engineered tissues. It is therefore a logical extension to exploit the desirable features of ultrasound imaging in tissue engineering applications. Significant progress has been made in both arenas. Below, we provide an overview of the ultrasound imaging techniques and their applications in tissue engineering.

1.2.1 Compositional Characterization

Grayscale ultrasound imaging for assessment of engineered tissues

Table 1-1 shows a list of representative studies that employed conventional B-mode ultrasound imaging techniques, a number of pioneering studies have used conventional grayscale ultrasound for nondestructive characterization of tissue components and properties in a variety of systems. For example, attenuation of B-mode ultrasound image intensity over time has been shown to correlate with extracellular matrix (ECM) deposition and differentiation of stem cells on 3D synthetic polymer scaffolds [30]. Similarly, grayscale ultrasound imaging has been used to track collagen production by myofibroblasts in 3D fibrin matrices over an 18 day culture time [31], and to characterize cell number in ceramic composites [32]. In addition, acoustic imaging parameters that represent bulk material properties have even been used to assess matrix evolution by chondrocytes in hydrogels over time [33, 34].

Table 1-1. Representative studies employing B-Mode ultrasound imaging for tissue engineering applications

Representative studies	Imaging parameters	Imaging frequency, MHz	References
Evaluation of extracellular matrix deposition and differentiation of stem cells on 3D synthetic polymer scaffolds	Attenuation	40 focused	Fite *et al.*
Tracking of collagen production by myofibroblasts in 3D fibrin matrices over an 18 day culture time	Grayscale ultrasound imaging	13 linear array	Kreitz *et al.*
Characterization of cell number in ceramic composites	Ultrasound amplitude	N/A	Oe *et al.*
Monitoring of cartilaginous matrix evolution in degradable PEG hydrogels	Speed of sound, slope of attenuation	50 and 100	Rice *et al.*
Evaluation of agarose hydrogel mechanical properties	Speed of sound	15	Walker *et al.*

While conventional B-mode ultrasound imaging can provide spatial and temporal information about sample morphology based purely on grayscale values [35], this approach provides little direct information about sample composition. In addition, purely grayscale signal-based analysis is both system- and operator-dependent. The imaging signals are affected by a variety of factors not associated with sample properties. These factors include power level of the input signals, ultrasound transducer response, receiver gain, and imaging/signal algorithms for pre- and post-processing and display. Therefore it is difficult to meaningfully compare the results obtained between ultrasound imaging data taken from different systems or at different times by different operators [36, 37].

Quantitative ultrasound (QUS) imaging for microscale assessment of engineered tissues

Although any ultrasound-based methods, even those based on conventional B-mode imaging, that provide quantitative assessments may be referred as quantitative ultrasound techniques, we here specifically refer only those techniques that derive objective, microscopic information related to local tissue composition and structural details as QUS imaging techniques. QUS imaging techniques are based on the fact that ultrasound propagation and acoustic scattering in tissue or body of material depends on the local variation of acoustic properties, which in turn is

related to tissue microstructure, composition, and other physical properties such as density and compressibility. However, quantitative details of tissue composition are not explicitly apparent from the backscattered signals. Therefore, QUS imaging techniques typically utilize the raw radio-frequency (RF) data of ultrasound backscattered signals to extract objective, quantitative, microscale metrics of tissues. As shown in **Table 1-2**, a number of parameters have been exploited as quantitative estimates of the density, size, and spatial organization of acoustic scatterers in tissue. An important advantage of using raw RF data is the ability to derive results independent of system and operator settings, thereby providing a more objective view of sample characteristics.

QUS imaging has been applied to a broad range of tissue characterization applications (**Table 1-2**), for example, to identify changes in tissue state in prostate, breast, and other cancer [38-40], as well as intravascular plaques [41]. It has also been implemented for monitoring of cell death [42, 43], and assessing therapeutic responses in diseased tissues [44-46]. These successful applications have motivated the exploration of QUS approaches in tissue engineering. In the following sections, we discuss two main QUS techniques, use of the integrated backscatter coefficient (IBC) and spectrum analysis and their application to characterization of engineered tissues.

Table 1-2. Representative studies employing quantitative ultrasound imaging techniques for tissue engineering applications

Representative studies	Imaging parameters	Imaging frequency, MHz	References
Estimation of cell concentration in 3D agarose constructs	Integrated backscatter coefficient	30 and 38	Mercado *et al.*
Assessment of spatial variation in collagen fiber density and diameter in 3D hydrogels	Integrated backscatter coefficient	38	Mercado *et al.*
Spatiotemporal characterization of mineralization in 3D collagen hydrogels	Midband fit and slope	55	Gudur *et al.*
Quantification of osteoblast differentiation in 3D collagen hydrogels	Midband fit, slope, scatterer size, equivalent number of scatterers, relative acoustic impedance	55	Gudur *et al.*

The IBC for tissue characterization

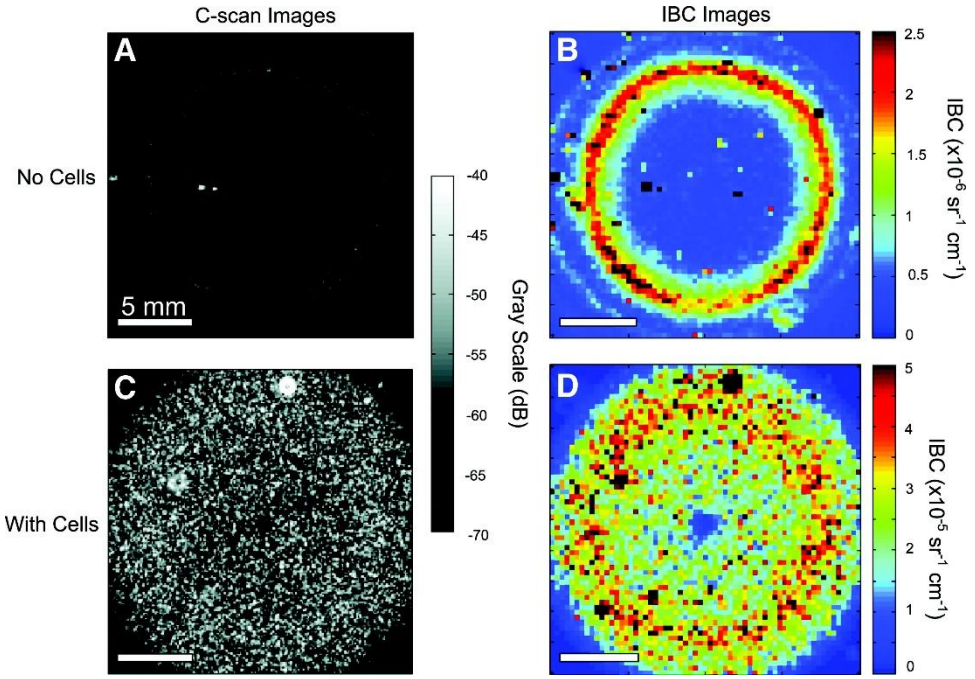

Figure 1-1. (A, B) C-scan and integrated backscatter coefficient (IBC) parametric imaging of acellular and (C, D) cell-seeded collagen gels. Best viewed in *color*. Adapted from Mercado *et al.* and used with permission [51].

One QUS imaging technique uses the IBC for tissue characterization [47]. The IBC is an estimate of the backscattered intensity of the sub-resolution scatterers per unit volume of tissue

under examination over the transducer bandwidth [48]. Although the scatterers are too small to be resolved individually in ultrasound imaging, which typically uses frequencies in the MHz range, the IBC provides a quantitative metric that approximates the scatterer number density [45, 48]. The IBC method can therefore be used to estimate the cell density and spatial distribution in tissue constructs. In a recent study by Mercado *et al.* [49], the IBC, calculated from the measured backscattered RF data in a frequency range of 13 – 47 MHz, was used to non-invasively estimate cell concentration in agarose gels. It was found that the IBC for cell-seeded gels increased linearly as cell density increased, suggesting that IBC values may represent the collective "strength" of the cells serving as acoustic scatterers in the constructs. It was also shown that both the accuracy and precision of IBC estimation improved with increasing region of interest (ROI) dimensions and cell concentration. These results are promising, and were obtained completely non-destructively. While this study examined only one time-point, it served as proof-of-concept that the IBC could be used to monitor cell populations within engineered tissue constructs.

The IBC method has also been extended to characterize collagen-based biomaterials [50], which are widely investigated as scaffolds in tissue engineering. As with cellular characterization, non-invasive techniques capable of visualizing collagen fiber microstructure would greatly aid the development of functional engineered tissues. In acellular collagen gels, the IBC increased linearly with increasing collagen concentration, indicating that collagen can act as an "effective" acoustic scatterer in such constructs. In contrast, collagen gels fabricated at higher polymerization temperature exhibited lower IBC values. Interestingly, IBC parametric images allowed visualization of the spatial variation in collagen distribution caused by the geometry of the gels studied, as shown in **Figure 1-1**. This work demonstrated that IBC analysis can be used to

indirectly examine the microstructure and spatial composition of 3D collagen matrices even in the absence of stronger scatterers such as cells.

Spectrum analysis for tissue characterization

Frequency domain analysis of backscattered RF signals in ultrasound imaging has also been exploited to provide objective, quantitative tissue characterization [35, 36, 51, 52]. In this approach, power spectra of the RF signals from an ROI are computed and calibrated so that the system effects are removed. Instead of obtaining an aggregate parameter such as the integrated IBC, spectrum analysis generates spectral parameters that can provide additional information about the underlying tissue microstructure. As shown in **Table 1-2**, the spectrum analysis technique has been used in various applications, including characterization of plaque composition by intravascular ultrasound (IVUS) [41, 53, 54], lesions induced by high intensity focused ultrasound (HIFU) [55, 56]. Spectral parameters have also shown the ability to identify changes in a tissue state for a number of organ systems including the prostate, pancreas, and lymph node [40, 57, 58].

The technique is based on the fact that spectral characteristics of the backscattered RF data includes information of the "effective" acoustic scatterers in tissue. As these scatterers are generally much smaller compared with the ultrasound wavelength, the calibrated spectra of the RF data are often quasi-linear over the bandwidth used in typical ultrasound imaging. Therefore, a linear regression is sufficient to obtain a set of parameters from the calibrated tissue spectra. Typically, the slope and intercept of the regression line as well as the mid-band fit (MBF), which is the linear function evaluated at the midpoint of the usable bandwidth, are used in spectrum analysis. Importantly, it has been shown theoretically that these spectral regression parameters are related to tissue microstructural properties [37, 51, 59]. For example, spectral slope depends on

the scatterer size, whereas MBF relates to size, concentration and relative acoustic impedances of the scattering elements [51].

Spectrum analysis can be applied to data from conventional ultrasound imaging (5-15 MHz) in diagnostic radiology [60], as well as to high frequency ultrasound imaging (20-60 MHz). The advantage of high frequencies, with wavelengths on the order of 100 μm, is that the higher resolution allows characterization of smaller tissue structures. Spectral analysis has been implemented to characterize the properties of cell aggregates that were used as simplified models of tumors [42, 60] and it was possible to detect cellular changes after exposure to chemotherapy [61]. In particular, it was found that ultrasound backscatter intensity and spectral slope increased after treatment, due to the decrease in the effective scatterer size associated with changes in cell nuclei and cell structure.

We recently implemented a high frequency spectral ultrasound imaging (SUSI) technique for non-invasive, quantitative assessment of engineered tissues. SUSI was applied to a model construct that mimics developing mineralized tissue [62]. **Figure 1-2** shows a schematic of the SUSI setup used.

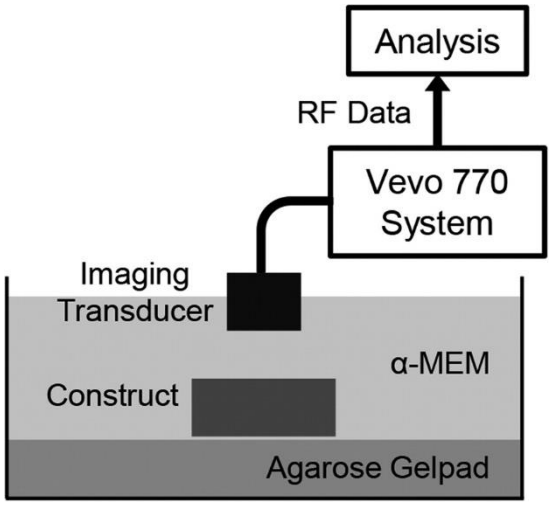

Figure 1-2. Schematic of experimental setup used for spectral ultrasound imaging (SUSI) of tissue construct. Adapted from Gudur *et al.* and used with permission [63].

The SUSI technique was validated using collagen hydrogels doped with known amounts of hydroxyapatite mineral (HA). Example grayscale and parametric images of HA-doped collagen gels are presented in **Figure 1-3**. It was shown that the MBF corresponded to HA concentration and therefore could be used to characterize the distribution of particles in the constructs. The spectral slope was inversely related to HA particle size, and therefore could be used to discriminate between different grades of HA.

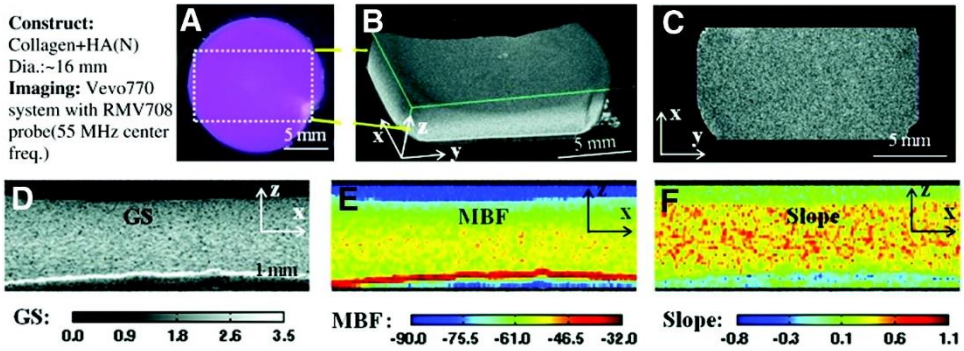

Figure 1-3. Virtual histology of three-dimensional (3D) collagen construct with added hydroxyapatite mineral. (A) Color image of the top view of constructs.(B) 3D ultrasound rendered image of the region outlined in (A). (C) Ultrasound C-scan of a transverse *x*–*y* plane. (D) Grayscale (GS), (E) midband fit (MBF), and (F) slope parametric images of one section in the *x*–*z*plane. Best viewed in *color*. Adapted from Gudur *et al.* and used with permission [63].

Exogenous mineralization of collagen gels was also induced via incubation in a high ionic strength solution to assess the ability of SUSI to monitor changes in the constructs over time, and to correlate spectral parameters with the concentration of mineral in the constructs. **Figure 1-4** shows example grayscale and parametric images at two time points. The MBF was useful in showing the pattern of mineral precipitation and the densification of the constructs over time. The slope parameter showed how particle size increased over time as mineral accretion progressed.

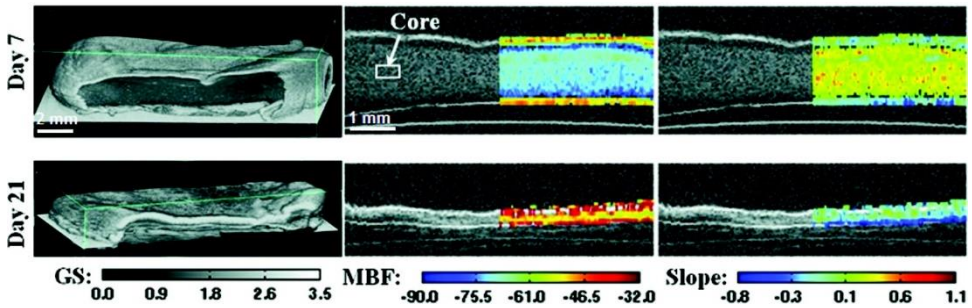

Figure 1-4. 3D rendered (*first column*), MBF superimposed on GS (*second column*), and slope superimposed on GS (*third column*) images of collagen constructs mineralized in simulated body fluid on day 7 and day 21. Best viewed in *color*. Adapted from Gudur *et al.* and used with permission [63].

In a follow-up study, we applied high resolution SUSI to quantitatively characterize the differentiation of pre-osteoblast cells seeded in 3D collagen-based engineered tissues [63]. SUSI was used to assess the compositional features of the cell-seeded constructs, including cell size, cell number, and calcium deposition. Estimation of cell size using the spectral slope parameter resulted in a value of 12-15 µm, which is larger than the nucleus alone and suggests that the cell body may also be involved in the scattering of ultrasound. Cell numbers were estimated based on the acoustic concentration (CQ^2) per unit volume, and agreed well with values obtained by conventional biochemical analysis at early time points. However, as the cells in the constructs differentiated, the cell number estimates became less accurate, presumably due to increased acoustic impedance caused by cellular calcium deposition. The value of the relative acoustic impedance was also used to estimate the mass of calcium deposited, which matched closely with data obtained by destructive biochemical analysis.

1.2.2 Mechanical Characterization

While grayscale B-mode ultrasound imaging is useful to understand tissue morphology and QUS imaging can assess certain aspects of tissue composition and microstructure, ultrasound imaging techniques also have potential for characterizing the mechanical properties of native and

engineered tissues [64, 65]. For example, ultrasound elastography techniques are based on the fact that ultrasound can detect signal changes that are specifically associated with the mechanical properties of tissue such as the stiffness or Young's modulus. Measurement of the speed of sound within a sample has also been used to characterize hydrogel mechanical properties [34]. Chung *et al*. [66] recently reported a study that estimated regional strains using ultrasound pulse-echo detection of a displacement generated by indentation of multilayered hydrogels and tissue engineered cartilage. Excellent reviews of ultrasound elasticity imaging methods have been provided by Greenleaf *et al*. [67], Parker *et al*. [68], Palmeri and Nightingale [69], and DeWall [67]. In the subsections below, we first summarize two main forms of ultrasound elastography: conventional ultrasound elasticity imaging (UEI) and acoustic radiation force (ARF) elasticity imaging. We then focus our attention to ultrasound techniques for assessing viscoelasticity for tissue engineering applications.

Ultrasound techniques for quantification of tissue stiffness

Ultrasound elasticity imaging (UEI) [70, 71], also called ultrasound elastography, has been exploited for tumor detection and other applications in which detection of spatial variation of tissue stiffness is informative [24, 70, 72]. These techniques are based on the differences of tissue displacements in uncompressed versus compressed tissues, as determined by ultrasound echo signals. Kim *et al*. has reported the use of ultrasound strain imaging technique for non-invasive monitoring of tissue scaffold degradation in tissue engineering [73].

In conventional UEI, an external static load is applied to the surface of a tissue to generate compression, usually via a mechanical device such as a platen. A sequence of pre- and post-compression ultrasound images are processed using a cross-correlation algorithm or speckle tracking scheme to detect the displacement at each location within the sample, to infer the elasticity

inside the sample [74, 75]. This technique has a particular advantage in imaging the spatial variation of mechanical properties within a tissue volume. For example, if a soft or hard inclusion is present in the tissue sample, the relative local deformation will exhibit a pattern that depends on the size of the inclusion and its stiffness relative to the surrounding material. UEI techniques exploit the same idea as manual palpation, but provide images of tissue volume with richer information in a more systematic and controlled fashion.

Acoustic radiation force (ARF) elasticity imaging uses the force associated with an ultrasound beam as a means to achieve deformation in a material body in a non-contact fashion [65]. Unlike the conventional form of UEI, ARF is a body force generated within a material sample generated by momentum transfer from the ultrasound wave to the medium [65]. For a plane wave, the ARF is proportional to the acoustic intensity, which is the time average of the acoustic pressure. If it is of sufficient magnitude, such a force may be utilized to induce tissue compression. In conventional ultrasound imaging, the ARF associated with the imaging pulse is small so that tissue deformation is negligible. However, an elegant form of ARF elasticity imaging, called acoustic radiation force impulse (ARFI) [76, 77] imaging adjusts the pulse intensity on selected pulses, and therefore can use the same pulse-echo ultrasound imaging system to generate both the compression ultrasound pulses, as well as the imaging pulses for detecting tissue displacements. **Figure 1-5** shows example grayscale and ARFI images for live tissue during a RF ablation procedure [78].

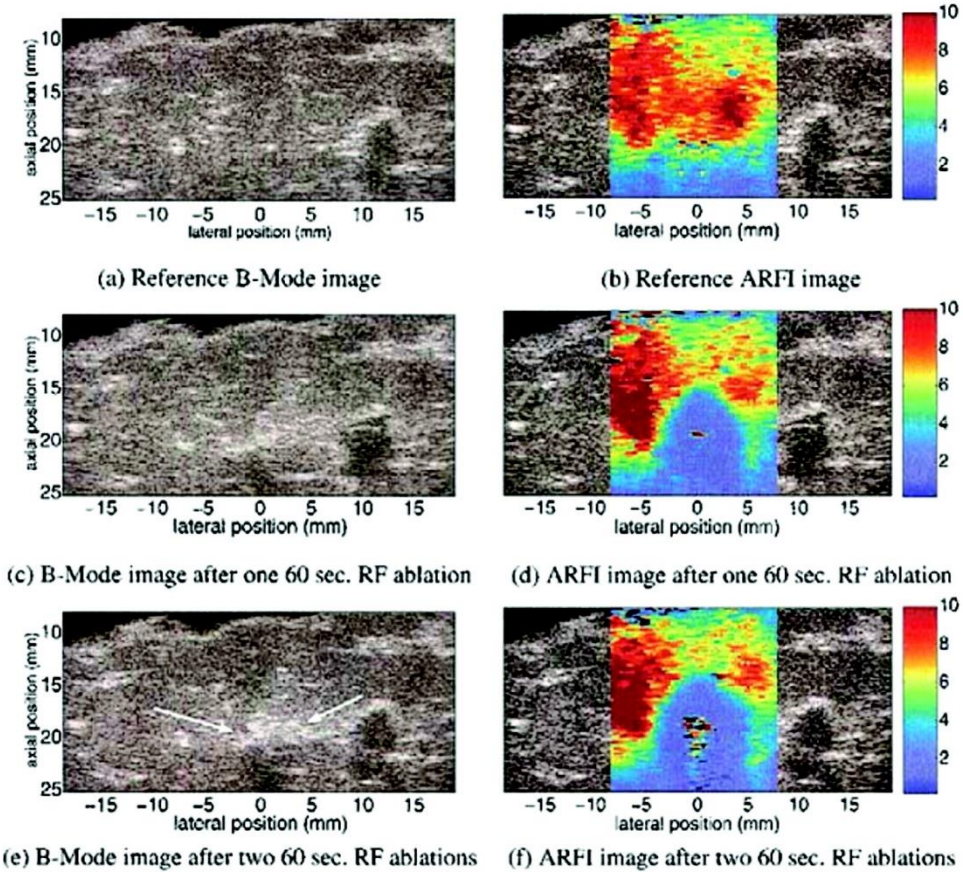

Figure 1-5. B-mode and acoustic radiation force impulse (ARFI) images of liver sample before (a and b) and after (c to f) radiofrequency (RF) ablation procedure. Best viewed in *color*. Adapted from Fahey *et al.* and used with permission [79].

Ultrasound techniques for quantification of the viscoelastic properties

In general, soft tissues are viscoelastic, inhomogeneous, and anisotropic [79], exhibiting properties of both elastic solids and viscous fluids. Engineered tissues typically make use of cells and biomaterial scaffolds that mimic key properties of the extracellular matrix (ECM), including biomechanical properties. Therefore, assessment of the material properties is an important tool in developing engineered tissues. However, current mechanical characterization methods are limited by the need for contact with the sample and their inherently destructive nature, which make them difficult to apply to cellular engineered constructs. Ultrasound techniques offer a new way of

characterizing engineered tissues, particularly those based on hydrogel scaffolds, which typically display viscoelastic properties.

Sonorheometry and monitoring of excitation and recovery using ARF imaging

Sonorheometry uses a series of high pulse repetition frequency (PRF) pulses to effectively generate a step excitation of a desired duration in sample [80]. This approach provides extended deformation and permits the measurement of the viscoelastic properties of a material. Walker *et al*. [81] used this technique, with 10 MHz transducer, to obtain the time-displacement curve from the sample. By fitting the time-displacement curve with a Voigt model, the relative elasticity and viscosity of the samples were derived. Since the ARF associated with typical imaging pulses are very small, Mauldin at el. extended the approach to allow monitoring of steady-state excitation and recovery (MSSER) of deformation in a sample before and after a step stress application [82]. Similar to ARFI elastography, the MSSER technique used two types of pulses using the same imaging system for both imaging and pushing, with 6.15 MHz and 4.21 MHz center frequency respectively. The pushing pulses were generated simply by increasing the acoustic pressure amplitude of the ultrasound pulses in order to deform the tissue more efficiently.

The sonorheometry and MSSER techniques employ the same ultrasound transducer and system for ARF application and imaging. While this configuration has advantages, it can also be restricting due to contradicting requirements for the compressing and imaging ultrasound beams. For example, high frequency is preferred to achieve high axial resolution for imaging. However, the correspondingly higher attenuation at high frequency results in reduced penetration depth. In addition, axial energy distribution at high frequency creates an inhomogeneous force field, complicating the analysis required to map the spatial distribution of viscoelastic properties. Also, these approaches require protocols to generate ARF pushing pulses with increased intensity, which

may present a technical barrier for working with commercial systems. Finally, while adjusting acoustic pressure amplitude and duration of the ultrasound pulses may be achieved with the same transducer, it may be difficult to alter the spatial beam characteristics using the same transducer.

Summary

Ultrasound techniques have proven their value in a wide range of *in vitro* and *in vivo* tissue characterization applications. These methods are particularly valuable in characterizing the spatial variation of tissue composition and properties, as well as in noninvasively monitoring tissue development over time. The use of non-ionizing radiation in ultrasound techniques to provide rapid, noninvasive, and image-based data therefore also has great potential in characterizing engineered tissues.

Ultrasound-based methods offer potentially important advantages over other tissue characterization techniques, and *in vitro* applications are progressively being translated to *in vivo* and clinical use. For example, UEI is now an FDA-approved technique for diagnostic breast imaging and classifying suspicious lesions [83]. Various forms of UEI techniques have also been exploited for other applications including characterizing contractility and strain in the myocardium [84-86]. Similarly, ARFI imaging has been investigated for multiple clinical applications, including assessment of changes in cardiac tissue stiffness [87] and detection of tumors in the prostate [88]. A version of ARFI elastography, called Virtual Touch tissue imaging, has been implemented on a commercial system with on-going clinical evaluations in Europe and Asia [65].

An important challenge in translating ARF-based ultrasound elastography techniques to *in vivo* applications is the difficulty in quantitatively characterizing the ARF. Relative measurements of tissue stiffness are useful in differentiating between healthy and diseased tissues. However, in some cases quantification of the material properties is preferred or necessary. *In vitro*

characterization of the ARF has been pursued, however strategies to determine its magnitude *in vivo* are also needed.

Ultrasound is unique in the way it interacts with biological tissue, offering the possibility of generating new kinds of mechanical properties data at scales relevant to cellular mechanobiology. The excellent tissue penetration and wide range of ultrasound frequencies and choice of other operating parameters make ultrasound techniques very versatile. Ultrasound is increasingly being applied to applications in tissue characterization, and offers a way to generate information-rich, quantitative representations of both native and engineered tissues.

1.3 Stimulation Techniques

Mechanical stimuli play a critical role in various stages of cell and tissue development and regeneration. Given the scope of this dissertation and the emphasis of ultrasound applications in musculoskeletal tissue engineering, in the following section we will focus on applications of extrinsic mechanical cues for directing stem cell fate and enhancing matrix deposition in mineralizing tissue.

1.3.1 Extrinsic Tensile, Compressive and Shear Stress

Tensile stress

Tensile stress is prominent in musculoskeletal system and tissues like muscle and tendons which naturally experience tensile forces when in motion. Abundant studies have convincingly demonstrated that effects of tensile forces in stem cell fate determination. Application of cyclic tensile strain can increase fibrogenic, osteogenic and chondrogenic markers in MSC, and effects are shown to heavily depend on the loading conditions [13, 19, 89-92]. Higher magnitude of strain guides MSCs towards myogenesis while low strain magnitude leads to osteogenesis [93]. Cyclic

tensile strain, when applied at appropriate magnitude and frequency, can increase osteogenic gene expression, alkaline phosphatase activity, calcium deposition rate and amount. Sun *et al.* [94] reported that the strain magnitude, loading frequency and direction of tensile forces influenced MSC proliferation and collagen production. Their study showed optimal results were obtained with 10% strain at 1.0 Hz when applying the load uniaxially, and at 0.1 Hz when applying load radially. Similar results have been reported by others using various scaffold materials including alginate, collagen-coated silicone, plastic strips and collagen [13, 19, 91, 95-97]. Increase in gene expression and alkaline phosphatase (ALP) were observed in some studies with treatment duration as short as 40 min [96]. Moreover, Sumanasinghe *et al.* [98] also reported cyclic tensile strain induces cytokines that inhibit bone resorption, suggesting potential benefits of marinating bone mass.

Compressive stress

Native bone tissues experience dynamic compressive loads with a peak magnitude around 0.2 – 0.35% [99] which occurs at a frequency around 1 – 3 Hz [100]. Only few studies have explored cyclic compressive strain at similar scale to the physiological dynamic load. One of the studies was shown by Ravichandran *et al.* where they cyclically compress cellular graft with 0.22% strain at 1 Hz for 4 h per day and observed an increase in osteogenic genes (osteonectin and COL1A1), ALP, and mineralization [100]. Most studies on cyclic compression investigated compressive strain in the range from 5% to 60% at 0.1 to 10 Hz [101-106]. Results from these studies demonstrated similar findings to those applying tensile stress. Osteogenesis favors low magnitude of strain while chondrogenesis favors higher strain magnitude, and adipogenesis is generally suppressed with cyclic strain [101-106]. Horner *et al.* [101] found that MSC differentiation into osteogenic/chondrogenic lineage is magnitude-dependent and inversely-

related. In this study, they compressed the electrospun scaffolds by 5 to 20% at 1 Hz for 2 h per day, and observed that with higher strain magnitude, the chondrogenic marker and glycosaminoglycan (GAG) production increases while osteogenic markers and mineralization decreases. These studies demonstrated that MSC lineage determination can be controlled by varying parameters in the dynamic strain regimen.

Shear stress

Shear stress is often related to fluid motion over the tissue surface and fluid-flow-induced shear stress has been found to be necessary for MSC to differentiate towards endothelial cells [107]. More recently, studies have shown that shear stress can also induce stem cell differentiation towards bone-producing cells [108] and osteoblastic lineage differentiation [109]. Kreke *et al.* [110] reported that continuous and intermittent shear stress can both enhance mineralization to similar levels at day 21, but shorter duration of continuous shear stress was needed to trigger up-regulation of osteogenesis-related prostaglandins. Additionally, according to a study conducted by Zhao *et al.* [111], flow rate also elicits different responses from hMSCs in the long term. When exposed to higher magnitude of shear stress, hMSCs in 3D scaffolds showed higher ALP activity and calcium deposition.

1.3.2 Low-Intensity Pulsed Ultrasound (LIPUS)

Low-Intensity Pulsed Ultrasound (LIPUS) has been shown clinically to accelerate fresh fracture healing [112, 113], effectively treat delayed unions [114] and nonunion [115, 116]. A commercial device has been approved by Food and Drug Administration (FDA) for fracture healing. In contrast to high-intensity (1 – 300 mW/cm^2) continuous ultrasound that are used to cause heat in tissues, LIPUS deliverers pulsed acoustic energy of low intensity (5 – 100 mW/cm^2) that are considered to be nondestructive and with limited thermal effects [117]. The LIPUS

treatment typically applies ultrasound waves of 1.5 MHz repeating at 1 kHz with 20% duty cycle at an intensity of 30 mW/cm^2 spatial average temporal average (SATA) for 20 min per day [118]. In the last two decades, it has also drawn attention for in vitro applications on stem cells, pre-osteoblastic cells and bone cell [26-28]. It has been shown to promote osteogenesis and chondrogenesis while suppressing adipogenesis [119-124], and the lineage determination mostly depends on the treatment intensity and pulse repetition frequency (PRF) [125-127]. Effectiveness of using LIPUS for differentiating stem cells towards a specific lineage also depends on the daily treat dosage and the onset timing [128, 129]. Further enhancement in acceleration fracture healing and promoting osteogenesis has been achieved when combining LIPUS with other mechanical stimuli such as microgravity, vibration or cyclic strain [121, 130, 131].

As acoustic wave delivered with LIPUS reaches the cells, it can act on integrin, mechanosensitive ion channels and gap junctions, and promote focal adhesion formation and increase matrix deposition [132-136]. LIPUS has been found to trigger various biochemical events in the cellular level [137-140] and several signaling pathways including integrin/phosphatidylinositol 3-OH kinase (PI3K)/Akt and ROCK-Cot/Tpl2-MEK-extracellular regulated kinase (ERK) pathway are involved in the mechanotransduction associated with LIPUS [136, 141-144]. The effects caused by LIPUS is believed to be associated with acoustic microstreaming and small oscillations of particles [138]. Microstreaming, distinctive from bulk streaming, requires secondary cavitation and therefore only exists *in vitro* in the form of eddies flow [145]. When occurs at cell-matrix interface, microstreaming is strong enough to change cell permeability and trigger cellular events [145]. Despite the existence of several theoretical explanations, the underlying mechanism of LIPUS has not been solidly elucidated.

1.4 Project Goal and Hypothesis

The overall goal of this project is to develop a noninvasive mechanical testing system that can quantitatively characterize the viscoelastic mechanical properties of engineered tissues and a noninvasive stimulation method to cyclically strain cellular constructs to promote osteogenesis and enhance mineralization in engineered tissues. Together with the previously developed SUSI technique, we have a long-term goal to use these noninvasive techniques to comprehensibly study the mechanobiology and gain more control in developing tissue engineering approaches. Here, we propose a multimode ultrasound viscoelastography technique that aims to enable longitudinal monitoring and localized characterization of viscoelastic properties, which is crucial for quality control of engineered tissue constructs and comprehensive understanding of tissue development. In addition, we also intend to induce cyclic strain using ARF to promote stem cell differentiation and enhance mineralization. **We hypothesize that the acoustic radiation force can be applied 1) in a controlled and continuous manner to deform soft materials with concurrent ultrasound imaging for characterizing both bulk and local microscale viscoelastic properties quantitatively; 2) in a pulsed fashion to induce localized cyclic strain in engineered constructs seeded with human mesenchymal stem cells (hMSCs) to promote osteogenic differentiation and enhance mineralization.**

1.5 Specific Aims

Specific Aim 1: Implement a noninvasive multi-mode ultrasound visco-elastography (MUVE) system for characterizing viscoelastic property of 3D engineered constructs.

The MUVE system will be implemented to conduct mechanical test on 3D engineered tissue constructs utilizing acoustic radiation force. The proposed system consists of a focused ultrasound (FUS) transducer and a higher frequency imaging transducer. Mechanical compression

on the tissue constructs will be applied utilizing ARF from the FUS transducer, and deformation will be monitored using the imaging transducer. With the high resolution provided by ultrasound imaging, the cellular scale strain distribution within the construct will be mapped, and both bulk and local viscoelastic properties will be measured. To quantitatively characterize the viscoelastic properties of engineered constructs, parameters will be extracted by fitting resulted strain-time curves from the MUVE system to established mechanical models. Moreover, results obtained from MUVE will be compared to rheology and nanoindentation measurements for validation.

Specific Aim 2: Interrogate viscoelastic properties in heterogeneous engineered constructs using MUVE

This aim will further explore the capability of the MUVE system for measuring localized mechanical properties in 3D. We will test whether the system can detect difference in viscoelastic properties in multiphase constructs. Hydrogels with inclusions of varying sizes will be used to examine the resolution of the system. In addition, we will vary the concentration difference between the hydrogel and the inclusion to determine the detectivity, which defines the system's detectable contrast in hydrogel composition.

Specific Aim 3: Develop an ARF-based tissue stimulation technique that utilizes pulsed focused ultrasound to enhance osteogenic differentiation in engineered tissue constructs.

In this specific aim, higher intensity focused ultrasound will be applied in a pulsed manner to induce cyclic strain in tissue constructs. We will investigate the influence of pulse repetition rate (PRF), ultrasound intensity, and treatment duration on osteogenesis and mineralization in collagen-fibrin hydrogels seeded with hMSCs and determine the parameters for optimal outcomes. Effects of the treatment will be evaluated based on cell viability, osteogenesis-related protein expression and mineral deposition.

These aims will guide us to develop an ultrasound mechanical testing technique that can nondestructively and noninvasively characterize bulk and localized mechanical properties of engineered tissue constructs. Additionally, a new ultrasound treatment strategy for enhancing osteogenic differentiation in engineered constructs will be investigated. The achievement of the goals will provide a new tool for nondestructive mechanical characterization and more efficient stimulation therapy for engineered tissue constructs, which further expands the scope of ultrasound applications in the field of tissue engineering.

1.6 Preview of Thesis

The present chapter (Chapter 1) provides the background and motivation of the dissertation, reviews the current methods and techniques for characterization and stimulation of tissue engineered constructs, and presents the hypothesis and specific aims of this dissertation. Part of Chapter 1 was published in *Tissue Engineering Part B: Reviews* in 2016 [146].

An application of the spectral ultrasound imaging (SUSI) technique in an animal model for detection of heterotopic ossification is discussed in Chapter 2. Parameters from SUSI differentiated mineralizing tissue from its surrounding tissue in a burn/tenotomy animal model and also from the uninjured control animal model. SUSI detected early ossification just one week after injury, which is 3 to 4 weeks earlier than when imaging with μCT. The study also demonstrates the feasibility of applying the ultrasound technique *in vivo*. This chapter has been accepted for publication in *Bone* this year.

Chapter 3 (aim 1) presents our work in developing the multimodel ultrasound viscoelastography system, which addresses aim 1. The system uses a FUS transducer to apply constant ARF to deform the sample while monitoring the deformation with a higher frequency imaging transducer. Both qualitative and quantitative results were obtained to characterize the bulk

and local viscoelastic properties of agarose, collagen and fibrin hydrogels doped with hydroxyapatite as well as cell-seeded collagen constructs. This chapter was published in *Biomaterials* in 2016 [147].

The MUVE system was then used to interrogate the mechanical properties in heterogeneous materials and the study is presented in Chapter 4 (aim 2). The MUVE system detected distinctive viscoelastic properties in multiphase constructs with agarose microbeads embedded in agarose, collagen and fibrin hydrogels. We varied the size of the agarose microbead and determined the system axial resolution to be around 200 μm and the system can detect a concentration difference of 9.54 mg/ml in agarose. Results from the MUVE system was compared with that from nanoindentation and shear rheometry, which addresses part of aim 1. This chapter is currently under submission process.

We then adapted the MUVE system to implement a stimulation system which applies pulsed focused ARF to induce localized cyclic strain in collagen/fibrin hydrogels seeded with hMSCs. The system implementation, optimization and effects are discussed in Chapter 5. We explored the effects of pulse PRF and intensity on the induced strain profile and their influences on osteogenesis together with treatment duration. The ARF intensity was also increased to address the stiffening in the mineralizing constructs over time to further improve the system perform.

Chapter 6 summarizes all the findings of this dissertation work and discusses several future directions to advance the current techniques and expand the applications.

1.7 References

1. Muschler, G.E., C. Nakamoto, and L.G. Griffith, *Engineering principles of clinical cell-based tissue engineering.* Journal of Bone and Joint Surgery-American Volume, 2004. **86A**(7): p. 1541-1558.
2. Spector, M., *Biomaterials-based tissue engineering and regenerative medicine solutions to musculoskeletal problems.* Swiss Medical Weekly, 2006. **136**(19-20): p. 293-301.

3. Jen, A.C., M.C. Wake, and A.G. Mikos, *Review: Hydrogels for cell immobilization.* Biotechnology and Bioengineering, 1996. **50**(4): p. 357-364.

4. Loo, Y. and C.A.E. Hauser, *Bioprinting synthetic self-assembling peptide hydrogels for biomedical applications.* Biomedical Materials, 2016. **11**(1).

5. Meghezi, S., B. Drouin, and D. Mantovani, *Collagen hydrogel-based scaffolds for vascular tissue regeneration: Mechanical and viscoelastic characterization*, in *Characterization of Polymeric Biomaterials*, M.C. Tanzi and S. Fare, Editors. 2017. p. 397-439.

6. Silva, R., B. Fabry, and A.R. Boccaccini, *Fibrous protein-based hydrogels for cell encapsulation.* Biomaterials, 2014. **35**(25): p. 6727-6738.

7. Guilak, F., *Functional tissue engineering - The role of biomechanics in reparative medicine*, in *Reparative Medicine: Growing Tissues and Organs*, J.D. Sipe, C.A. Kelley, and L.A. McNicol, Editors. 2002. p. 193-195.

8. Guilak, F., *et al.*, *Biomechanics and mechanobiology in functional tissue engineering.* Journal of Biomechanics, 2014. **47**(9): p. 1933-1940.

9. Gudur, M.S.R., *et al.*, *Noninvasive Quantification of In Vitro Osteoblastic Differentiation in 3D Engineered Tissue Constructs Using Spectral Ultrasound Imaging.* Plos One, 2014. **9**(1).

10. Chaudhuri, O., *et al.*, *Substrate stress relaxation regulates cell spreading.* Nature Communications, 2015. **6**.

11. Chaudhuri, O., *et al.*, *Hydrogels with tunable stress relaxation regulate stem cell fate and activity.* Nature Materials, 2016. **15**(3): p. 326-344.

12. Haasper, C., *et al.*, *Osteogenic Differentiation of Human Bone Marrow Stromal Cells (hBMSC) by Cyclic Longitudinal Mechanical Strain and Dexamethasone.* Zeitschrift Fur Orthopadie Und Unfallchirurgie, 2008. **146**(5): p. 636-643.

13. Hamilton, D.W., T.M. Maul, and D.A. Vorp, *Characterization of the response of bone marrow derived progenitor cells to cyclic strain: Implications for vascular tissue engineering applications (vol 10, pg 361, 2004).* Tissue Engineering Part A, 2008. **14**(3): p. 461-461.

14. Kearney, E.M., *et al.*, *Tensile Strain as a Regulator of Mesenchymal Stem Cell Osteogenesis.* Annals of Biomedical Engineering, 2010. **38**(5): p. 1767-1779.

15. Lee, I.C., *et al.*, *The differentiation of mesenchymal stem cells by mechanical stress or/and co-culture system.* Biochemical and Biophysical Research Communications, 2007. **352**(1): p. 147-152.

16. Maredziak, M., *et al.*, *The Effect of Low-Magnitude Low-Frequency Vibrations (LMLF) on Osteogenic Differentiation Potential of Human Adipose Derived Mesenchymal Stem Cells.* Cellular and Molecular Bioengineering, 2017. **10**(6): p. 549-562.

17. Pelaez, D., C.Y.C. Huang, and H.S. Cheung, *Cyclic Compression Maintains Viability and Induces Chondrogenesis of Human Mesenchymal Stem Cells in Fibrin Gel Scaffolds.* Stem Cells and Development, 2009. **18**(1): p. 93-102.

18. Li, Y.J., *et al*., *Oscillatory fluid flow affects human marrow stromal cell proliferation and differentiation.* Journal of Orthopaedic Research, 2004. **22**(6): p. 1283-1289.

19. Qi, M.C., *et al*., *Expression of Bone-related Genes in Bone Marrow MSCs after Cyclic Mechanical Strain: Implications for Distraction Osteogenesis.* International Journal of Oral Science, 2009. **1**(3): p. 143-150.

20. Sumanasinghe, R.D., S.H. Bernacki, and E.G. Loboa, *Osteogenic differentiation of human mesenchymal stem cells in collagen matrices: Effect of uniaxial cyclic tensile strain on bone morphogenetic protein (BMP-2) mRNA expression.* Tissue Engineering, 2006. **12**(12): p. 3459-3465.

21. Plotkin, L.I., *et al*., *Mechanical stimulation prevents osteocyte apoptosis: requirement of integrins, Src kinases, and ERKs.* American Journal of Physiology-Cell Physiology, 2005. **289**(3): p. C633-C643.

22. Lu, J.Y., H.H. Zou, and J.F. Greenleaf, *BIOMEDICAL ULTRASOUND BEAM FORMING.* Ultrasound in Medicine and Biology, 1994. **20**(5): p. 403-428.

23. Sarvazyan, A.P., O.V. Rudenko, and W.L. Nyborg, *BIOMEDICAL APPLICATIONS OF RADIATION FORCE OF ULTRASOUND: HISTORICAL ROOTS AND PHYSICAL BASIS.* Ultrasound in Medicine and Biology, 2010. **36**(9): p. 1379-1394.

24. Ophir, J., *et al*., *ELASTOGRAPHY - A QUANTITATIVE METHOD FOR IMAGING THE ELASTICITY OF BIOLOGICAL TISSUES.* Ultrasonic Imaging, 1991. **13**(2): p. 111-134.

25. Garra, B.S., *et al*., *Elastography of breast lesions: Initial clinical results.* Radiology, 1997. **202**(1): p. 79-86.

26. Hoeks, A.P.G., *et al*., *Non-invasive measurement of mechanical properties of arteries in health and disease.* Proceedings of the Institution of Mechanical Engineers Part H-Journal of Engineering in Medicine, 1999. **213**(H3): p. 195-202.

27. Levinson, S.F., M. Shinagawa, and T. Sato, *SONOELASTIC DETERMINATION OF HUMAN SKELETAL-MUSCLE ELASTICITY.* Journal of Biomechanics, 1995. **28**(10): p. 1145-1154.

28. Claes, L. and B. Willie, *The enhancement of bone regeneration by ultrasound.* Progress in Biophysics & Molecular Biology, 2007. **93**(1-3): p. 384-398.

29. Gebauer, D., *et al*., *Low-intensity pulsed ultrasound: Effects on nonunions.* Ultrasound in Medicine and Biology, 2005. **31**(10): p. 1391-1402.

30. Dyson, M. and J. Suckling, *Stimulation of tissue repair by ultrasound: a survey of the mechanisms involved.* Physiotherapy, 1978. **64**(4): p. 105-8.

31. Fite, B.Z., *et al*., *Noninvasive multimodal evaluation of bioengineered cartilage constructs combining time-resolved fluorescence and ultrasound imaging.* Tissue Eng. Part C-Methods, 2011. **17**(4): p. 495-504.

32. Kreitz, S., *et al*., *Nondestructive method to evaluate the collagen content of fibrin-based tissue engineered structures via ultrasound.* Tissue Eng. Part C-Methods, 2011. **17**(10): p. 1021-1026.

33. Oe, K., *et al*., *Nondestructive evaluation of cell numbers in bone marrow stromal cell/beta-tricalcium phosphate composites using ultrasound.* Tissue Eng. Part C-Methods, 2010. **16**(3): p. 347-353.

34. Rice, M.A., K.R. Waters, and K.S. Anseth, *Ultrasound monitoring of cartilaginous matrix evolution in degradable PEG hydrogels.* Acta. Biomater., 2009. **5**(1): p. 152-161.

35. Walker, J.M., *et al*., *Nondestructive evaluation of hydrogel mechanical properties using ultrasound.* Ann. Biomed. Eng., 2011. **39**(10): p. 2521-30.

36. Insana, M.F. and D.G. Brown, *Acoustic scattering theory applied to soft biological tissues*, in *Ultrasonic Scattering in Biological Tissues*, K.K. Shung, Editor. 1993, CRC Press: Boca Raton. p. 75-124.

37. Lizzi, F.L., *et al*., *Theoretical framework for spectrum analysis in ultrasonic tissue characterization.* J. Acoust. Soc. Am., 1983. **73**(4): p. 1366-73.

38. Lizzi, F.L., *et al*., *Ultrasonic spectrum analysis for tissue assays and therapy evaluation.* Int. J. Imag. Syst. Tech., 1997. **8**(1): p. 3-10.

39. Feleppa, E.J., *et al*., *Spectrum-analysis and neural networks for imaging to detect and treat prostate cancer.* Ultrason. Imaging, 2001. **23**(3): p. 135-46.

40. Golub, R.M., *et al*., *Differentiation of breast-tumors by ultrasonic tissue characterization.* J. Ultras. Med., 1993. **12**(10): p. 601-608.

41. Feleppa, E.J., *Ultrasonic tissue-type imaging of the prostate: Implications for biopsy and treatment guidance.* Cancer Biomarkers, 2008. **4**(4-5): p. 201-212.

42. Nasu, K., *et al*., *Accuracy of in vivo coronary plaque morphology assessment - A validation study of in vivo virtual histology compared with in vitro histopathology.* J. Am. Coll. Cardiol., 2006. **47**(12): p. 2405-2412.

43. Kolios, M.C., *et al*., *Ultrasonic spectral parameter characterization of apoptosis.* Ultrasound Med. Biol., 2002. **28**(5): p. 589-97.

44. Brand, S., *et al*., *High frequency ultrasound tissue characterization and acoustic microscopy of intracellular changes.* Ultrasound Med. Biol., 2008. **34**(9): p. 1396-407.

45. Ghoshal, G., *et al*., *Quantitative ultrasound imaging for monitoring in situ high-intensity focused ultrasound exposure.* Ultrason. Imaging, 2014. **36**(4): p. 239-55.

46. Vlad, R.M., *et al*., *Quantitative ultrasound characterization of responses to radiotherapy in cancer mouse models.* Clin. Cancer Res., 2009. **15**(6): p. 2067-75.

47. Kemmerer, J.P. and M.L. Oelze, *Ultrasonic assessment of thermal therapy in rat liver.* Ultrasound Med. Biol., 2012. **38**(12): p. 2130-7.

48. Thomas, L.J., *et al*., *Quantitative real-time imaging of myocardium based on ultrasonic integrated backscatter.* IEEE Trans Ultrason Ferroelectr Freq Control, 1989. **36**(4): p. 466-70.

49. Insana, M.F. and T.J. Hall, *Parametric ultrasound imaging from backscatter coefficient measurements: image formation and interpretation.* Ultrason. Imaging, 1990. **12**(4): p. 245-67.

50. Mercado, K.P., *et al*., *Estimating cell concentration in three-dimensional engineered tissues using high frequency quantitative ultrasound.* Ann. Biomed. Eng., 2014. **42**(6): p. 1292-304.

51. Mercado, K.P., *et al*., *Noninvasive quantitative imaging of collagen mcrostructure in three-dmensional hydrogels using high-frequency ultrasound.* Tissue Eng. Part C-Methods, 2015.

52. Lizzi, F.L., *et al*., *Relationship of ultrasonic spectral parameters to features of tissue microstructure.* IEEE Trans. Ultrason. Ferroelectr. Freq. Control, 1987. **34**(3): p. 319-29.

53. Lizzi, F.L., *et al*., *Ultrasonic spectrum analysis for tissue evaluation.* Pattern Recog. Lett., 2003. **24**: p. 637-658.

54. Nair, A., *et al*., *Coronary plaque classification with intravascular ultrasound radiofrequency data analysis.* Circulation, 2002. **106**(17): p. 2200-2206.

55. Qian, J., *et al*., *Impact of gender and age on in vivo virtual histology-intravascular ultrasound imaging plaque characterization (from the global virtual vistology intravascular ultrasound [VH-IVUS] registry).* Am. J. Cardiol., 2009. **103**(9): p. 1210-1214.

56. Gudur, M.S., *et al*., *High-frequency rapid B-mode ultrasound imaging for real-time monitoring of lesion formation and gas body activity during high-intensity focused ultrasound ablation.* IEEE Trans. Ultrason. Ferroelectr. Freq. Control, 2012. **59**(8): p. 1687-99.

57. Kumon, R.E., *et al*., *High-frequency ultrasound M-mode imaging for identifying lesion and bubble activity during high-intensity focused ultrasound ablation.* Ultrasound Med. Biol., 2012. **38**(4): p. 626-641.

58. Kumon, R.E., *et al*., *In vivo characterization of pancreatic and lymph node tissue by using EUS spectrum analysis: a validation study.* Gastrointest Endosc., 2010. **71**(1): p. 53-63.

59. Kumon, R.E., *et al*., *EUS spectrum analysis for in vivo characterization of pancreatic and lymph node tissue: a pilot study.* Gastrointest Endosc., 2007. **66**(6): p. 1096-106.

60. Lizzi, F.L., *et al*., *Statistical framework for ultrasonic spectral parameter imaging.* Ultrasound Med. Biol., 1997. **23**(9): p. 1371-82.

61. Vlad, R.M., *et al*., *Quantitative ultrasound characterization of cancer radiotherapy effects in vitro.* Int. J. Radiat. Oncol., 2008. **72**(4): p. 1236-1243.

62. Czarnota, G.J., *et al*., *Ultrasound imaging of apoptosis: high-resolution non-invasive monitoring of programmed cell death in vitro, in situ and in vivo.* Brit. J. Cancer, 1999. **81**(3): p. 520-527.

63. Gudur, M., *et al*., *Noninvasive, quantitative, spatiotemporal characterization of mineralization in three-dimensional collagen hydrogels using high-resolution spectral ultrasound imaging.* Tissue Eng. Part C-Methods, 2012. **18**(12): p. 935-946.

64. Gudur, M.S., *et al*., *Noninvasive quantification of in vitro osteoblastic differentiation in 3D engineered tissue constructs using spectral ultrasound imaging.* PLoS One, 2014. **9**(1): p. e85749.

65. Sarvazyan, A., *et al*., *An overview of elastography - an emerging branch of medical imaging.* Curr. Med. Imaging Rev., 2011. **7**(4): p. 255-282.

66. Doherty, J.R., *et al*., *Acoustic radiation force elasticity imaging in diagnostic ultrasound.* IEEE Trans. Ultrason. Ferroelectr. Freq. Control, 2013. **60**(4): p. 685-701.

67. Chung, C.Y., *et al*., *Ultrasound elastography for estimation of regional strain of multilayered hydrogels and tissue-engineered cartilage.* Ann. Biomed. Eng., 2015.

68. Greenleaf, J.F., M. Fatemi, and M. Insana, *Selected methods for imaging elastic properties of biological tissues.* Annu. Rev. Biomed. Eng., 2003. **5**: p. 57-78.

69. Parker, K.J., *et al*., *A unified view of imaging the elastic properties of tissue.* J. Acoust. Soc. Am., 2005. **117**(5): p. 2705-12.

70. Palmeri, M.L. and K.R. Nightingale, *Acoustic radiation force-based elasticity imaging methods.* Interface Focus., 2011. **1**(4): p. 553-64.

71. Ophir, J., *et al*., *Elastography: a quantitative method for imaging the elasticity of biological tissues.* Ultrason. Imaging, 1991. **13**(2): p. 111-34.

72. Dewall, R.J., *Ultrasound elastography: principles, techniques, and clinical applications.* Crit. Rev. Biomed. Eng., 2013. **41**(1): p. 1-19.

73. Hoeks, A.P.G., *et al*., *Non-invasive measurement of mechanical properties of arteries in health and disease.* P. I. Mech. Eng. H., 1999. **213**(H3): p. 195-202.

74. Kim, K., C.G. Jeong, and S.J. Hollister, *Non-invasive monitoring of tissue scaffold degradation using ultrasound elasticity imaging.* Acta. Biomater., 2008. **4**(4): p. 783-90.

75. Lubinski, M.A., S.Y. Emelianov, and M. O'Donnell, *Speckle tracking methods for ultrasonic elasticity imaging using short-time correlation.* IEEE Trans. Ultrason. Ferroelectr. Freq. Control, 1999. **46**(1): p. 82-96.

76. Bilgen, M. and M.F. Insana, *Deformation models and correlation analysis in elastography.* J. Acoust. Soc. Am., 1996. **99**(5): p. 3212-24.

77. Nightingale, K., *et al*., *Acoustic radiation force impulse imaging: In vivo demonstration of clinical feasibility.* Ultrasound Med. Biol., 2002. **28**(2): p. 227-235.

78. Nightingale, K.R., *et al*., *On the feasibility of remote palpation using acoustic radiation force.* J. Acoust. Soc. Am., 2001. **110**(1): p. 625-34.

79. Fahey, B.J., *et al*., *Acoustic radiation force impulse imaging of thermally- and chemically-induced lesions in soft tissues: preliminary ex vivo results.* Ultrasound Med. Biol., 2004. **30**(3): p. 321-8.

80. Pinto, J.G., *et al*., *A device for testing mechanical properties of biological materials--the "Biodyne".* J. Appl. Physiol., 1975. **39**(5): p. 863-7.

81. Viola, F., *et al*., *Sonorheometry: a noncontact method for the dynamic assessment of thrombosis.* Ann. Biomed. Eng., 2004. **32**(5): p. 696-705.

82. Walker, W.F., F.J. Fernandez, and L.A. Negron, *A method of imaging viscoelastic parameters with acoustic radiation force.* Phys. Med. Biol., 2000. **45**(6): p. 1437-47.

83. Mauldin, F.W., Jr., *et al*., *Monitored steady-state excitation and recovery (MSSER) radiation force imaging using viscoelastic models.* IEEE Trans. Ultrason. Ferroelectr. Freq. Control, 2008. **55**(7): p. 1597-610.

84. Roach, M., 3rd, *et al*., *Diagnostic and therapeutic imaging for cancer: therapeutic considerations and future directions.* J. Surg. Oncol., 2011. **103**(6): p. 587-601.

85. Urheim, S., *et al*., *Myocardial strain by doppler echocardiography: validation of a new method to quantify regional myocardial function.* Circulation, 2000. **102**(10): p. 1158-64.

86. D'Hooge, J., *et al*., *Two-dimensional ultrasonic strain rate measurement of the human heart in vivo.* IEEE Trans. Ultrason. Ferroelectr. Freq. Control, 2002. **49**(2): p. 281-6.

87. Jia, C., *et al*., *Two-dimensional strain imaging of controlled rabbit hearts.* Ultrasound Med. Biol., 2009. **35**(9): p. 1488-501.

88. Hsu, S.J., *et al*., *In vivo assessment of myocardial stiffness with acoustic radiation force impulse imaging.* Ultrasound Med. Biol., 2007. **33**(11): p. 1706-19.

89. Zhai, L., *et al*., *Acoustic radiation force impulse imaging of human prostates: initial in vivo demonstration.* Ultrasound Med. Biol., 2012. **38**(1): p. 50-61.

90. Altman, G.H., *et al*., *Advanced bioreactor with controlled application of multi-dimensional strain for tissue engineering.* Journal of Biomechanical Engineering-Transactions of the Asme, 2002. **124**(6): p. 742-749.

91. Baker, B.M., *et al*., *Dynamic Tensile Loading Improves the Functional Properties of Mesenchymal Stem Cell-Laden Nanofiber-Based Fibrocartilage.* Tissue Engineering Part A, 2011. **17**(9-10): p. 1445-1455.

92. Hanson, A.D., *et al*., *Osteogenic Effects of Rest Inserted and Continuous Cyclic Tensile Strain on hASC Lines with Disparate Osteodifferentiation Capabilities.* Annals of Biomedical Engineering, 2009. **37**(5): p. 955-965.

93. McMahon, L.A., *et al*., *Regulatory effects of mechanical strain on the chondrogenic differentiation of MSCs in a collagen-GAG scaffold: Experimental and computational analysis.* Annals of Biomedical Engineering, 2008. **36**(2): p. 185-194.

94. Jang, J.-Y., *et al*., *Combined Effects of Surface Morphology and Mechanical Straining Magnitudes on the Differentiation of Mesenchymal Stem Cells without Using Biochemical Reagents.* Journal of Biomedicine and Biotechnology, 2011.

95. Sun, L., *et al*., *Effects of Mechanical Stretch on Cell Proliferation and Matrix Formation of Mesenchymal Stem Cell and Anterior Cruciate Ligament Fibroblast.* Stem Cells International, 2016.

96. Haudenschild, A.K., *et al*., *Pressure and Distortion Regulate Human Mesenchymal Stem Cell Gene Expression.* Annals of Biomedical Engineering, 2009. **37**(3): p. 492-502.

97. Qi, M.C., *et al*., *Mechanical strain induces osteogenic differentiation: Cbfa1 and Ets-1 expression in stretched rat mesenchymal stem cells.* International Journal of Oral and Maxillofacial Surgery, 2008. **37**(5): p. 453-458.

98. Ward, D.F., Jr., *et al*., *Mechanical strain enhances extracellular matrix-induced gene focusing and promotes osteogenic differentiation of human mesenchymal stem cells through an extracellular-related kinase-dependent pathway.* Stem Cells and Development, 2007. **16**(3): p. 467-479.

99. Sumanasinghe, R.D., *et al*., *Expression of Proinflammatory Cytokines by Human Mesenchymal Stem Cells in Response to Cyclic Tensile Strain.* Journal of Cellular Physiology, 2009. **219**(1): p. 77-83.

100. Rubin, C.T. and L.E. Lanyon, *OSTEOREGULATORY NATURE OF MECHANICAL STIMULI - FUNCTION AS A DETERMINANT FOR ADAPTIVE REMODELING IN BONE.* Journal of Orthopaedic Research, 1987. **5**(2): p. 300-310.

101. Ravichandran, A., *et al*., *In vitro cyclic compressive loads potentiate early osteogenic events in engineered bone tissue.* Journal of Biomedical Materials Research Part B-Applied Biomaterials, 2017. **105**(8): p. 2366-2375.

102. Horner, C.B., *et al*., *Magnitude-dependent and inversely-related osteogenic/chondrogenic differentiation of human mesenchymal stem cells under dynamic compressive strain.* Journal of tissue engineering and regenerative medicine, 2016.

103. Huang, A.H., *et al*., *Long-term dynamic loading improves the mechanical properties of chondrogenic mesenchymal stem cell-laden hydrogel.* European cells & materials, 2010. **19**: p. 72-85.

104. Li, R., *et al*., *Mechanical Strain Regulates Osteogenic and Adipogenic Differentiation of Bone Marrow Mesenchymal Stem Cells.* Biomed Research International, 2015.

105. Nam, J., *et al*., *Novel Electrospun Scaffolds for the Molecular Analysis of Chondrocytes Under Dynamic Compression.* Tissue Engineering Part A, 2009. **15**(3): p. 513-523.

106. Rath, B., *et al*., *Compressive forces induce osteogenic gene expression in calvarial osteoblasts.* Journal of Biomechanics, 2008. **41**(5): p. 1095-1103.

107. Yamada, M., *et al*., *Effect of mechanical stress on differentiation of mouse mesenchymal stem cells seeded into an octacalcium phosphate-gelatin scaffold.* Sensors and Actuators B-Chemical, 2015. **220**: p. 125-130.

108. Shah, N., Y. Morsi, and R. Manasseh, *From mechanical stimulation to biological pathways in the regulation of stem cell fate.* Cell Biochemistry and Function, 2014. **32**(4): p. 309-325.

109. Stolberg, S. and K.E. McCloskey, *Can Shear Stress Direct Stem Cell Fate?* Biotechnology Progress, 2009. **25**(1): p. 10-19.

110. Knippenberg, M., *et al*., *Adipose tissue-derived mesenchymal stem cells acquire bone cell-like responsiveness to fluid shear stress on osteogenic stimulation.* Tissue Engineering, 2005. **11**(11-12): p. 1780-1788.

111. Kreke, M.R., *et al*., *Effect of intermittent shear stress on mechanotransductive signaling and osteoblastic differentiation of bone marrow stromal cells.* Tissue Engineering Part A, 2008. **14**(4): p. 529-537.

112. Zhao, F., R. Chella, and T. Ma, *Effects of shear stress on 3-D human mesenchymal stem cell construct development in a perfusion bioreactor system: Experiments and hydrodynamic modeling.* Biotechnology and Bioengineering, 2007. **96**(3): p. 584-595.

113. Brookes, M. and M. Dyson, *STIMULATION OF BONE REPAIR BY ULTRASOUND.* Journal of Bone and Joint Surgery-British Volume, 1983. **65**(5): p. 659-659.

114. Jung, Y.J., *et al*., *FOCUSED LOW-INTENSITY PULSED ULTRASOUND ENHANCES BONE REGENERATION IN RAT CALVARIAL BONE DEFECT THROUGH ENHANCEMENT OF CELL PROLIFERATION.* Ultrasound in Medicine and Biology, 2015. **41**(4): p. 999-1007.

115. Romano, C.L., D. Romano, and N. Logoluso, *LOW-INTENSITY PULSED ULTRASOUND FOR THE TREATMENT OF BONE DELAYED UNION OR NONUNION: A REVIEW.* Ultrasound in Medicine and Biology, 2009. **35**(4): p. 529-536.

116. Nolte, P.A., *et al*., *Low-intensity pulsed ultrasound in the treatment of nonunions.* Journal of Trauma-Injury Infection and Critical Care, 2001. **51**(4): p. 693-702.

117. Takikawa, S., *et al*., *Low-intensity pulsed ultrasound initiates bone healing in rat nonunion fracture model.* Journal of Ultrasound in Medicine, 2001. **20**(3): p. 197-205.

118. Takayama, T., *et al*., *Low-intensity pulsed ultrasound stimulates osteogenic differentiation in ROS 17/2.8 cells.* Life Sciences, 2007. **80**(10): p. 965-971.

119. Pounder, N.M. and A.J. Harrison, *Low intensity pulsed ultrasound for fracture healing: A review of the clinical evidence and the associated biological mechanism of action.* Ultrasonics, 2008. **48**(4): p. 330-338.

120. Costa, V., *et al*., *Osteogenic commitment and differentiation of human mesenchymal stem cells by low-intensity pulsed ultrasound stimulation.* Journal of Cellular Physiology, 2018. **233**(2): p. 1558-1573.

121. Jaiswal, N., *et al*., *Osteogenic differentiation of purified, culture-expanded human mesenchymal stem cells in vitro.* Journal of Cellular Biochemistry, 1997. **64**(2): p. 295-312.

122. Uddin, S.M.Z. and Y.X. Qin, *Enhancement of Osteogenic Differentiation and Proliferation in Human Mesenchymal Stem Cells by a Modified Low Intensity Ultrasound Stimulation under Simulated Microgravity.* Plos One, 2013. **8**(9).

123. Zhou, X., *et al*., *Improved Human Bone Marrow Mesenchymal Stem Cell Osteogenesis in 3D Bioprinted Tissue Scaffolds with Low Intensity Pulsed Ultrasound Stimulation.* Scientific Reports, 2016. **6**.

124. Sun, J.S., *et al*., *In vitro effects of low-intensity ultrasound stimulation on the bone cells.* Journal of Biomedical Materials Research, 2001. **57**(3): p. 449-456.

125. Yang, R.S., *et al*., *Regulation by ultrasound treatment on the integrin expression and differentiation of osteoblasts.* Bone, 2005. **36**(2): p. 276-283.

126. Angle, S.R., *et al*., *Osteogenic differentiation of rat bone marrow stromal cells by various intensities of low-intensity pulsed ultrasound.* Ultrasonics, 2011. **51**(3): p. 281-288.

127. Becerra, G.D., *et al*., *Evaluation of mesenchymal stem cell proliferation using different low intensity pulsed ultrasound intensities.* International Journal of Morphology, 2012. **30**(2): p. 621-626.

128. Kusuyama, J., *et al*., *Low Intensity Pulsed Ultrasound (LIPUS) Influences the Multilineage Differentiation of Mesenchymal Stem and Progenitor Cell Lines through ROCK-Cot/Tpl2-MEK-ERK Signaling Pathway.* Journal of Biological Chemistry, 2014. **289**(15): p. 10330-10344.

129. Sakurakichi, K., *et al*., *Effects of timing of low-intensity pulsed ultrasound on distraction osteogenesis.* Journal of Orthopaedic Research, 2004. **22**(2): p. 395-403.

130. Yoon, J.H., *et al*., *Introducing pulsed low-intensity ultrasound to culturing human umbilical cord-derived mesenchymal stem cells.* Biotechnology Letters, 2009. **31**(3): p. CP15-335.

131. Hu, J.Z., *et al*., *Combined Application of Low-Intensity Pulsed Ultrasound and Functional Electrical Stimulation Accelerates Bone-Tendon Junction Healing in a Rabbit Model.* Journal of Orthopaedic Research, 2014. **32**(2): p. 204-209.

132. Kang, K.S., *et al*., *Effects of combined mechanical stimulation on the proliferation and differentiation of pre-osteoblasts.* Experimental and Molecular Medicine, 2011. **43**(6): p. 367-373.

133. Hsu, H.C., *et al*., *Ultrasound induces cyclooxygenase-2 expression through integrin, integrin-linked kinase, Akt, NF-kappa B and p300 pathway in human chondrocytes.* Cellular Signalling, 2007. **19**(11): p. 2317-2328.

134. Iwashina, T., *et al*., *Low-intensity pulsed ultrasound stimulates cell proliferation and proteoglycan production in rabbit intervertebral disc cells cultured in alginate.* Biomaterials, 2006. **27**(3): p. 354-361.

135. Jones, D.B., *et al*., *BIOCHEMICAL SIGNAL TRANSDUCTION OF MECHANICAL STRAIN IN OSTEOBLAST-LIKE CELLS.* Biomaterials, 1991. **12**(2): p. 101-110.

136. Liu, S.L., *et al*., *Investigation into the Effect of Acoustic Radiation Force and Acoustic Streaming on Particle Patterning in Acoustic Standing Wave Fields.* Sensors, 2017. **17**(7).

137. Simmons, C.A., *et al*., *Cyclic strain enhances matrix mineralization by adult human mesenchymal stem cells via the extracellular signal-regulated kinase (ERK1/2) signaling pathway.* Journal of Biomechanics, 2003. **36**(8): p. 1087-1096.

138. Arnsdorf, E.J., *et al*., *Mechanically induced osteogenic differentiation - the role of RhoA, ROCKII and cytoskeletal dynamics.* Journal of Cell Science, 2009. **122**(4): p. 546-553.

139. Baker, K.G., V.J. Robertson, and F.A. Duck, *A review of therapeutic ultrasound: Biophysical effects.* Physical Therapy, 2001. **81**(7): p. 1351-1358.

140. Hiyama, A., *et al*., *Synergistic effect of low-intensity pulsed ultrasound on growth factor stimulation of nucleus pulposus cells.* Journal of Orthopaedic Research, 2007. **25**(12): p. 1574-1581.

141. Puts, R., *et al*., *In-vitro Stimulation of Cells of the Musculoskeletal System with Focused Low-Intensity Pulsed Ultrasound (FLIPUS): Analyses of Cellular Activities in Response to the Optimized Acoustic Dose*, in *2014 Ieee International Ultrasonics Symposium*. 2014. p. 1630-1633.

142. Binderman, I., Z. Shimshoni, and D. Somjen, *BIOCHEMICAL PATHWAYS INVOLVED IN THE TRANSLATION OF PHYSICAL STIMULUS INTO BIOLOGICAL MESSAGE.* Calcified Tissue International, 1984. **36**: p. S82-S85.

143. Somjen, D., *et al*., *BONE REMODELING INDUCED BY PHYSICAL STRESS IS PROSTAGLANDIN-E2 MEDIATED.* Biochimica Et Biophysica Acta, 1980. **627**(1): p. 91-100.

144. Takeuchi, R., *et al*., *Low-intensity pulsed ultrasound activates the phosphatidylinositol 3 kinase/Akt pathway and stimulates the growth of chondrocytes in three-dimensional cultures: a basic science study.* Arthritis Research & Therapy, 2008. **10**(4).

145. Zhang, P., *et al*., *Osteogenic response of mesenchymal stem cells to continuous mechanical strain is dependent on ERK1/2-Runx2 signaling.* International Journal of Molecular Medicine, 2012. **29**(6): p. 1083-1089.

146. Kremkau, F.W., *ULTRASOUND - BIOLOGICAL EFFECTS AND POTENTIAL HAZARDS - WILLIAMS,AR.* New England Journal of Medicine, 1984. **311**(7): p. 478-479.

Chapter 2 Detection of Heterotopic Ossification Using Spectral Ultrasound Imaging

2.1 Introduction

Patients with severe burns, spinal cord injuries, and orthopedic interventions are at significant risk for developing heterotopic ossification (HO).[1-3] More than 65% of major combat injuries and over 10% of patients who undergo invasive joint surgery develop HO.[4] Animal models of traumatic HO have been tailored to create reproducible HO after polytrauma.[5,6] Current treatment strategies are lacking, and even after a technically successful surgical extirpation, over 75% of patients have difficulty maintaining their range of motion.[7] The disruption of physiological structures by HO results in significant morbidity including limited range of motion, pain, and disability in performing activities of daily living.[4,5] Currently, a definitive diagnosis of HO relies on the use of CT and MRI to locate and visualize ectopic lesions.[2,3] Unfortunately, however, these imaging modalities are expensive, and diagnosis is oftentimes delayed as HO is only visualized after it has already formed and matured. In these cases, the critical therapeutic window for non-operative treatment has passed and surgery becomes the only definitive option.[6] Unfortunately, however, surgery is limited by incomplete restoration of range of motion and frequent recurrence in approximately 50-90% of cases.[1]

The early diagnosis of HO is critically important for multiple reasons.[7] Recent studies have analyzed newer strategies to detect early HO in congenital and traumatic forms.[8-10] With improved diagnostic technologies for patients who are at high risk for HO, patients with severe burns and

blast injuries may be candidates for medical management as opposed to surgical intervention; more specifically, identifying a technology that can detect HO within 1-3 weeks after initiation will enable the implementation of pharmacologic strategies for early treatment instead of surgery.[8] In animal models, the pharmacologic modulation of BMP signaling demonstrated the greatest reduction in HO when administered 0-2 weeks after injury, and less effect when administered 3-6 weeks after injury.[8] Current diagnostic modalities including CT and MRI are inadequate for the early detection of HO; other developing technologies such as Raman spectroscopy are effective in discriminating endochondral bone development, but have yet to be effectively translated to the clinic.[9]

Spectral ultrasound imaging (SUSI), a technique extended from conventional grayscale B-mode ultrasound imaging, retains the non-invasiveness of ultrasound imaging yet is capable of obtaining objective parameters related to the composition and structural properties of tissues based on an already ubiquitous technology.[11-13] While some studies have tested the use of conventional grayscale ultrasound imaging for the detection of HO, it is not surprising that these studies have proven that ultrasound is effective for visualizing HO only once it has already formed or in the presence of limitations in range of motion, rather than at early time points.[14-16] Conventional grayscale ultrasound imaging primarily provides morphological information of tissue cross-sections with millimeters of spatial resolution. SUSI, on the other hand, utilizes calibrated spectra based on radio-frequency backscattered signals to extract parameters that are system- and operator independent; SUSI provides quantitative and objective tissue characterization.[17] Spectral characteristics including acoustic scatter diameter in addition to other spectral parameters enable detection of tissue compositional changes in addition to morphology. These parameters can be mapped to generate specimen-specific reference ranges. Although high frequency ultrasound is

not suitable for use in highly mineralized tissues due to limited penetration and attenuation, SUSI represents a unique advancement for the visualization of developing foci of bone in soft tissue such as HO. Given previous results that have validated the use of spectral parameters of quantitative spectral ultrasound imaging in characterizing solid particles in inhomogeneous materials and improving the early detection of pathologies including breast cancer and atherosclerotic plaques, it is possible that this technology will provide value for the early detection of HO.[18,19,20]

In this study, we validate the use of SUSI in the identification of musculoskeletal tissues, and the visualization of ectopic bone at multiple stages of its development in a mouse model of traumatic HO. We investigated the differences in timing between injury and initial detection of HO using SUSI versus the current gold standard of imaging, micro CT. The use of SUSI has the potential to expand the diagnostic options available to patients with HO, and can also enable the use of additional pharmacologic agents against HO in a timelier manner than what is currently possible.

2.2 Materials and Methods

2.2.1 Burn Injury and Achilles Tenotomy Models

To evaluate the ability of SUSI to detect HO, we used our validated burn/tenotomy model.[19] Two groups of studies were performed. First, a longitudinal analysis was conducted to compare an injured limb (left) to an uninjured limb (right) as a control (n=5 mice per group). This specific comparison was selected as a correlate to clinical scenarios in which patients commonly present with one injured limb using imaging from the injured side as a comparison to the uninjured side to detect pathology. Longitudinal analysis was conducted to compare the accuracy and timing

of detection using SUSI versus micro CT. Additionally, static time point analyses were performed to compare the uninjured limb (right) to the injured limb with HO (left) using SUSI, CT, and histology at 1, 2, 4, and 9 weeks after injury (n=3-5 mice per time point). To perform the burn/tenotomy surgeries, mice were anesthetized using isofluorane and pre-treated with buprenorphine. The dorsum of each mouse was shaved, and a metal block heated to 60˚Celsius was placed at this site for 18 seconds. Next, a pair of scissors was used to make an incision at the site of the Achilles' tendon. Dissection was carried down to visualize the tendon which was then sharply divided. The skin incision was closed with a 4-0 vicryl suture. No injury was performed on the right limb for comparison.

Next, in order to ensure that the hyperechoic foci detected at one week post-injury were HO rather than simple pockets of edema, we compared the findings of SUSI using two different injury models. Animals underwent either burn/tenotomy (n=5) or burn with skin incision without tenotomy (n=5). This skin incision model results in the presence of edema without HO, and can thus be used to define the ability of SUSI to distinguish between HO and edema at early time points. SUSI was performed at one week post-injury. For animals treated with skin incision only, mice were anesthetized, shaved, and pre-treated with buprenorphine as above. A scissors was used to make a small skin incision at the site of the Achilles' tendon, but the tendon itself was not divided. The skin incision was closed with a 4-0 vicryl suture.

2.2.2 Ultrasound Imaging and Data Acquisition

Mice were placed on examination stage and anesthetized with 2% isoflurane in oxygen during ultrasound imaging. Animals were placed on the examination stage with similar orientation, and the skin surface was brought to the focus of the ultrasound probe to optimize the imaging quality. Excessive hair surrounding the heel was removed and ultrasound gel was applied on the

skin at the site as a coupling agent. Imaging was performed with a high-resolution small animal ultrasound imaging unit, Vevo 770 System (Visualsonics, Toronto, Canada) and a 55-MHz center frequency single element transducer (Vevo 708 scan head; 20-75 MHz -6 dB bandwidth; 30 μm axial resolution; 70 μm lateral resolution; 4.5 mm focal distance; 1.5 mm -6 dB focal depth; 100% transmit power). Both heels of each mouse were imaged with B-mode, 3D scan mode, and radiofrequency mode to acquire backscattered ultrasound signals for SUSI processing. Cross-section images were obtained under B-mode. A 6 mm range around the calcaneus was scanned with a step size of 30 μm, and 3D images were reconstructed. Backscattered radio frequency (RF) signals were acquired using the RF mode with a 200 μm step size and a 5-millimeter scan range. 3D scanning was accomplished with an automated scanning motor on the system with a 30 μm distance between neighboring frames. This non-invasive imaging procedure requires less than 15 min for each imaging site. Grayscale images were reconstructed from the radio-frequency signals.

2.2.3 High Frequency Spectral Ultrasound Analysis

Grayscale values GS(y, z) and images were computed as previously mentioned.[20] Briefly, raw backscattered RF data was Hilbert transformed to obtain the complex analytical signal p(y, z). Grayscale B-mode images are reconstructed using the logarithm of amplitude envelop the signal. Quantitatively, grayscale values (GS) were determined as the mean absolute value of the signal over the selected region of interest as:

$$GS(y,z) = \log_{10}|p(y,z)|. \quad \textit{Equation 2-1}$$

Analysis of the ultrasound power spectrum has been discussed and applied for detecting mineralization in engineered tissue constructs previously.[21] Similar to our previous work on detecting mineralization, we were targeting ossification at the early stage, in which the mineral

nuclei in the soft tissue didn't yield multiple backscattering as mature bone and the spherical scatterer assumption can be applied to yield a first-order approximation. The power spectrum of each RF scan line in an image was calculated by taking the Fast Fourier Transform of the segment of signals gated by a hamming window of 0.2 μs sliding with a 0.1 us offset. To remove system-dependence, the power spectrum of the gated signals was calibrated by dividing it by a calibration power spectrum, which was obtained from a perfect reflector (oil-water interface). Spectral parameters slope (m) and mid-band fit (MBF) were determined by using linear regression to the calibrated power spectrum within a -9 dB bandwidth. Microstructural parameters such as the acoustic scatterer diameter, a, which represents an effective size of the acoustic scatters in tissue, can be assessed from the spectral parameters including the slope m, the geometry index (n), the center frequency of the imaging transducer (f_c), and bandwidth of the transducer (b), and is given by:

$$a = 2 * \sqrt{0.25n \frac{[b-(1-\frac{b^2}{4})]}{b^3 f_c^2} - \frac{m}{105.5 f_c}}. \quad \textit{Equation 2-2}$$

Acoustic concentration, which is denoted as CQ^2, a product of scatter concentration and the square of the acoustic impedance of the scatters, depends on MBF, scatterer diameter (a) and a shape dependent factor (E), and is defined as:

$$\mathrm{CQ}^2 = \frac{\exp(0.23\left(MBF - g_1 n - g_2(\frac{a}{2})^2\right))}{E a^{2(n-1)}}, \quad \textit{Equation 2-3}$$

$$g_1(f_c, b) = 4.34[\ln(f_c \left(1 - \frac{b^2}{4}\right)^{0.5} \left(\frac{2+b}{2-b}\right)^{\frac{1}{b}}) - 1], \quad \textit{Equation 2-4}$$

$$g_2(f_c, b) = -76.9 f_c^2 (3 + \frac{b^2}{4}). \quad \textit{Equation 2-5}$$

The average scatterer diameter (ASD) and average acoustic concentration (AAC) is calculated as the average value of the scatterer size (a), and the acoustic concentration(CQ^2)

respectively in the chosen region of interest (ROI). Due to the large span of the CQ^2 values, AAC values are represented in decible scale[22]. The values of the scatterer diameter and the acoustic concentration were assigned to each pixel in the selected ROI and overlaid on the grayscale image to create parametric images representing these parameters.

2.2.4 Micro-Computed Tomography

Micro CT was performed at each time point at which SUSI was performed GE Healthcare Biosciences, using 80 kVp, 80 mA, and 1,100 ms exposure). The anatomic and spatial orientation of HO was characterized using a calibrated imaging protocol as previously described. Three-dimensional reconstructions were performed at a threshold of 800 Houndsfield Units using anatomic landmarks and observer identification to quantify and define the original cortical bone structures. This defined bone mineral within the soft tissues was quantified as HO.[23]

2.2.5 Histology Staining and Image Acquisition

Animals in each respective experimental arm were euthanized following the conclusion of sonographic and radiographic assays. Harvested hind limbs were fixed in 10% formalin for 24 hours at 4°C. Specimens were subsequently decalcified using 4% EDTA for 3 weeks at 4°C, paraffin processed, and cut in 5μm transversely oriented sections. Specimens were then deparaffinized, rehydrated, and stained using H&E and Movat's Pentachrome formulations. Stained slides were imaged using an Olympus Bx-51 microscope equipped with an Olympus DP-70 high-resolution digital camera.[24]

2.2.6 Statistical Test

ROIs in at least 5 frames from each limb were identified using grayscale images and quantified with GS value and spectral parameters. Results were presented as mean ± SEM. Statistical comparisons of parameters between groups and time points were made using Student's t-test for paired samples and the differences were considered significant at a level of $p<0.05$. In our initial pilot study, the average acoustic concentration (AAC; (dB[mm^{-3}]) of HO was 37.82 ± 2.41 and 29.34 ± 3.81 for control samples. To be able to detect a true difference between these groups with 80 percent certainty using an alpha of .05, at least 4 mice per group are necessary to ensure adequate power. Therefore, five mice per group were included in the subsequent analysis groups.

2.3 Results

2.3.1 The Mineral Density of Post-Traumatic HO Foci at Early Time Points Indicates a Composition between Cartilage and Bone

To assess the ability of SUSI to distinguish between various musculoskeletal tissue types, samples of bone, cartilage, tendon, and muscle were imaged *ex vivo* (**Figure 2-1**). Clear distinctions between these tissue types were observed with SUSI (**Figure 2-1**A). Bone was the most echogenic, with the highest grayscale values (GS), and was also associated with the high acoustic concentration (AAC: 86.3±1.02, 79.2±1.4, 76.8±1.22 dB[mm^{-3}] for femur, calcaneus, and tibia respectively). Fibrocartilage was less echogenic than bone with a lower AAC (49.2±1.34 dB[mm^{-3}]), but was more mineralized than soft tissues such as tendon (39.7±0.4 dB[mm^{-3}]) and muscle (30.2±1.34 dB[mm^{-3}]) (**Figure 2-1**B). In particular, HO has a higher AAC and ASD than cartilage, but less than bone. This indicates the HO development at week 1 is at a level of

mineralization between the calcaneus and the cartilage. These findings are consistent with histology demonstrating the progression of HO in previous studies.[25, 24] Interestingly, although the grayscale values for all tissue types are similar except muscle, the AAC values exhibited much more differences (**Figure 2-1**B and C). In addition, while the ASD values may be similar (**Figure 2-1**C), the tissue types can be easily differentiated by the AAC values, indicating that SUSI is sensitive in detecting the tissue types based on tissue composition. Importantly, SUSI revealed tissue specific signatures of these samples (**Figure 2-1**C) based on both ACC and ASD values, with larger scatter size and higher concentration for more mineralized tissues such as bone.

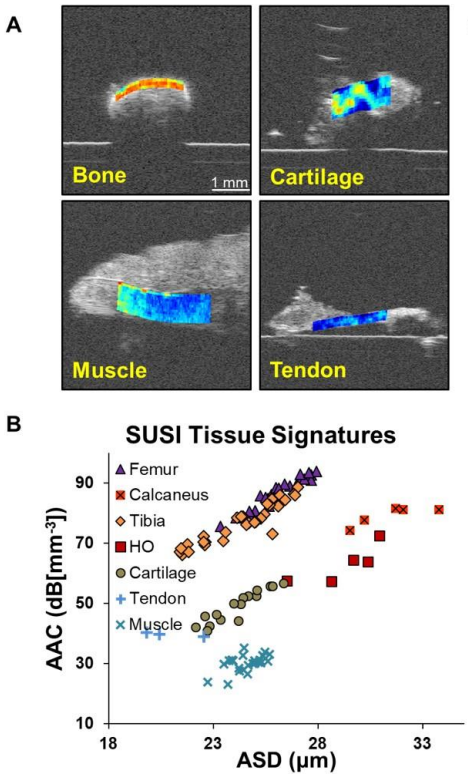

C

Tissue Type	GS	ASD (μm)	AAC (dB[mm]$^{-3}$)
Muscle	25.15 ± 1.33	24.60 ± 0.43	30.21 ± 1.58
Tendon	48.27 ± 1.90	20.93 ± 0.83	39.70 ± 0.40
Cartilage	46.68 ± 0.67	24.15 ± 0.32	49.15 ± 1.34
HO	**42.89 ± 1.62**	**29.23 ± 0.78**	**63.19 ± 2.80**
Tibia	56.22 ± 0.32	24.35 ± 0.33	76.78 ± 1.22
Calcaneus	50.92 ± 1.99	31.47 ± 0.74	79.19 ± 1.40
Femur	60.23 ± 0.42	26.00 ± 0.24	86.33 ± 1.02

Figure 2-1. Characterization of different types of musculoskeletal tissue by SUSI. A. Grayscale images of calcaneus, cartilage, muscle and tendon overlaid with acoustic concentration values (scale bar: 1 mm). B. Table summarizes the mean ± SEM of grayscale intensity, average scatterer diameter (ASD) and average acoustic concentration (AAC) of various musculoskeletal tissue types ($n \geq 3$). Heterotopic ossification at 1 week post injury shows AAC values between cartilage and calcaneus, indicating a mineralization level between the two. C. Scatter plot of the ASD and AAC values of various tissue types. Different tissue types can be differentiated by the AAC values.

2.3.2 SUSI Differentiates between Post-Traumatic HO in the Injury Model versus Edema in the Skin Incision Model

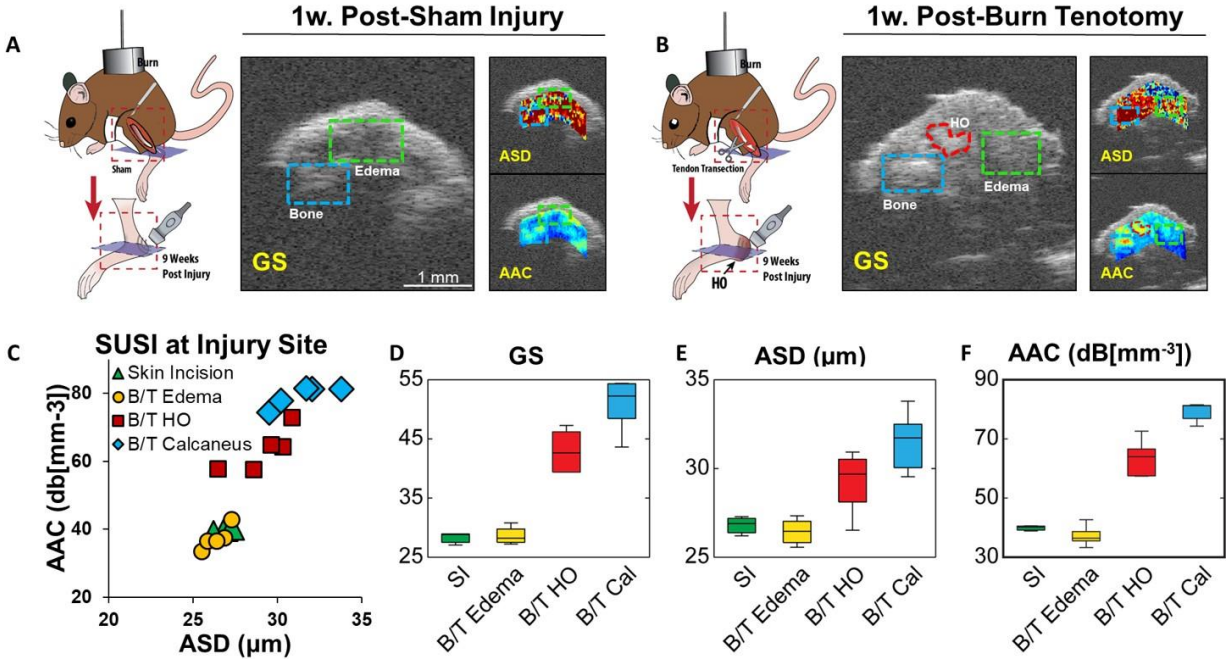

Figure 2-2. SUSI comparison of the skin incision (SI) model and the burn/tenotomy model at 1 week post injury. A. As shown in the grayscale image, animal underwent burn and skin incision with tenotomy developed edema (green box) without formation of ectopic bone (scale bar: 1 mm). Low values of AAC are shown in the edema region. B. In animals underwent burn and tenotomy, both edema (green box) and HO (red ROI) formed in the space between bone (blue box) and skin. The HO foci exhibited AAC and ASD values between bone and edema. C. Scatter plot of ASD and AAC values of edema in skin incision model, edema, HO and calcaneus in B/T model (n = 5). D-F. Bar plots of grayscale intensity, ASD and AAC values in the skin incision edema, B/T edema, HO and Calcaneus foci. Edema in both models showed similar ASD and AAC. HO foci showed ASD and AAC values in between edema and bone.

Injured and sham-treated animals were imaged at one-week post-injury to test whether that SUSI was able to distinguish between edema and HO at very early time points during which time these two structures may be mistaken for one another on imaging. Reconstructed grayscale images from the RF data for the two HO models are presented in **Figure 2-2**A and **Figure 2-2**B. Differences in the two models were also revealed in the parametric images (**Figure 2-2**A and B**)**. The quantitative results show significantly higher grayscale value, ASD and AAC value in the HO foci (GS: 42.9±1.6, ASD: 29.2±0.8 μm, AAC: 63.2±2.8 dB[mm^{-3}], n = 5) relative to the

surrounding edema (GS: 28.7±0.7, ASD: 26.4±0.3 μm, AAC: 37.2±1.5 dB[mm^{-3}], n = 5) in the B/T model. The calcaneus has the highest value in all three parameters (GS: 50.9±2.0, ASD: 31.5±0.7 μm, AAC: 79.2±1.4 dB[mm^{-3}], n = 5). In the skin incision only model, no ROI with high AAC/ASD values were detected. The edema region in the sham-treated limb show similar grayscale, ASD and AAC value as the edema in the injured limb (GS: 28.3±0.6, ASD: 26.8±0.3 μm, AAC: 39.9±0.5 dB[mm^{-3}], n = 3). As shown clearly in the SUSI signature (**Figure 2-2**C), our results comparing the burn/tenotomy limb with the skin incision limb demonstrate that SUSI is able to accurately distinguish between two different injury models. Notably, this technology both qualitatively and quantitatively differentiates between edema and HO as early as one week post-injury (**Figure 2-2**).

2.3.3 SUSI Visualizes post-traumatic HO foci as Early as One Week after Injury and Demonstrate Progression to Mature over Time

We performed serial imaging at 1, 2, 4, and 9 weeks to demonstrate consistency and accuracy of SUSI over time in terms of the ability to identify HO.

As shown in **Figure 2-3**, in the control limb (right limb), both skin and calcaneus maintain a high level of ASD and ACC consistently over time. Connective tissue next to the calcaneus is less echogenic, and has a lower ASD (27.1±0.7 μm) and AAC (47.4±1.7 dB[mm^{-3}]) values in the region. No hyperechoic foci are seen at any time points in the uninjured model. However, on the injured side, parametric images demonstrate that the HO foci are present as early as one week after injury, and have much higher ACC and larger ASD compared to the surrounding edema, The AAC value for the HO foci increases from 63.2±2.8 to 67.7±1.3 dB[mm^{-3}] from week 1 to week 9, while the surrounding edema has an AAC value of 37.2±1.5 and 40.5±1.8 dB[mm^{-3}] at week 1 and week 9. This indicates that HO on SUSI is consistently different from edema longitudinally at all time-

points. Moreover, while the grayscale values are different between the control and HO model at week 9, only the SUSI ACC values are distinct for the control and HO model as early as week 1. Furthermore, the HO foci at week 9 have slightly higher acoustic concentration compared to earlier time points, demonstrating greater mineralization of these tissues with time.

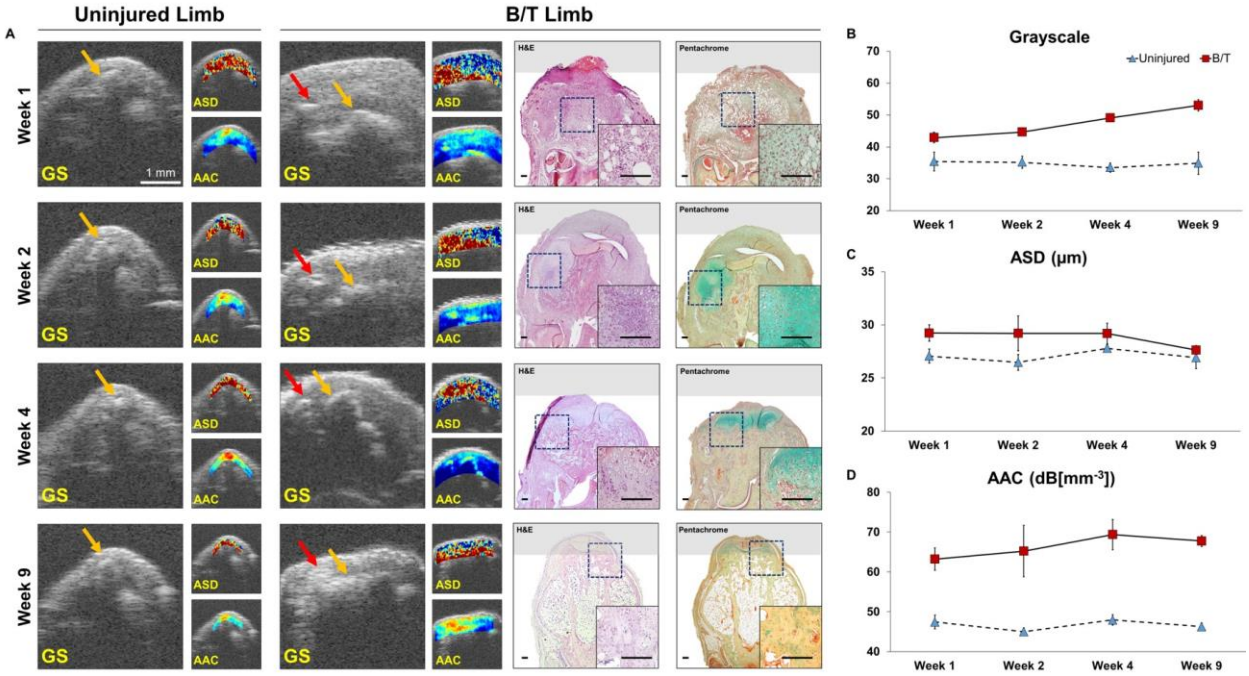

Figure 2-3. SUSI monitors longitudinal tissue development in the uninjured and B/T limb at 1, 2, 4 and 9 weeks post injury. A. In the uninjured limb at all four time points, no edema formed and the calcaneus (yellow arrow) was located beneath the skin. In the B/T limb, edema formed and its volume gradually decreased over time (scale bar: 1 mm). HO (red arrow) can be visualized at 1 week post injury. The AAC-overlaid images show high intensity at the bone and HO foci. Corresponding H&E and Pentachrome staining images confirmed the presence of cartilage deposition and inflammation. B-D. Mean ± SEM (n=5) of grayscale intensity, ASD and AAC values are shown for the connective tissue region (between skin and bone) in the uninjured limb, and the HO foci (yellow arrow) in the B/T limb at week 1, 2, 4 and 9 post injury. GS, ASD and AAC values of the HO foci are higher than that in the uninjured limb at all four time points.

In addition, compared to the calcaneus (AAC value of 79.2±1.4 dB[mm^{-3}] at week 1, the HO foci have slightly lower acoustic concentration indicating a less dense mineral density in the HO foci. The progression of HO over time is clearly evident qualitatively based on the evolution of the

hyperechoic foci from weeks 1-9 post-injury (**Figure 2-3**B-D). Additionally, the presence of hyperechoic foci on SUSI correlates with early cartilage deposits and inflammation on histology.

2.3.4 SUSI Identifies Post-Traumatic HO 3-5 Earlier than Micro-CT and is Consistent with Histological Findings

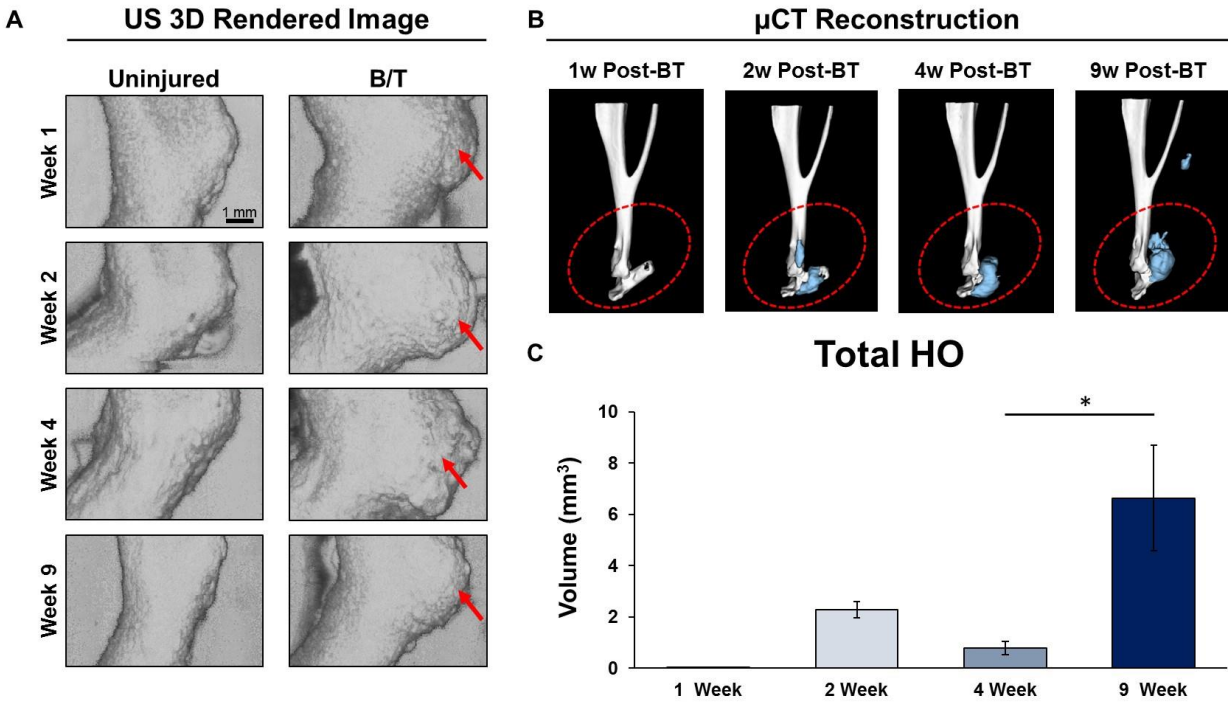

Figure 2-4. Concurrent SUSI and micro CT of the uninjured and B/T limbs at 1, 2, 4, and 9 weeks post injury. A. 3D rendered ultrasound images of the uninjured limbs and the B/T limbs (scale bar: 1 mm). Inflammation and HO formation in the B/T were reflected by the tissue volume increase compared to the uninjured limb. B. HO was visualized under micro CT 4 weeks post injury. Blue areas shows the newly formed ectopic bone. C. Mean ± SEM (n=5) of the volume of ectopic bone measured with reconstructed micro CT. Graphic comparison of HO development at 1 week (0.01 ± 0.00 mm^3, n=6), 2 weeks (2.29 ± 0.31 mm^3, n=3), 4 weeks (0.79 ± 0.26 mm^3, n=4), and 9 weeks post-injury (6.64 ± 2.07, n=5). Difference in detectable HO volume at 4 v. 9 weeks is statistically significant (p=0.0465, two-sided student's t-test).

Currently, micro CT serves as the gold standard to detect HO. HO is reliably visualized at approximately 4-6 weeks post-injury using micro CT (**Figure 2-4**). Histologically, HO begins as small inflammatory infiltrates which subsequently coalesce into uncalcified regions at 1 week, and transition to calcified and uncalcified fibrocartilage islands approximately 3 weeks after the injury.

Approximately 4-6 weeks after the initial injury, these networks of cartilage become bone through the process of endochondral ossification. Using SUSI, we were able to visualize ectopic bone within the calcaneal region of each mouse as early as one week after injury (**Figure 2-4**A). The findings of SUSI at early time points and late time points correlated with the presence of HO on histology at all time-points and on micro CT at 9 weeks (**Figure 2-4**B and C). Given the known progression of HO from an inflammatory lesion at 1-2 weeks, to cartilage at 3 weeks, and finally HO after 6 weeks, it is likely that SUSI captures the inflammatory foci that ultimately progress to cartilage and bone at later time points. None of the control limbs demonstrated these inflammatory infiltrates or HO according to micro CT or SUSI (**Figure 2-4**). 3D reconstructions performed on SUSI demonstrate that HO can be visualized 3-5 weeks earlier than on micro CT.

2.4 Discussion

Timely initiation of early medical management strategies against HO remain ineffective due to a lack of diagnostic strategies available to accurately detect and visualize HO within 1-2 weeks of injury. In this study, we validate the use of SUSI for the early detection of HO within one week of inciting injury using two animal models. When compared to more traditional modalities of imaging including micro CT, SUSI visualized and quantified the presence of HO five weeks earlier, consistent with the formation of HO as visualized by histology. The system and operator independent nature and quantitative output of SUSI simplify its use and allows for providers with varying degrees of training to benefit equally from such advancements. As such, based on the result of our *in vivo* testing, we believe that SUSI represents a promising tool to enable the early detection of HO. Earlier detection may enable the initiation of early pharmacologic treatment among high-risk patients to mitigate the need for surgery. Specifically, we foresee this technology being used in burn patients who develop HO in the elbow >90% of the time. Future

studies to validate this technology in deeper tissue forms of HO such as hip replacement are needed. To achieve more penetration depth, ultrasound probe with lower center frequency can be used with the cost in imaging resolution, yet the power spectral analysis has been validated with ultrasound center frequency as low as 5 MHz.[17]

Traditional ultrasound imaging alone has been validated as a screening tool to detect ectopic bone among patients with neurogenic HO. For example, Falsetti *et al.* stated that bedside ultrasound is a safe, non-invasive, cost-effective screening tool important for screening patients with acquired forms of brain injury.[26] Importantly, however, one of the main limitations of this study is the lack of generalizability, as one operator performed all measurements in this study precluding the assessment of inter-operator reliability. In this regard, SUSI represents an improvement beyond traditional ultrasound techniques because SUSI obtains parameters from calibrated spectrum which are objective and quantitative; as these parameters are related to the intrinsic properties of tissues, SUSI allows for greater utility and without the need to rely on subjective graphic assessments. Specifically, SUSI provides parameters that represent tissue properties beyond grayscale imaging intensity. As shown in this study, the utility of SUSI is also demonstrated by its ability to perform comprehensive, objective visualizations of microstructural tissue properties to a much greater degree than conventional ultrasound.[27-31] Such objectivity enhances the application and utility of this technology into clinical environments that are currently founded upon principles of clinical judgement and experience. With regards to patients at high risk for HO specifically after burns and blast injuries, targeted forms of screening may be instituted to promote early detection given that the most common sites of HO have been clearly defined in the past. By implementing standardized imaging procedures at these sites specifically, it may be possible to diagnosis HO earlier than current imaging modalities permit. This process may also be

broadened to include imaging for symptomatic regions in patients who present with signs concerning for the development of HO.

Conventional B-mode grayscale values are not absolute and dependent on imaging settings and specific systems and interpretation of these images are not absolute and unable to compare with different studies. Therefore, such qualitative results are inevitably subjected to operator variation. SUSI offers a quantitative method that is system- and operator independent because it uses acoustic scatterer diameter (ASD) and acoustic concentration (AAC) extracted from the backscattered signals to distinguish tissue changes within the region of interest of the injured and control limbs as early as possible for HO diagnosis.

While there are limitations to consider, the strength of our findings lies in the identification of a non-invasive technology that detects the presence of HO much earlier than traditional, gold standard modalities commonly used today. Our study is limited by the restrictions imposed on the serial imaging of animals within our institution. To address this, we performed both longitudinal and individual time point analyses to ensure that we were performing serial evaluations from multiple perspectives using both SUSI and micro CT. Consequently, our results demonstrate that SUSI correlated with micro CT at both final and early time points. Additionally, the overall generalizability of our findings can be enhanced by validating the use of SUSI in other musculoskeletal pathologies as well. The theoretical model we applied herein involves assumption of spherical scatterers, which may not be optimal for some tissue types. Nevertheless, this model provides a first order approximation of more complex scatterer geometry. In addition, the spherical sphere assumption provides an effective radius that can be used to describe any given scatterer. For future work, other theoretical models of various scatterer geometry and dimension, will be investigated.[32, 33] Despite these limitations, the use of SUSI to detect early post-traumatic HO is

significant. SUSI represents an effective, non-invasive, potentially cost-effective diagnostic strategy that can facilitate the early diagnosis of HO.

2.5 Conclusion

In this study, we demonstrate the utility of SUSI in detecting post-traumatic HO as early as one week post-injury in two models. Application of this technology will facilitate the prompt diagnosis of HO based on both quantitative and objective data. Early diagnosis may allow for timely initiation of treatments that may negate the need for surgical intervention in the future. Using quantitative metrics and advanced, yet noninvasive imaging strategies, SUSI represents an important technological advancement for its application to visualizing ectopic bone formation.

2.6 References

1. Shehab D, Elgazzar AH, Collier BD. Heterotopic ossification. *J Nucl Med.* 2002;43(3):346-353.
2. Ranganathan K, Loder S, Agarwal S, *et al*. Heterotopic Ossification: Basic-Science Principles and Clinical Correlates. *The Journal of bone and joint surgery American volume.* 2015;97(13):1101-1111.
3. Vanden Bossche L, Vanderstraeten G. Heterotopic ossification: a review. *Journal of rehabilitation medicine.* 2005;37(3):129-136.
4. Potter BK, Burns TC, Lacap AP, Granville RR, Gajewski DA. Heterotopic ossification following traumatic and combat-related amputations. Prevalence, risk factors, and preliminary results of excision. *J Bone Joint Surg Am.* 2007;89(3):476-486.
5. Peterson JR, Okagbare PI, De La Rosa S, *et al*. Early detection of burn induced heterotopic ossification using transcutaneous Raman spectroscopy. *Bone.* 2013;54(1):28-34.
6. Pavey GJ, Qureshi AT, Hope DN, *et al*. Bioburden Increases Heterotopic Ossification Formation in an Established Rat Model. *Clinical orthopaedics and related research.* 2015.
7. Hunt JL, Arnoldo BD, Kowalske K, Helm P, Purdue GF. Heterotopic ossification revisited: a 21-year surgical experience. *J Burn Care Res.* 2006;27(4):535-540.
8. Onat SS, Ozisle Z, Orhan A, Akman B, Koklu K, Ozcakar L. Ultrasonographic diagnosis of heterotopic ossification and secondary nerve entrapments in a patient with spinal cord injury. *Med Ultrason.* 2017;19(3):338-339.

9. Eekhoff EMW, Botman E, Coen Netelenbos J, *et al*. [18F]NaF PET/CT scan as an early marker of heterotopic ossification in fibrodysplasia ossificans progressiva. *Bone.* 2017.

10. Al Mukaddam M, Rajapakse CS, Pignolo RJ, Kaplan FS, Smith SE. Imaging assessment of fibrodysplasia ossificans progressiva: Qualitative, quantitative and questionable. *Bone.* 2017.

11. Gudur M, Rao RR, Hsiao YS, Peterson AW, Deng CX, Stegemann JP. Noninvasive, Quantitative, Spatiotemporal Characterization of Mineralization in Three-Dimensional Collagen Hydrogels Using High-Resolution Spectral Ultrasound Imaging. *Tissue Eng Part C-Me.* 2012;18(12):935-946.

12. Gudur MSR, Rao RR, Peterson AW, Caldwell DJ, Stegemann JP, Deng CX. Noninvasive Quantification of In Vitro Osteoblastic Differentiation in 3D Engineered Tissue Constructs Using Spectral Ultrasound Imaging. *PloS one.* 2014;9(1).

13. Deng CX, Hong XW, Stegemann JP. Ultrasound Imaging Techniques for Spatiotemporal Characterization of Composition, Microstructure, and Mechanical Properties in Tissue Engineering. *Tissue Eng Part B-Re.* 2016;22(4):311-321.

14. Rosteius T, Suero EM, Grasmucke D, *et al*. The sensitivity of ultrasound screening examination in detecting heterotopic ossification following spinal cord injury. *Spinal cord.* 2017;55(1):71-73.

15. Ohlmeier M, Suero EM, Aach M, Meindl R, Schildhauer TA, Citak M. Muscle localization of heterotopic ossification following spinal cord injury. *The spine journal : official journal of the North American Spine Society.* 2017.

16. Stefanidis K, Brindley P, Ramnarine R, *et al*. Bedside Ultrasound to Facilitate Early Diagnosis and Ease of Follow-Up in Neurogenic Heterotopic Ossification: A Pilot Study From the Intensive Care Unit. *The Journal of head trauma rehabilitation.* 2017.

17. Lizzi FL, Feleppa EJ, Alam SK, Deng CX. Ultrasonic spectrum analysis for tissue evaluation. *Pattern Recogn Lett.* 2003;24(4-5):637-658.

18. O'Donnell M, Mimbs JW, Miller JG. Relationship between collagen and ultrasonic backscatter in myocardial tissue. *The Journal of the Acoustical Society of America.* 1981;69(2):580-588.

19. Sethuraman S, Amirian JH, Litovsky SH, Smalling RW, Emelianov SY. Spectroscopic intravascular photoacoustic imaging to differentiate atherosclerotic plaques. *Optics express.* 2008;16(5):3362-3367.

20. Banihashemi B, Vlad R, Debeljevic B, Giles A, Kolios MC, Czarnota GJ. Ultrasound imaging of apoptosis in tumor response: novel preclinical monitoring of photodynamic therapy effects. *Cancer research.* 2008;68(20):8590-8596.

21. Gudur MS, Rao RR, Peterson AW, Caldwell DJ, Stegemann JP, Deng CX. Noninvasive quantification of in vitro osteoblastic differentiation in 3D engineered tissue constructs using spectral ultrasound imaging. *PloS one.* 2014;9(1):e85749.

22. Oelze ML, O'Brien WD, Jr., Blue JP, Zachary JF. Differentiation and characterization of rat mammary fibroadenomas and 4T1 mouse carcinomas using quantitative ultrasound imaging. *IEEE Trans Med Imaging.* 2004;23(6):764-771.

23. Peterson JR, De La Rosa S, Sun H, *et al*. Burn injury enhances bone formation in heterotopic ossification model. *Annals of surgery.* 2014;259(5):993-998.

24. Agarwal S, Loder S, Brownley C, *et al*. Inhibition of Hif1alpha prevents both trauma-induced and genetic heterotopic ossification. *Proceedings of the National Academy of Sciences of the United States of America.* 2016;113(3):E338-347.

25. Balboni TA, Gobezie R, Mamon HJ. Heterotopic ossification: Pathophysiology, clinical features, and the role of radiotherapy for prophylaxis. *International journal of radiation oncology, biology, physics.* 2006;65(5):1289-1299.

26. Falsetti P, Acciai C, Palilla R, Carpinteri F, Patrizio C, Lenzi L. Bedside ultrasound in early diagnosis of neurogenic heterotopic ossification in patients with acquired brain injury. *Clinical neurology and neurosurgery.* 2011;113(1):22-27.

27. Insana MFB, D.G. *Acoustic scattering theory applied to soft biological tissue.* Boca Raton: CRC Press; 1993.

28. Lizzi FL, Greenebaum M, Feleppa EJ, Elbaum M, Coleman DJ. Theoretical framework for spectrum analysis in ultrasonic tissue characterization. *The Journal of the Acoustical Society of America.* 1983;73(4):1366-1373.

29. Lizzi FL, Astor M, Feleppa EJ, Shao M, Kalisz A. Statistical framework for ultrasonic spectral parameter imaging. *Ultrasound in medicine & biology.* 1997;23(9):1371-1382.

30. Lizzi FL, Astor M, Liu T, Deng C, Coleman DJ, Silverman RH. Ultrasonic spectrum analysis for tissue assays and therapy evaluation. *Int J Imag Syst Tech.* 1997;8(1):3-10.

31. Berglund JD, Nerem RM, Sambanis A. Viscoelastic testing methodologies for tissue engineered blood vessels. *Journal of biomechanical engineering.* 2005;127(7):1176-1184.

Chapter 3 Development of Multimode Ultrasound Viscoelastography (MUVE) System

3.1 Introduction

The importance of mechanical cues in the extracellular environment in directing cell behavior has been demonstrated conclusively over the past decade [1-3]. Mechanical signals combine with other cues, including soluble biochemical factors and cell-cell and cell-matrix adhesions, to regulate many important developmental, physiological, and pathological processes [4]. The realization that mechanical factors must be considered when seeking to understand cell function has led to an increasing interest in the field of mechanobiology, with an emphasis on determining how changes in matrix mechanical properties affect cell phenotype. However, the molecular mechanisms underlying mechanotransduction are not fully understood, in part because of the difficulty in robustly characterizing the mechanical behavior of biomaterials at the microscale.

Tissue engineering generally aims to enhance tissue regeneration through the use of cells and biomaterial scaffolds designed to mimic the properties of the extracellular matrix (ECM). It is well established that scaffold materials play a critical role in cell attachment, proliferation, and differentiation, and that their mechanical properties have significant effects on cell behavior [5]. Hydrogels are often used as scaffold materials because of their similarity to the ECM, cell compatibility, and ease of fabrication. These materials consist of water-swollen networks of cross-linked hydrophilic polymer chains derived from either natural, synthetic or hybrid materials [6],

and have been used as biomimetic materials for skin [7], corneal [8, 9], cartilage [10, 11], and vascular [12] tissue engineering. Hydrogels have also been used to study cell-matrix interactions, including response to mechanical cues [13]. A key attribute of many hydrogel biomaterials is their viscoelastic nature [14], which mimics tissue behavior and has recently been shown to be important to the cellular response [15, 16]. Therefore, tuning and characterizing hydrogel mechanical properties are important when creating and maintaining engineered tissues. However, current methods for assessing material mechanical properties are generally limited by the need for invasive specimen preparation, difficulties in applying to soft and cell-seeded biomaterials, and the destructive nature of testing that precludes longitudinal studies.

Commonly used methods for measuring the mechanical properties of hydrogel biomaterials include uniaxial tensile testing [17], compression testing [18], and shear rheology[19, 20]. In addition, more specialized testing using micro- and nano-indentation [21, 22], bulge tests [23], magnetic force methods [24], and other contact-based approaches have been used to characterize the properties of hydrogel materials [25]. These conventional mechanical testing techniques typically deform a sample by stretching or compression applied directly to the sample by means of grips, platens or other physical fixtures [18, 25]. Bulk material properties and stress-strain relationships can be generated to provide more insight into the material behavior, and time-dependent tests can be used to characterize basic viscoelastic properties. However, it is difficult to directly compare measurements obtained from different types of tests because the loading mode is different. For example, shear rheometry relies on tangential shear applied at the material surface (usually in torsion), whereas creep testing uses compression (or tension) to apply a force normal to the surface of the material. The values for the elastic and viscous components derived from these two orthogonal loading modes in soft materials are quite different. In addition, conventional

approaches generally require physical contact with the samples, and are unable to determine internal strain distributions or spatial variation of the mechanical properties in materials.

Ultrasound techniques have the potential for non-invasive material characterization, because of their capability to penetrate and interact with cells and tissues at depth (recently reviewed in [26]. Ultrasound elastography [27] has been developed to detect tumors [28-30] by using ultrasound-generated images before and after tissue compression to derive information about sample stiffness [31, 32]. In particular, acoustic radiation force (ARF) elasticity imaging techniques, such as acoustic radiation force impulse (ARFI) imaging [33, 34], use the force associated with an ultrasound field to generate deformation within a body of material in a non-contact fashion [35, 36]. While ultrasound elastography detects relative spatial variation of tissue stiffness, such as those caused by tumors, it does not generally provide a direct assessment of absolute material parameters or tissue viscoelastic properties.

An ultrasound technique called sonorheometry developed by Walker et al. [37]] for assessing blood coagulation [38, 39] uses multiple ultrasound pulses to apply ARF to a sample, and measures the sample displacement over time. Relative elasticity and viscosity of the sample were derived by fitting the time-displacement curve with a Voigt model. Mauldin at el. [40] used a similar approach called monitored steady-state excitation and recovery (MSSER) to obtain displacement data before and after ARF application. These studies focused on non-invasively determining the relative mechanical properties of inclusions in tissues at depth. However, they worked solely with bulk displacements and did not provide information on microscale mechanical properties. In addition, these ARF-based techniques used the same ultrasound system for both force application and detection of displacement. While convenient, this configuration makes it difficult to generate the high intensity ultrasound pulses needed to generate sufficient ARF for

tissue compression. Therefore, for maximum performance, it is preferable to have separate deforming and imaging beams to optimize the characteristics of each type of ultrasound beam.

The goal of the present study was to demonstrate a versatile technique capable of non-invasive characterization of the viscoelastic properties of hydrogel biomaterials both in the bulk phase and at the microscale. We developed a dual-mode ultrasound elasticity (DUE) technique that uses focused ultrasound (FUS) pulses to induce compression in samples in conjunction with a co-linearly aligned high frequency ultrasound imaging system to detect sample deformation as a function of time and location at high resolution. The use of separate transducers for compression and detection provides the design flexibility to control loading conditions. We applied the DUE technique to representative hydrogel constructs to investigate the effects of biomaterial composition on viscoelastic properties, and to characterize the spatial variation of properties through the depth of these materials. Creep tests were performed by applying a constant load for a defined period of time and characterizing the compression and subsequent relaxation of hydrogel samples. Burger's viscoelastic model was applied to generate quantitative parameters that described the viscoelastic behavior. This study shows how DUE can be used to non-invasively characterize hydrogel materials, and how the spatial variation in mechanical and viscoelastic properties can be mapped using this technique. Such high resolution spatial information is expected to facilitate our elucidation of the principles of mechanobiology, and will aid in designing and developing engineered tissues.

3.2 Materials and Methods

3.2.1 Preparation of hydrogel constructs

Four types of hydrogel constructs were tested: hydroxyapatite (HA)-doped agarose constructs (10.0 mg/ml), HA-doped collagen constructs (2.0 mg/ml and 5.0 mg/ml), HA-doped fibrin constructs (2.0, 4.0, 8.0, 10.0 and 12.0 mg/ml), and cell-seeded collagen constructs (collagen concentration 2.0 mg/ml) on day 1 and day 5. In acellular constructs, hydroxyapatite served as a scatterer that produced ultrasound signals, while in cell-seeded constructs the cellular component served as the scatterer. HA has been used as an additive in a variety of hydrogel biomaterials, for example to potentiate bone formation and to facilitate endothelial network formation [41].

Agarose solution (1.0% w/v) was prepared by dissolving agarose powder (Sigma Aldrich, St. Louis, MO) in distilled water via heating and stirring. Nano-grade hydroxyapatite (HA) (Sigma Aldrich) suspended in Dulbecco's modified Eagle's medium-low glucose (DMEM; Life Technologies, Grand Island, NY) was prepared at 200 mg/ml and placed in a sonication water bath for 1 h to disrupt aggregates [42]. Nano-HA stock solution was added to the agarose solution to obtain a final HA concentration of 10.0 mg/ml. The mixture was degassed and 250 µL was injected into a 48-well plate and allowed to gel at 4°C for 30 min.

HA-doped collagen hydrogels of 2.0 mg/ml and 5.0 mg/ml were generated as previously described [43], with some modifications. Briefly, collagen type I (MP Biomedicals, Solon, OH) was dissolved at 4.0 mg/ml (for 2.0 mg/ml collagen hydrogel) or 10.0 mg/ml (for 5.0 mg/ml collagen hydrogel) in 0.02 N acetic acid and stirred overnight. HA-doped collagen hydrogels were generated by mixing 50% collagen type I, 20% 5X-concentrated Dulbecco's modified Eagle's medium (5X-DMEM; Invitrogen, Carlsbad, CA), 10% fetal bovine serum (FBS; Invitrogen), 5% DMEM, 5% 200 mg/ml nano-HA stock solution, and 10% 0.1 N NaOH (Sigma Aldrich). This

mixture (250 µL) was then injected into a 48-well plate and allowed to gel at 37ºC for 30 min. HA-collagen composites were 10 mm in diameter and 2-3 mm in thickness after fabrication and their dimensions remained stable over time.

HA-doped fibrin hydrogels of 2.0, 4.0, 8.0, 10.0 and 12.0 mg/ml fibrin were prepared by adding nano-HA solution to a fibrin gel mixture as previously described [43]. Fibrinogen was prepared by dissolving the appropriate amount of bovine fibrinogen (Sigma Aldrich) in DMEM to reach the desired final concentration. HA-fibrin hydrogels were generated by mixing 83% fibrinogen stock solution, 10% FBS, 5% of 200 mg/ml nano-HA stock solution, and 2% 50 UT/mL thrombin (Sigma Aldrich). This mixture (250 µL) was injected into a 48-well plate and allowed to gel at 37ºC for 25 min. HA-fibrin composites were 10 mm in diameter and 2-3 mm in thickness after fabrication and their dimensions remained stable over time.

Mouse pre-osteoblast (MC3T3-E1) cells were cultured in α-MEM (Life Technologies) without ascorbic acid but supplemented with 10% FBS and 1% penicillin and streptomycin (PS; Life Technologies), and encapsulated in collagen hydrogels at passage 9 at a concentration of 1.0x106 cells/mL. Cellular constructs were prepared by mixing 50% collagen type I (4.0 mg/ml), 20% 5X-DMEM, 10% FBS, 10% cell suspension in DMEM, and 10% 0.1 N NaOH. This mixture (250 µL) resulted in a collagen concentration of 2.0 mg/ml, which was then injected into a 48-well plate and allowed to gel at 37ºC for 30 min. Cell-seeded constructs were cultured in α-MEM supplemented with FBS and PS for a period of five days. Cellular constructs were ~8 mm in diameter and 2 mm in thickness at day 1, and compacted over time due to cell-mediated compaction to ~5 mm in diameter and 1 mm in thickness at day 5.

3.2.2 MUVE Technique for Characterizing Hydrogel Mechanical Properties

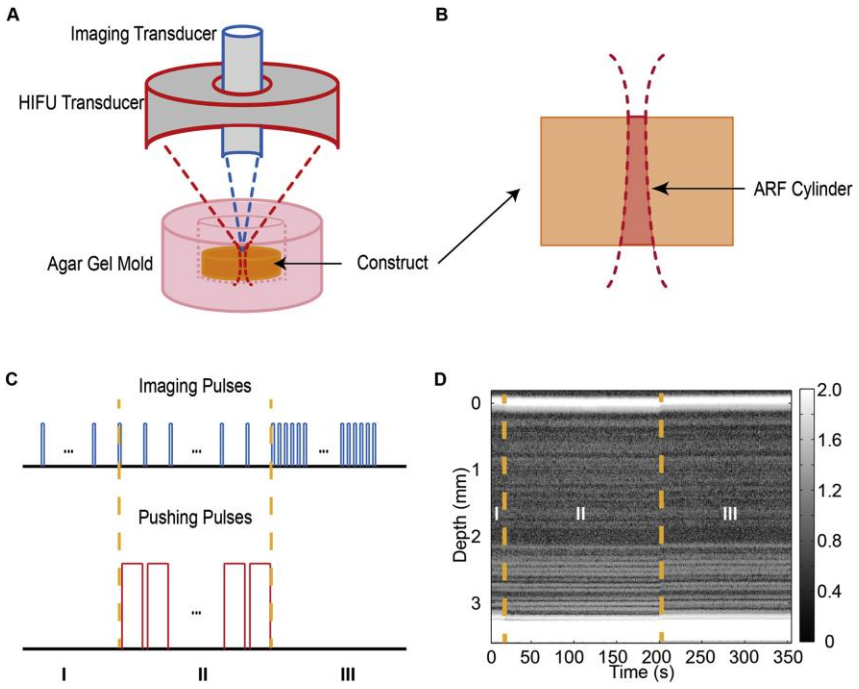

Figure 3-1. (A) Experimental setup of dual mode elastography (DUE), which combines high frequency focused ultrasound (HIFU) with high resolution imaging to mechanically characterize hydrogel materials (not to scale). (B) Cross-section of an acoustic radiation force (ARF) cylinder in a sample caused by focusing of the ultrasound beam. (C) Pulse scheme for FUS pushing and imaging pulses during DUE deformation and detection. (D) Representative grayscale M-mode image showing the scatter distribution before (phase I), during (phase II), and after (phase III) compression.

Experimental Setup – The DUE imaging setup (**Figure 3-1**A) consisted of a 2 MHz FUS transducer with an annular aperture (H148; Sonic Concepts, Woodinville, WA) and an ultrasound imaging system with a 10 MHz transducer (Olympus, Waltham, MA; focal distance at 55 mm, - 6 dB beam width of 1 mm). The imaging transducer was placed in the annular space of the FUS transducer and collinearly aligned. The FUS transducer was driven by a signal generator (33220A; Agilent, Santa Clara, CA) and a power amplifier (75A250; Amplifier Research, Souderton, PA), and was calibrated using a hydrophone (HNR-0500; Onda, Sunnyvale, CA) to map the 3D beam profile in free field. In experiments, a construct was placed in an excavation within a 2% w/v agar gel mold that supported the construct and reduced reflections from boundaries. The FUS focal

point was positioned on the top surface of the construct. In this configuration, the FUS applied an ARF to induce compression within a specific volume determined by the FUS beam profile and referred to as the ARF cylinder, (**Figure 3-1**B).

Ultrasound Application and Data Acquisition – Experiments were conducted using the four types of constructs described above. For each construct, 3D imaging was performed using a VEVO 770 imaging system (VisualSonics Inc., Toronto, Canada) to assess construct morphology and volume. The volume of the construct was determined by integrating the area of cross-sections obtained from 3D image data with 0.2 mm step size using a semi-automated algorithm from the VEVO 770 system. The absorption coefficient and acoustic speed of the constructs were determined from imaging an agar gel pad with and without the construct and comparing the spectral magnitude and travel time to the agar gel pad under both conditions, as described in our previous work [41].

In this study, the DUE technique was tested with ultrasound imaging operated in M-mode at four discrete lateral locations in each construct, although the technique can be easily expanded to fully 3D measurements by performing testing covering the entire construct. At each location, A-line pulse-echo signals were acquired before, during, and after FUS compression and stored for off-line analysis. As illustrated in **Figure 3-1**C, pulse-echo imaging was performed at a 1 Hz pulse repetition frequency (PRF) via a pulser-receiver (5900 PR; Olympus) for 20 s to acquire base-line signals before FUS compression. A series of FUS pulses (1 Hz PRF, pulse duration 0.99 s or duty cycle 99%) were then applied to the construct for a total of 180 s. During FUS application, ultrasound imaging pulses (PRF 1 Hz, pulse duration 0.4 μs or duty cycle 0.00004%) were applied to detect FUS-induced deformation in the construct. The imaging pulses were interleaved with the FUS pulses to allow acquisition of backscattered radio frequency (RF) signals without

interference. At the end of FUS application, imaging was again performed and backscattered RF signals were acquired for 150 s at a PRF of 50 Hz. Synchronization of the FUS pulses and imaging pulses was accomplished using a pulse/delay generator (Model 565; BNC, San Rafael, CA) and two waveform generators (33220A; Agilent, Santa Clara, CA). Backscattered RF signals received by the imaging transducer were recorded at 250 million sample/s and stored on a digital oscilloscope (54380B, Agilent, Santa Clara, CA). **Figure 3-1**D shows an example of an M-mode image generated by the imaging transducer, showing a hydrogel before (section I), during (section II), and after (section III) application of the compressive ultrasound pressure.

Characterization of the FUS transducer was performed to determine the ultrasound beam profile in the sagittal and transverse planes (**Figure 3-2**A and B). The compressive beam measured in free field in this study was axis symmetric, with a 6-dB axial beam depth of 8.0 mm (**Figure 3-2**C) and a lateral beam width of 1.5 mm at the focal plane (**Figure 3-2**D).

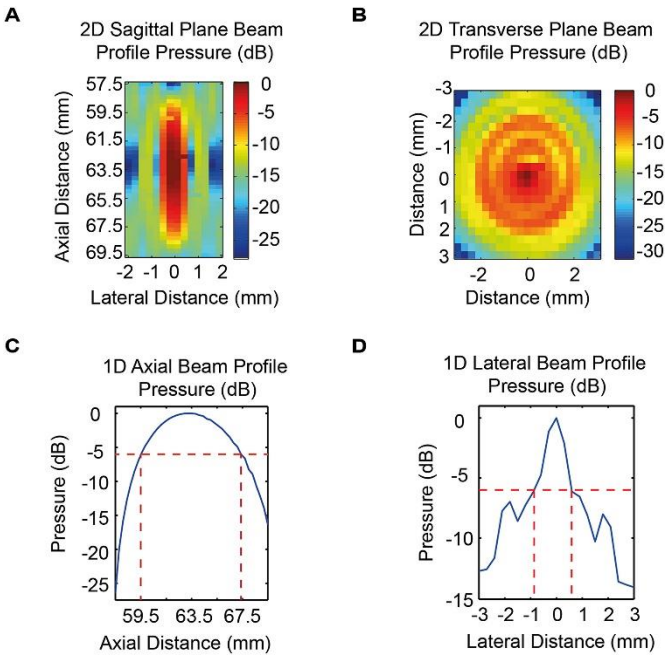

Figure 3-2. Acoustic pressure profile (in dB) for the FUS transducer in (A) 2D sagittal plane, (B) 2D transverse plane, (C) 1D axial direction, and (D) 1D lateral direction.

Generation of Stress and Detection of Strain in Hydrogels using DUE – The principle of DUE is to apply FUS pulses to generate deformation in the construct via the associated ARF, which is caused by momentum transfer from a propagating ultrasound wave to the medium [35]. The ARF is a body force that is generated within a sample [44], offering the possibility of "remote palpation" without direct surface contact. The ARF is dependent on the spatial distribution of the ultrasound intensity and the degree of acoustic attenuation in the sample [45]. A high duty cycle (99%) was chosen for the FUS pulses to generate an essentially constant compression load to the sample, while allowing interleaving with ultrasound imaging for detection of deformation during ARF application.

The lateral beam width of the axial symmetric FUS field (e.g. ~ 1.5 mm) generates deformation mostly concentrated within a narrow cylinder of material along the direction of the FUS beam, which we refer to as the ARF cylinder. The cross sectional area of the ARF cylinder is determined by the lateral energy distribution of the FUS field. The material within the ARF cylinder sustains the most deformation and strain, and the co-linearly aligned high frequency ultrasound imaging system, which also has a narrow lateral beam profile, detects the FUS induced strain within the ARF cylinder as a function of depth and time. Laterally, the detected strain is the average strain over the cross sectional area of the imaging beam.

3.2.3 Data Analysis and Model Fitting

M-mode Image, Local Displacement, and Displacement Color Maps – M-mode images were generated from the series of A-line RF signals obtained at a given location at different times after applying the Hilbert transform to the signals [46] (e.g. **Figure 3-1**D). A section of RF signals in the image represents the material element at that location. For each A-line, displacement at different depths was determined from the temporal shift of the corresponding RF signal segment

from pre-compression using a two-step cross-correlation algorithm [47]. A ten-wavelength window surrounding a specific location was first used to obtain a coarse estimation of displacement at this location. The coarse estimation was then interpolated, and a single wavelength window was applied to obtain the displacement from base-line, defined as the average value of pre-compression locations. Displacement color maps were generated by color-coding the displacement value at each pixel location.

Bulk Strain and Segment Strain – The positions of the top and bottom surfaces of an ARF cylinder in the construct being tested were determined directly from the backscattered RF signals acquired at this location. Change in thickness (Δl) of the ARF cylinder, was calculated as the difference between the displacement at the top surface (d_t) and the bottom surface (d_b) of the ARF cylinder. We define the bulk strain, ε_b, as the ratio of Δl over the original ARF cylinder thickness (l_0) as

$$\varepsilon_b = \frac{d_t - d_b}{l_0} = \frac{\Delta l}{l_0}. \quad (1)$$

To assess spatial distribution of the strain in the construct, an ARF cylinder was divided into *N* axial segments of equal length (l_{s0}) to represent local strains. The segment strain, ε_{s_i}, was defined as the ratio of the change in length of a segment (Δl_i), which is computed as the difference in displacements at the top and bottom boundaries of the segment (d_{t_i} and d_{b_i} in the ARF cylinder) over l_{s0}:

$$\varepsilon_{s_i} = \frac{d_{t_i} - d_{b_i}}{l_{s0}} = \frac{\Delta l_i}{l_{s0}},\ i = 1,2,\ldots,N. \quad (2)$$

Thus the bulk strain is the average of the segment strains:

$$\varepsilon_b = \frac{\Delta l}{l_0} = \frac{\sum_{i=1}^{N} \Delta l_i}{N l_{s0}} = \frac{1}{N} \sum_{i=1}^{N} \frac{\Delta l_i}{l_{s0}} = \frac{1}{N} \sum_{i=1}^{N} \varepsilon_{s_i}. \qquad (3)$$

To relate local strain to bulk strain, the ratio of each segment strain over the bulk strain was computed. The contribution of each segment strain to the overall bulk strain could then be computed to examine heterogeneity within the sample volume, and to determine the effect of segment size on this heterogeneity.

Maximum Strain, Residual Strain, Creep and Recovery Time Constants – The maximum strain was defined as the highest value of strain achieved during FUS application. The residual strain was defined as the steady-state strain after the end of FUS application. The creep and recovery time constants were obtained by fitting the deformation data over time with exponential functions. These parameters provided a versatile means for characterizing the viscoelastic strains without assuming a specific model of the material being tested.

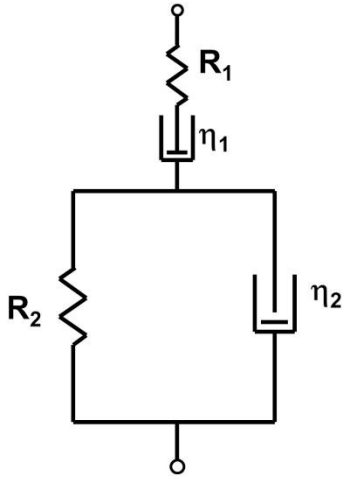

Figure 3-3. Schematic of Burger's model of viscoelastic solids

Burger's Viscoelastic Model – Burger's viscoelastic model [48] (**Figure 3-3**) combines a Maxwell model (a spring and a dashpot in series) and a Voigt model (a spring in parallel with a dashpot). The parameters R_1 and R_2 represent elastic properties (or modulus) of the Maxwell

model and Voigt model respectively, while η_1 and η_2 are associated with the viscosity of the materials [49].

Under a constant stress σ_0 from $t = 0$ to $t = t_c$, the material sustains a strain response described by Burger's model

$$\varepsilon_{creep}(t) = \frac{\sigma_0}{R_1} + \frac{\sigma_0 t}{\eta_1} + \frac{\sigma_0}{R_2}\left[1 - \exp\left(-\frac{R_2}{\eta_2}t\right)\right], \quad (4)$$

which includes the elastic strain σ_0 / R_1, viscous strain $\sigma_0 t / \eta_1$, and viscoelastic strain σ_0 / R_2 with a viscoelastic creep constant η_2 / R_2 [50]. The model parameters R_1, R_2, η_1 and η_2 can be obtained by fitting experimental creep data to equation (4) to characterize the behavior of the viscoelastic material.

After removal of the stress at $t = t_c$, strain will undergo a viscoelastic recovery for $t > t_c$

$$\varepsilon_{recovery}(t) = \frac{\sigma_0 t_c}{\eta_1} + \frac{\sigma_0}{R_2}\left[1 - \exp\left(-\frac{R_2}{\eta_2}t_c\right)\right]\exp\left[-\frac{R_2}{\eta_2}(t - t_c)\right]. \quad (5)$$

Note that equation (5) does not include the instantaneous elastic recovery (σ_0 / R_1) immediately after the removal of the applied stress. Fitting the recovery strain data ($t > t_c$) to equation (5) can be performed to estimate η_1, R_2, and η_2, while R_1 can be obtained directly by determining the instantaneous elastic recovery of strain. However, to avoid potential large errors in estimating the sharp decrease, we rearrange equation (5) using the strain value at $t = t_c$ as

$$\varepsilon_{recovery}(t) = \sigma_0 \frac{t_c}{\eta_1}\left[1 - \exp\left(-\frac{R_2}{\eta_2}(t - t_c)\right)\right] + \left[\varepsilon_{creep}(t_c) - \frac{\sigma_0}{R_1}\right]\exp\left[-\frac{R_2}{\eta_2}(t - t_c)\right], \quad (6)$$

allowing estimation of R_1 by fitting the recovery strain without using the instantaneous recovery strain. Fitting the recovery strain to eq. (6) can be performed to estimate η_1, R_1, and η_2 / R_2.

Model Fitting: DUE Characterization of Averaged Viscoelastic Properties – Burger's viscoelastic model is a lumped model that uses discrete spring and dashpot elements to approximate the behavior of linearly viscoelastic materials. In modeling creep behavior, it assumes that the stress is applied as a step function, and is valid for primary and secondary creep behavior, but not tertiary creep (i.e. necking, which is not relevant in compression). Although theoretically the spatiotemporal evolution of FUS-induced stress and strain in a 3D construct is a distributed problem, the DUE technique is compatible with approximation using Burger's model. Model fitting using Burger's model can be applied to the entire ARF cylinder to obtain averaged material properties, such as the bulk strain as defined in eq. (1) and stress applied to the ARF cylinder. The FUS generated stress for the ARF cylinder is

$$\sigma_0 = \frac{\int_V F dv}{S_{FUS}} = \frac{\int_0^{R_0}\int_0^{l_0} F(r,z')2\pi r dr dz'}{S_{FUS}}. \qquad (7)$$

Thus the averaged viscoelastic property for the ARF cylinder in a construct can be characterized by fitting the strain and stress to eqs. (4) and (5) to obtain the relevant Burger's model parameters.

Because the ARF acts through the sample, the DUE technique can be used to interrogate material properties of a specific segment of material (thickness Δz) at depth z within the sample. The segment strain is related to the stress applied to the segment, calculated by volume integration of the body force ARF within the ARF cylinder:

$$\sigma_0(z) = \frac{\int_V F dv}{S_{FUS}(z)} = \frac{\int_0^{z}\left[\int_0^{R_0} F(r,z')2\pi r dr\right] dz'}{S_{FUS}(z)}, \qquad (8)$$

where $S_{FUS}(z)$ is the beam cross sectional area of the axial symmetric FUS beam at depth z. The ARF, $F[\mathrm{N/m^3}]$ depends on the absorption coefficient $\alpha[\mathrm{m^{-1}}]$, *in situ* acoustic intensity $I'\left[W/m^2\right]$, and speed of sound $c[\mathrm{m/s}]$ in the sample [44]. Under a plane wave assumption,

$$F(r,z)=\frac{2\alpha(r,z)I'(r,z)}{c}=\frac{2\alpha(r,z)I(r,z)e^{-2\alpha(r,z)\cdot z}}{c}, \quad (9)$$

where I' is approximated by the free field intensity $I(r,z)$ multiplied by the attenuation factor.

3.2.4 Temperature Measurement during FUS Application

We used HA-doped collagen constructs (2.0 mg/ml and 5.0 mg/ml collagen) to assess the temperature change due to FUS exposure. A sample was placed in a polymer holder with an acoustically transparent bottom, with its top surface kept dry (above water/medium). IR thermal imaging (Silver SC5600, FLIP, Wilsonville, OR) was used to measure the temperature in the construct as described previously [51] using an emissivity of 0.85 for collagen hydrogels [52]. The FUS pulses were applied from below with its focus positioned on the upper surface of the sample.

3.2.5 Statistical Analysis

Results are presented as mean $\pm$ standard deviation. Student's two-tailed t-test for unpaired samples was performed to determine differences between groups. Differences were considered statistically significant when $p<0.05$.

3.3 Results and Discussion

3.3.1 Ultrasound Characterization of Hydrogel Constructs

A

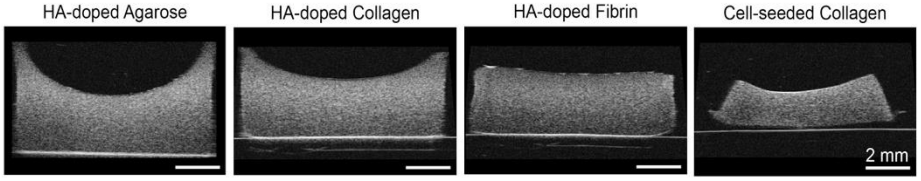

B

Construct Type	Protein Concentration (mg/ml) / Day	Volume (mm^3) (n = 4)	Attenuation Coefficient (dB/MHz/cm)
HA-doped Agarose	10.0	244.6 ± 3.2	0.218 ± 0.025
HA-doped Collagen	2.0	245.1 ± 2.6	0.255 ± 0.033
	5.0	244.6 ± 1.4	0.259 ± 0.017
HA-doped Fibrin	2.0	213.5 ± 14.2	0.245 ± 0.023
	4.0	211.2 ± 6.3	0.250 ± 0.017
	8.0	205.9 ± 7.2	0.241 ± 0.022
	10.0	210.4 ± 13.2	0.259 ± 0.040
	12.0	212.0 ± 3.3	0.255 ± 0.026
Cell-seeded Collagen	2.0 (Day 1)	156.6 ± 17.9	0.153 ± 0.024
	2.0 (Day 5)	36.8 ± 3.0	0.254 ± 0.026

C

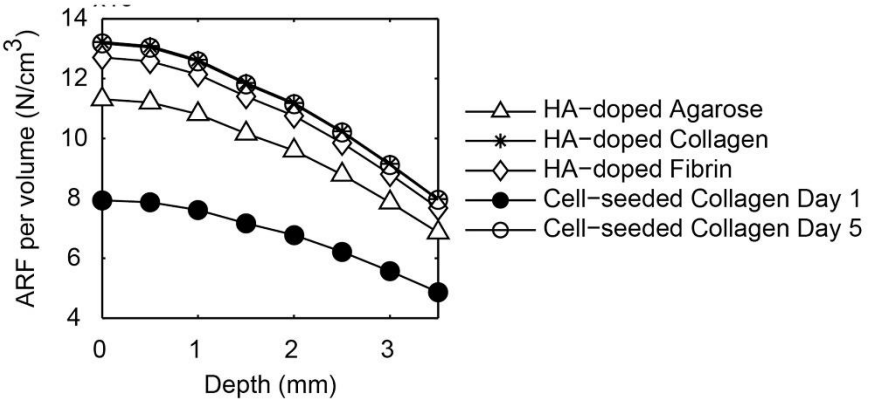

Figure 3-4. (A) B-mode images of hydrogel constructs. (B) Volume and attenuation coefficient of hydrogel constructs as a function of matrix material and concentration. (C) Acoustic radiation force per volume in hydrogel constructs.

Shape and volume changes in the constructs were monitored longitudinally after fabrication using ultrasound imaging. B-mode images of the hydrogel constructs examined in this study (**Figure 3-4**A) showed that the both the HA added to the hydrogels and the cellular component were evenly spatially distributed as acoustic scatterers within the constructs. The table in **Figure 3-4**B shows the calculated volume of each construct type, measured immediately after

fabrication for acellular constructs, and on day 1 and day 5 for cellular constructs. All constructs were fabricated using the same initial volume of material. The agarose gels and collagen constructs had the highest volume, which was similar between the materials. However, fibrin constructs had volumes about 15% lower than the other materials. Cell-seeded constructs exhibited an even larger volume reduction via cell-mediated compaction over time, and decreased in volume by 35% at 1 day and 85% after 5 days. These volume reductions resulted in an effective increase in the protein concentrations in the respective construct types. For example, for 2.0 mg/ml fibrin constructs, the effective bulk concentration after compaction was 2.3 mg/ml. For the more compacted cell-seeded constructs (initial collagen concentration 2.0 mg/ml), the effective collagen concentration was 3.1 mg/ml and 13.2 mg/ml on day 1 and day 5, respectively. An advantage of the non-invasive DUE system is that the dynamic remodeling of constructs can be monitored over time.

Figure 3-4B also lists the acoustic attenuation coefficient of each construct type measured at a location near the middle of the hydrogel. The HA-doped collagen and fibrin constructs exhibited similar degrees of acoustic attenuation, generally around 0.25 dB/MHz/cm. These values were not dependent on protein concentration, suggesting that the HA component was mostly responsible for acoustic attenuation. The day 1 cell-seeded collagen samples exhibited a significantly lower degree of acoustic attenuation due to the lack of HA in the matrix, however by day 5 they were similar to the HA-collagen and HA-fibrin samples. This effect was likely due to the high degree of compaction of the cell-seeded constructs over time, resulting in higher effective cell and matrix densities and greater acoustic scattering. The attenuation coefficients could be used to calculate the axial profile of the ARF associated with the FUS field in each construct tested (**Figure 3-4**C).

The temperature in the constructs was monitored during FUS application (**Figure 3-5**) to characterize the degree of ultrasound-induced heating, which could be harmful to engineered tissues. The temperature was found to follow a time course (**Figure 3-5**A) and spatial pattern (**Figure 3-5**B) that would be expected from FUS energy application and subsequent heat dissipation. Higher acoustic pressure induced a greater temperature rise (**Figure 3-5**C), however the maximum temperature increase was less than 2 ºC for the FUS parameters used in this study. The 5.0 mg/ml collagen constructs exhibited higher temperature increases than the 2.0 mg/ml collagen constructs at the same acoustic pressure, since the FUS-induced temperature increase depends on the attenuation coefficient and thermal diffusivity [33]. However, in all cases the temperature rise was not in the range expected to be harmful to the embedded cellular component.

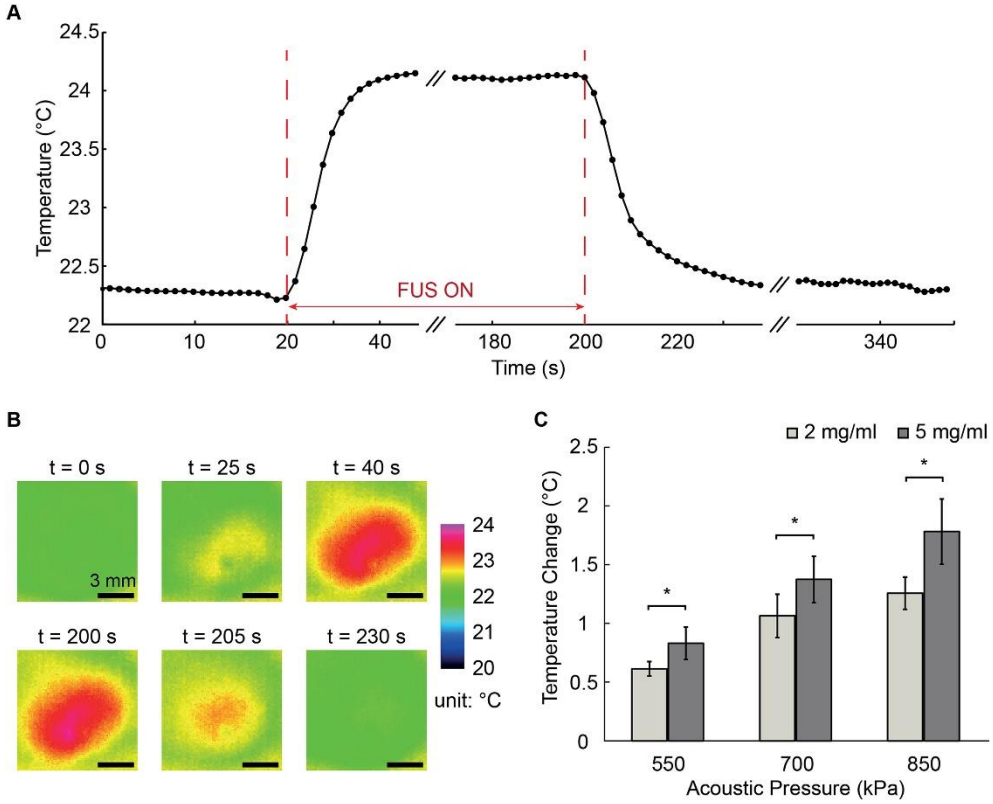

Figure 3-5. (A) Example temperature–time curve of a 5.0 mg/mL HA-doped collagen hydrogel when tested at 850 kPa acoustic pressure. (B) Example of temperature maps at selected time points during creep testing. (C) Aggregate temperature increase data (n = 4) for 2.0 mg/mL and 5.0 mg/mL HA-collagen constructs under acoustic pressure of 550, 700, and 850 kPa with 180 s FUS pulse duration.

3.3.2 FUS-Induced Strain in Hydrogel Constructs

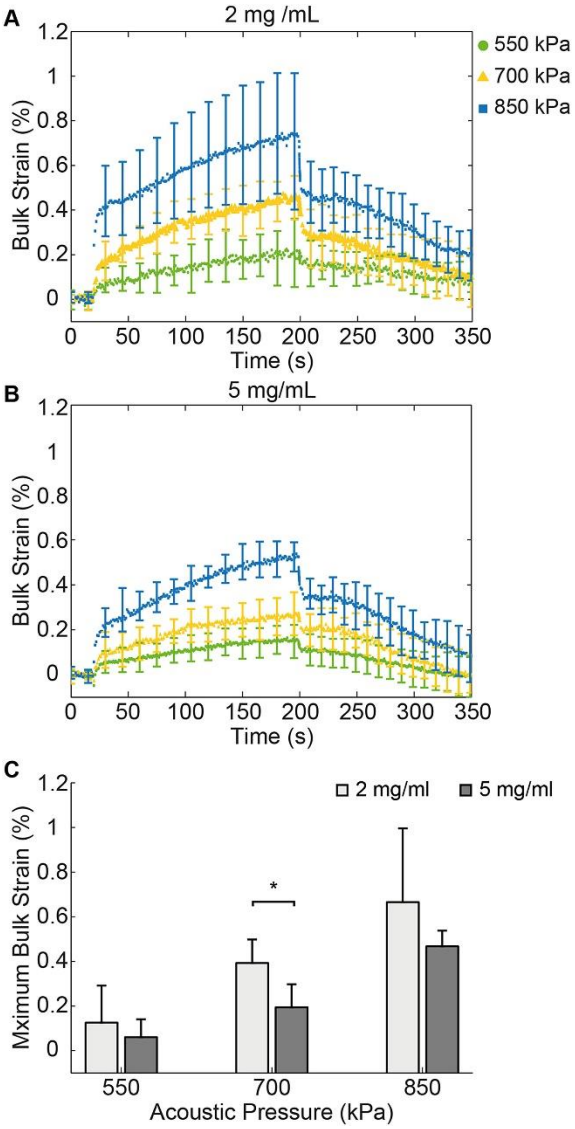

Figure 3-6. Bulk strain curves for (A) 2.0 mg/mL and (B) 5.0 mg/mL HA-doped collagen constructs (n = 4). (C) Maximum bulk strain values for the two concentrations under acoustic pressures of 550 kPa, 700 kPa, and 850 kPa.

Experiments using HA-collagen constructs (2.0 mg/ml or 5.0 mg/ml collagen) were conducted to examine the bulk strain response to FUS application at selected acoustic pressures (**Figure 3-6**). The bulk strain of the constructs exhibited characteristic viscoelastic behavior (**Figure 3-6**A and B). The curves showed a step increase in strain upon FUS application (at t = 20 s) followed by a creep region during which strain increased gradually at constant load until the end

of the 180 s FUS application (t = 200 s), followed by strain recovery when FUS compression was removed. At both collagen concentrations, the different acoustic pressures produced distinct curves. The variation in strain values was somewhat larger in 2.0 mg/ml collagen constructs subjected to higher FUS acoustic pressure, compared to the 5.0 mg/ml constructs. In both types of constructs the maximum strain increased with increasing applied acoustic pressure in an approximately linear fashion (**Figure 3-6**C), and at 700 kPa the collagen concentrations were distinguished by a statistical significantly different maximum strain, reflective of the difference in material stiffness.

3.3.3 Spatiotemporal Distribution of FUS-Induced Deformation in Hydrogel Constructs

Figure 3-7 shows high frequency 3D renderings of the hydrogel construct types (left column), along with the corresponding displacement maps (middle column), and graphs of displacement at four axial locations within each construct type (right column) generated by DUE. The displacement maps express the spatiotemporal evolution of the FUS-induced deformation within the samples. The displacements were the largest at the top surface of the construct, decreased with increasing depth within the material, and were zero at the bottom of the samples because of the fixed boundary. In general, maximum displacements were in the range 10-25 μm, depending on the material and location in the construct. HA-doped agarose gels (**Figure 3-7**A) showed displacements that increased rapidly upon application of FUS, and stayed almost constant during the period of FUS compression. Similarly, recovery after FUS compression was rapid and complete. The rapid step jumps upon application of FUS compression and the lack of significant creep are reflective of the essentially elastic nature of these constructs. In contrast, FUS-generated displacements in collagen and fibrin constructs exhibited viscoelastic behavior, with a clear creep response during FUS compression and after removal of the acoustic pressure (**Figure 3-7**B-D).

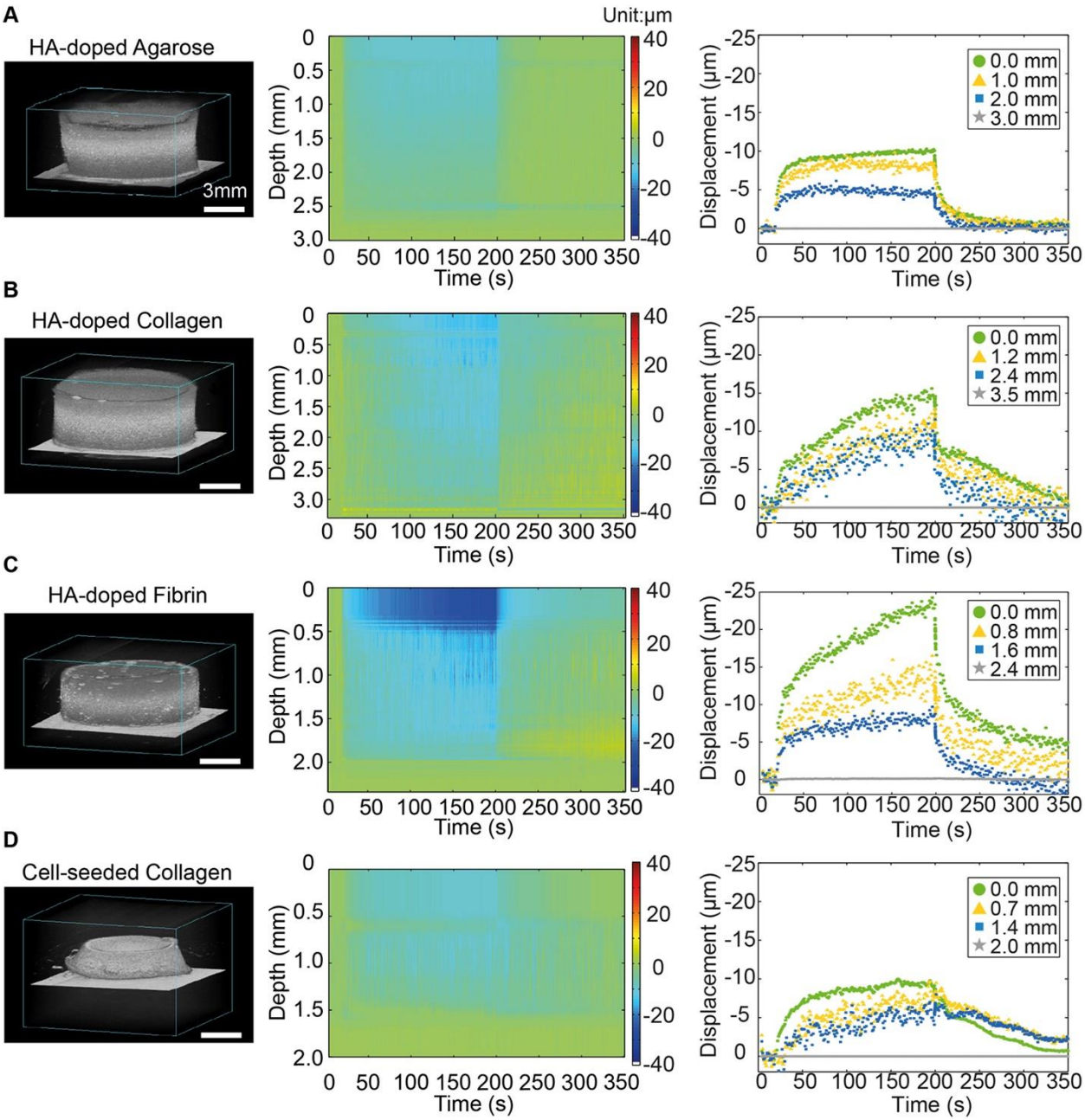

Figure 3-7. Example of 3D rendered ultrasound images (left column), displacement color maps (center column) and displacement at selected depth in the constructs (right column) for (A) HA-doped agarose gel, (B) HA-doped collagen constructs (2.0 mg/mL), (C) HA-doped fibrin construct (2.0 mg/mL), and (D) cell-seeded collagen construct (day 1).

The degree of displacement was dependent on the construct composition. Fibrin constructs generally exhibited the greatest degree of compression, while cell-seeded constructs at day 1

sustained smaller displacements, due to the lower attenuation coefficient (**Figure 3-4**B) and correspondingly lower ARF in these samples (**Figure 3-4**C).

3.3.4 Spatiotemporal Distribution of FUS-Induced Strain in Hydrogel Constructs

The absolute displacement data were converted to strain by normalizing to a dimension in the uncompressed state, either of a portion of the thickness of the construct (to calculate segment strains) or of the entire construct thickness (to calculate bulk strain). **Figure 3-8** shows strain maps (left column), three selected segment strains (middle column), and bulk strains (right column) for the each construct type. The strain maps provide a convenient way to examine the heterogeneity in strain through the thickness of the samples. Strain values produced by FUS compression were generally small (<2%), and the general shape of the curves mirrored the deformation data. HA-doped agarose gels (**Figure 3-8**A) exhibited relatively uniform strain within the sample with complete recovery, consistent with results from other forms of compressive testing [53, 54]. Collagen constructs (**Figure 3-8**B) showed relatively uniform strain levels through the construct, with a characteristic viscoelastic response [55]. Fibrin constructs (**Figure 3-8**C) showed a similar profile, but exhibited significant variation in strain magnitude between segments. Significantly larger strains were observed at the top bottom surfaces of the fibrin constructs, compared to the interior. Cell-seeded collagen constructs (**Figure 3-8**D) produced a profile that showed viscoelastic response, but which was distinct from the acellular constructs. In particular, cell-seeded constructs showed higher spatial variation through their thickness, and a slower relaxation response.

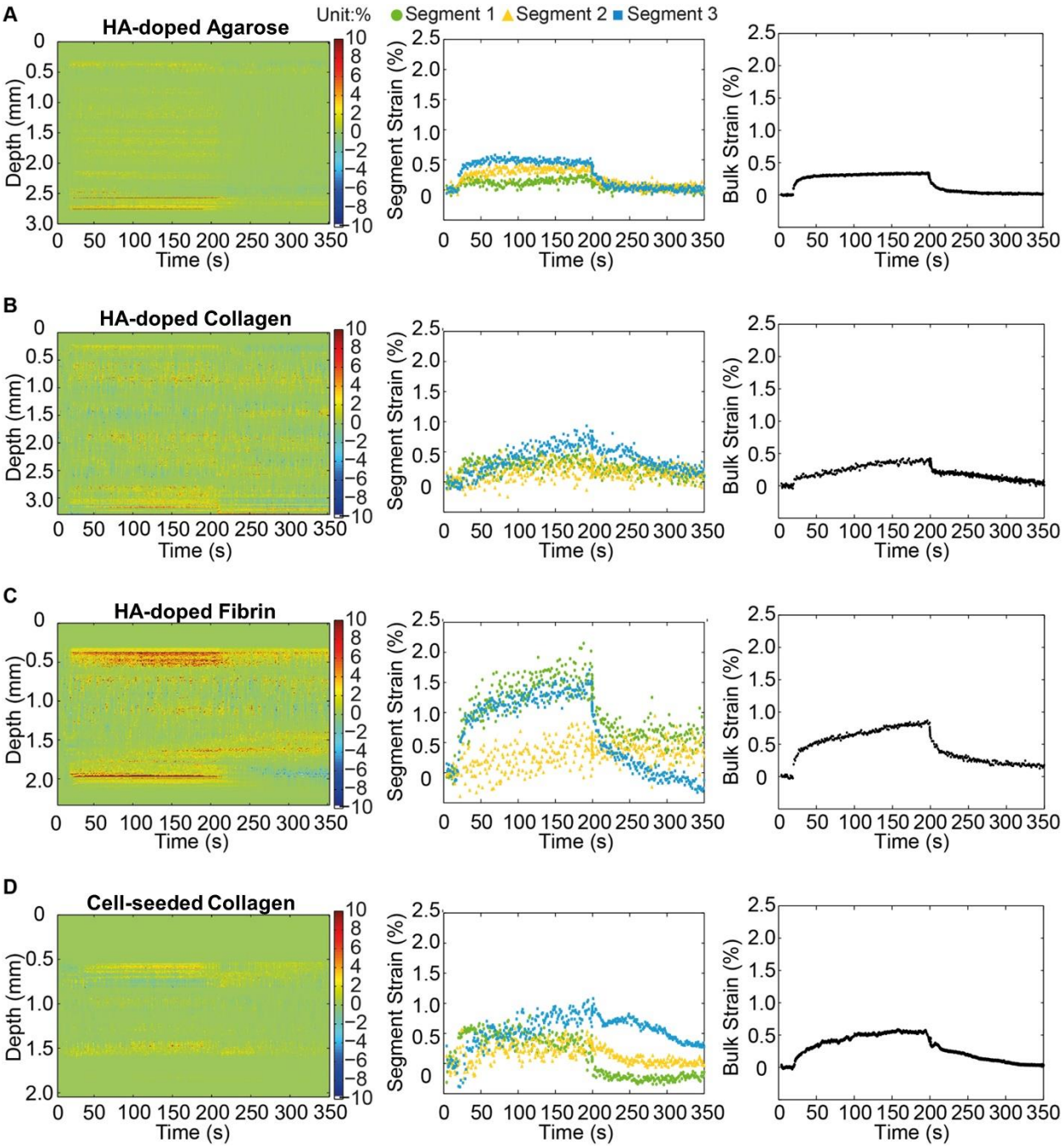

Figure 3-8. Segment strain color maps (left column) and graphs of segment strain (center column) and bulk strain (right column) for (A) HA-doped agarose gel, (B) HA-doped collagen constructs (2.0 mg/mL), (C) HA-doped fibrin construct (2.0 mg/mL), and (D) cell-seeded collagen construct (day 1).

3.3.5 Characteristic Parameters Derived from FUS-Induced Strains in Hydrogel Constructs

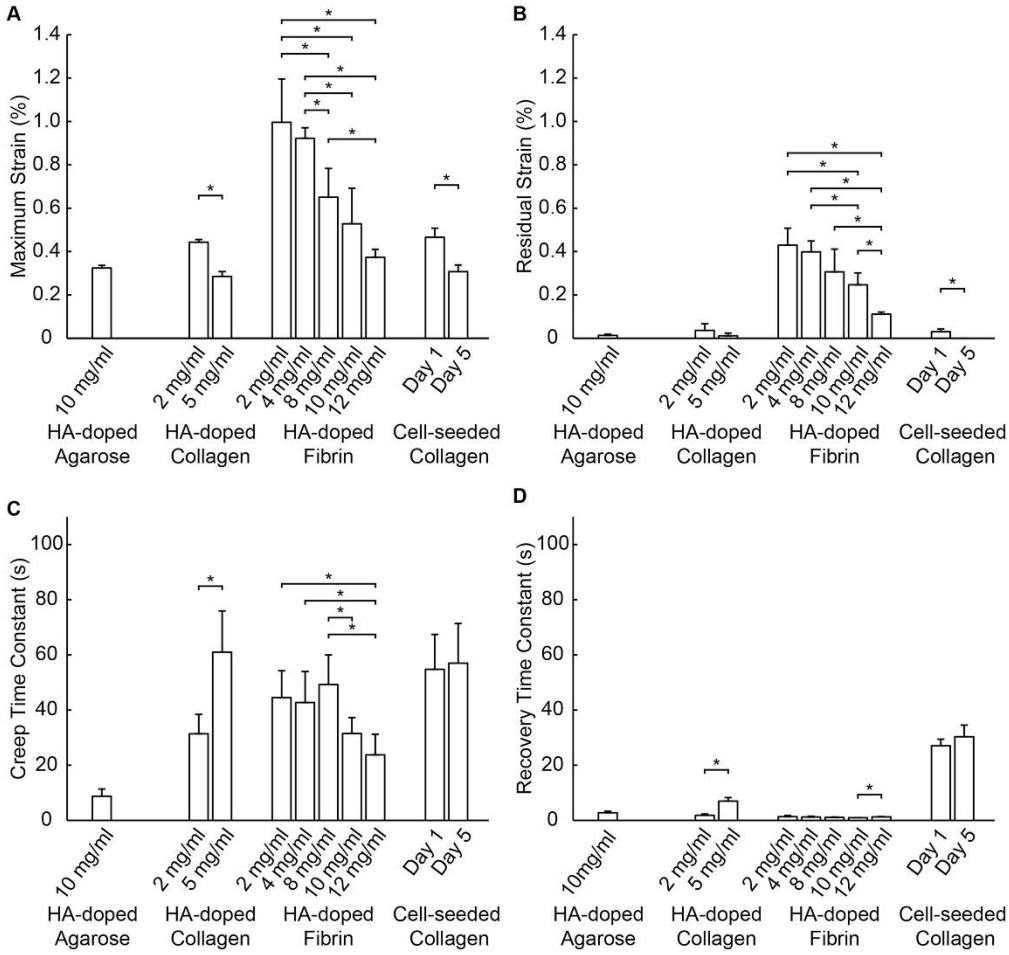

Figure 3-9. Characteristic parameters of hydrogel constructs (n = 4 per construct type). (A) Maximum strain, (B) Residual strain, (C) Creep time constant, and (D) Recovery time constant.

To provide a practical means for rapid quantification of the FUS-induced strain without assuming a model for the material, the maximum strain, residual strain, and creep and recovery time constants were determined from the bulk strain data for each of the samples types (**Figure 3-9**). The maximum strain (**Figure 3-9**A) was both material- and concentration-dependent. At the same concentration, fibrin constructs exhibited significantly higher maximum strains (indicative of lower stiffness) than the other materials. Higher protein concentrations resulted in lower maximum strains (indicative of higher material stiffness), and the effect of concentration was

observable in all materials. The cell-seeded constructs had higher effective collagen concentrations due to volume compaction over time, and consequently the day 5 cellular constructs exhibited a lower maximum strain than the day 1 cellular constructs. These constructs did not contain HA and therefore their increased stiffness is a result of the increased protein and cell concentration caused by hydrogel compaction. The compaction of collagen gels via cell-mediated remodeling is a well-established phenomenon that results in an effectively more concentrated protein matrix [56, 57].

The minimal residual strains detected in the HA-agarose gels and the HA- and cell-seeded collagen constructs (**Figure 3-9**B) indicate that these constructs achieved essentially complete recovery with minimal permanent deformation after the FUS was applied. In contrast, fibrin constructs exhibited comparatively larger residual strains, reflecting the more plastic nature of these constructs that results in more permanent deformation. The degree of residual strain was also dependent on fibrin concentration, with generally decreased residual strain in hydrogels with higher fibrin concentrations. These results are consistent with those obtained from unconfined compression test on synthetic hydrogels with varying water content [14].

The creep and recovery time constants (**Figure 3-9**C and D) represent the dynamics of the deformation and relaxation processes. The more elastic HA-doped agarose gels exhibited low creep and recovery time constants, indicating a more rapid material response. HA-collagen and HA-fibrin materials showed markedly higher creep time constants. While higher collagen concentration increased the time constants, there was no clear protein concentration-dependence in the HA-fibrin constructs. The cell-seeded collagen constructs exhibited notably higher creep and relaxation time constants, reflective of the slower dynamics of deformation and relaxation in these constructs. In particular, the cellular constructs became stiffer and had altered time-depended

deformation as they developed from day 1 to day 5, similar to reported results from *in vivo* studies [58, 59].

3.3.6 Viscoelastic Properties of Hydrogel Constructs using Model Fitting

To assess the averaged properties of constructs within an ARF cylinder, we fit the measured bulk strain data using Burger's model to obtain the elastic and viscoelastic parameters for each of the constructs types (**Figure 3-10**). The spring constant for the Maxwell element, R_1, represents the initial elastic response of the material, and is directly related to material stiffness. The R_1 values (**Figure 3-10**A) agreed in general with the trends observed in the maximum strain data (**Figure 3-9**A), though they showed an inverse pattern since increased stiffness leads to decreased strain. Collagen at 5.0 mg/ml was stiffer than at 2.0 mg/ml, and cellular constructs were stiffer at day 5 then at day 1. There was again a general increase in stiffness with increasing protein concentration in both collagen and fibrin constructs, consistent with reported observations that hydrogels with lower water content or higher protein concentration exhibit higher stiffness [58, 60].

The viscous damping parameter in the Maxwell element, η_1 (**Figure 3-10**B), represents the unrecoverable strain response and the long term creep behavior of the material. This value was lowest in fibrin constructs, indicating an increased propensity to creep over time, and exhibited a concentration dependence. The agarose constructs exhibited a relatively large η_1, reflecting their more elastic nature. This parameter was markedly elevated in the day 5 cellular constructs, suggesting decreased viscoelastic behavior, presumably due to the large increase in collagen protein concentration due to volume compaction and other changes during construct development.

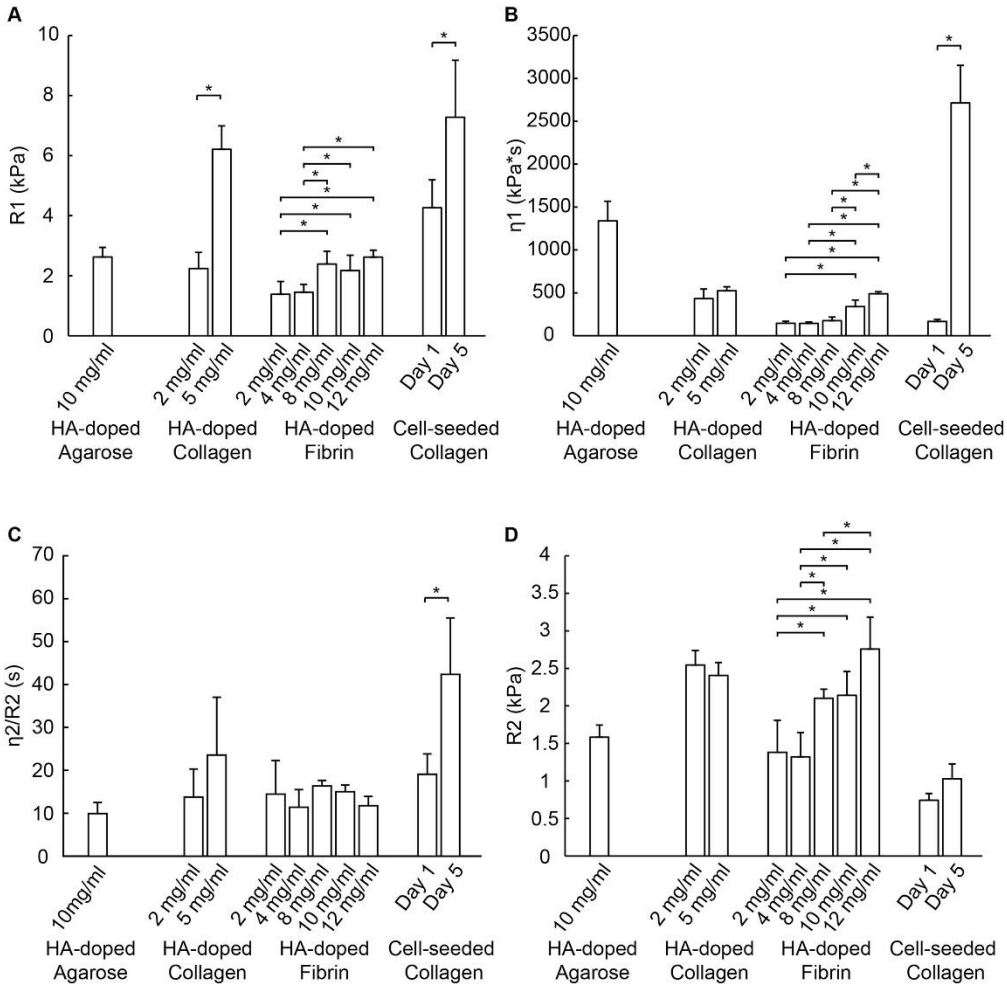

Figure 3-10. Burger's model parameters for hydrogel constructs generated by fitting of the bulk creep curves (n = 4 per construct type). (A) R1, (B) η1, (C) η2/R2, and (D) R2.

The viscoelastic time constant, η_2 / R_2 (**Figure 3-10**C) reflects the magnitude and duration of the transient region of the creep curve. This parameter was similar among the acellular constructs tested, though the Day 5 cellular collagen constructs exhibited an increase relative to other constructs. This parameter reflects a slower creep response, and again suggests a significant effect of construct development on the viscoelastic behavior of cellular constructs. The cellular constructs also had a lower value of the modulus related to retarded elasticity, R_2 (**Figure 3-10**D), which is inversely related to the magnitude of the strain response in the transient region.

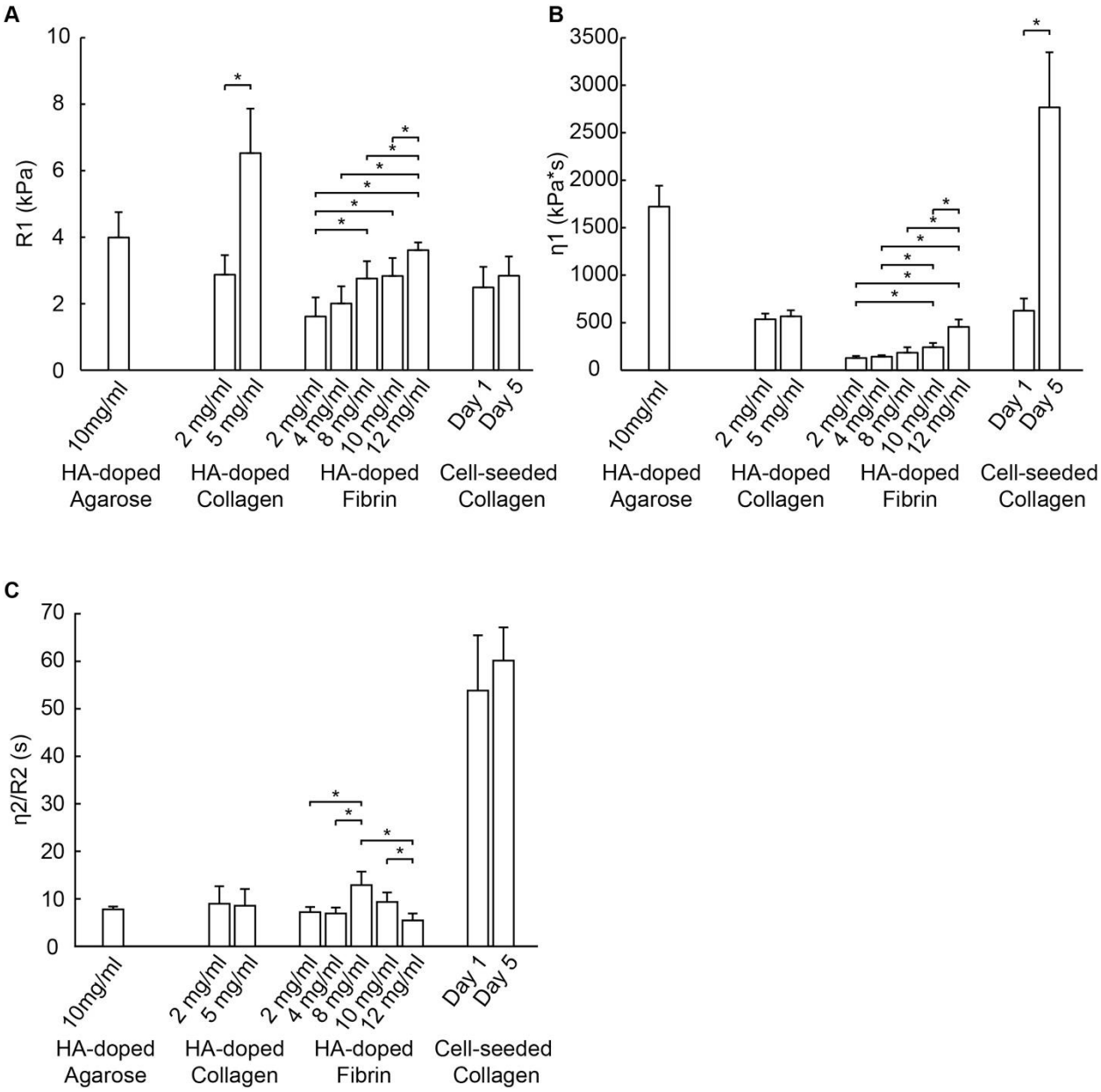

Figure 3-11. Burger's model parameters for hydrogel constructs generated by fitting of the bulk recovery curves (n = 4 per construct type). (A) R1, (B) η1, and (C) η2/R2.

The Burger's parameters generated for different types of constructs reflected the different viscoelastic characteristics of the materials and, in the case of cellular constructs, their development over time. These parameters reveal the effects of construct composition (type and concentration of protein, presence of cells, changes over time) on their mechanical properties and behavior, and therefore provide a useful tool in comparing materials and developing constructs.

Notably, these parameters can be obtained non-invasively and at high resolution using DUE. The Burger's model parameters obtained from the relaxation portion of the creep curve were also calculated (**Figure 3-11**), and generally mirrored the values obtained from the creep deformation curve. Mechanical parameters obtained using DUE can also be combined with compositional information, for example as obtained by multispectral ultrasound imaging [41, 45], to elucidate structure-function relationships in engineered tissues.

An important capability of the DUE technique is the ability to virtually section samples and thereby to examine local mechanical properties at a very small scale non-invasively. This type of analysis can also reveal inhomogeneity in samples at high resolution. The displacement and strain maps and curves presented in **Figure 3-7** and **Figure 3-8** show spatial variation along the depth direction, and provide a rapid and easily accessible way to show the pattern of internal strains. The amount of variability between segments at different depths depended on the construct type and could be generally represented by the ratio of the segment strain to the bulk strain. **Figure 3-12** shows an analysis of segment strains and the fraction of the total bulk strain which each segment contributes. These data show that there is heterogeneity in strain through the construct, and that the amount of variation depended on the construct type. Agarose gels exhibited more uniform strain that increased regularly through the thickness of the sample as would be the expected effect of a body force, compared to the collagen and fibrin constructs, which exhibited more random variations. In addition, the degree of variation depended on the number of segments used in the analysis. Use of three segments (**Figure 3-12**A) resulted in relatively uniform segment strains, while use of six segments (**Figure 3-12**B) revealed increased heterogeneity at smaller scales.

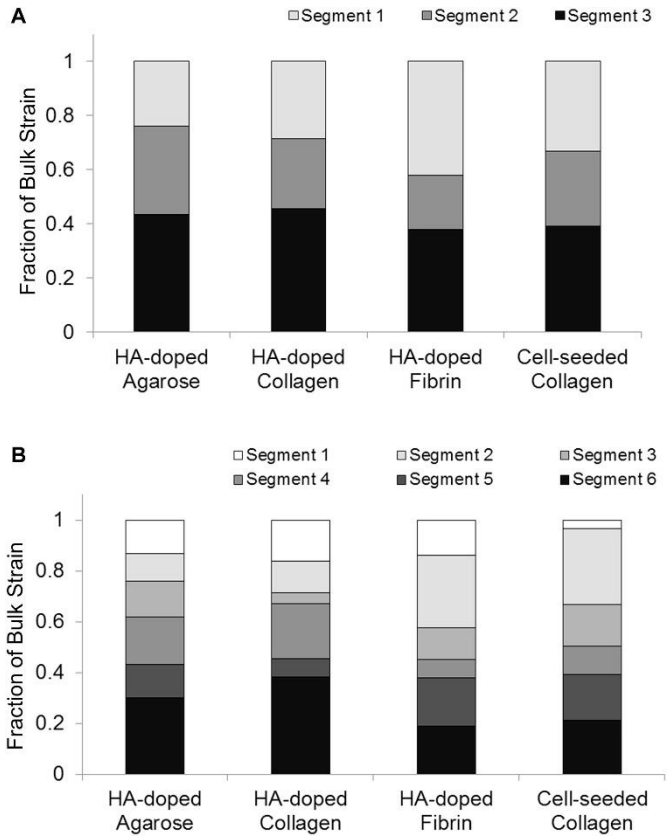

Figure 3-12. Fraction of the total bulk strain contributed by each segment, when analyzed as A) three segments, or B) six segments.

The ability to analyze sub-surface sections of the material non-invasively is a useful feature when characterizing the structure of a biomaterials and its mechanical effect on cells. Previously reported efforts have used conventional shear rheometry to measure the viscoelastic properties of collagen gels fabricated under different temperatures [61]. The bulk shear properties were correlated with the microscale morphology of the collagen fibers as determined by confocal microscopy, but no direct microscale mechanical measurements were made. Another previous study applied "active microrheology" by optically oscillating silica microbeads (2 μm in diameter) within a fibrin matrix [62]. The oscillatory deflection of the surrounding matrix was used to determine the storage and loss moduli of the material, similar to macroscale dynamic mechanical analysis. However, the degree of microbead deflection was only around 60 nm, and therefore the

technique may be better described as “nanorheology”. In contrast, the DUE technique we report achieved and imaged deformation from 5,000-25,000 nm (5-25 μm), which is more clearly on the microscale. In agreement with the present study, the active microrheology experiments showed that protein hydrogels exhibit microscale heterogeneity.

3.4 Conclusion

This study demonstrates the feasibility of applying DUE to the non-invasive characterization of both the averaged bulk and segmented local viscoelastic properties of hydrogel constructs. Application of a constant acoustic radiation force using DUE can be used to perform a creep test on small or large samples, and the resulting curves reflect the viscoelastic characteristics of the materials. In addition, DUE can be used to image the samples and determine their volume, morphology, and acoustic parameters. Testing of HA-doped hydrogels showed the effects of material type and concentration on the viscoelastic mechanical properties, as well as the effects of cell-seeding as constructs developed over time. Importantly, examination of local mechanical properties showed spatial variation that reflected microscale heterogeneity within the constructs. These findings suggest that DUE is a flexible tool that can be used to investigate microscale properties of hydrogel materials over time. The technique may also be extended to examine other material properties, and to characterization of tissues *in vivo*. Therefore DUE may provide an important enabling tool for investigating fundamental mechanisms of mechanobiology and facilitating progress in tissue engineering.

3.5 References

1. Discher, D.E., P. Janmey, and Y.L. Wang, *Tissue cells feel and respond to the stiffness of their substrate.* Science, 2005. **310**(5751): p. 1139-43.

2. Jaalouk, D.E. and J. Lammerding, *Mechanotransduction gone awry.* Nat Rev Mol Cell Biol, 2009. **10**(1): p. 63-73.

3. Vogel, V. and M. Sheetz, *Local force and geometry sensing regulate cell functions.* Nat Rev Mol Cell Biol, 2006. **7**(4): p. 265-75.

4. Discher, D.E., D.J. Mooney, and P.W. Zandstra, *Growth factors, matrices, and forces combine and control stem cells.* Science, 2009. **324**(5935): p. 1673-7.

5. Drury, J.L. and D.J. Mooney, Hydrogels for tissue engineering: scaffold design variables and applications. Biomaterials, 2003. **24**(24): p. 4337-4351.

6. Anseth, K.S., C.N. Bowman, and L. Brannon-Peppas, *Mechanical properties of hydrogels and their experimental determination.* Biomaterials, 1996. **17**(17): p. 1647-57.

7. Eaglstein, W.H. and V. Falanga, *Tissue engineering and the development of Apligraf(R), a human skin equivalent.* Clinical Therapeutics, 1997. **19**(5): p. 894-905.

8. Minami, Y., H. Sugihara, and S. Oono, *Reconstruction of Cornea in 3-Dimensional Collagen Gel Matrix Culture.* Investigative Ophthalmology & Visual Science, 1993. **34**(7): p. 2316-2324.

9. Vijayasekaran, S., et al., *Cell viability and inflammatory response in hydrogel sponges implanted in the rabbit cornea.* Biomaterials, 1998. **19**(24): p. 2255-2267.

10. Kisiday, J., et al., *Self-assembling peptide hydrogel fosters chondrocyte extracellular matrix production and cell division: Implications for cartilage tissue repair.* Proceedings of the National Academy of Sciences of the United States of America, 2002. **99**(15): p. 9996-10001.

11. Yamaoka, H., et al., *Cartilage tissue engineering chondrocytes embedded in using human auricular different hydrogel materials.* Journal of Biomedical Materials Research Part A, 2006. **78A**(1): p. 1-11.

12. Weinberg, C.B. and E. Bell, *A Blood-Vessel Model Constructed from Collagen and Cultured Vascular Cells.* Science, 1986. **231**(4736): p. 397-400.

13. Chaudhuri, O., et al., *Hydrogels with tunable stress relaxation regulate stem cell fate and activity.* Nat Mater, 2015.

14. Stammen, J.A., et al., *Mechanical properties of a novel PVA hydrogel in shear and unconfined compression.* Biomaterials, 2001. **22**(8): p. 799-806.

15. Chaudhuri, O., et al., *Substrate stress relaxation regulates cell spreading.* Nat Commun, 2015. **6**: p. 6364.

16. Ahearne, M., et al., *Characterizing the viscoelastic properties of thin hydrogel-based constructs for tissue engineering applications.* Journal of the Royal Society Interface, 2005. **2**(5): p. 455-463.

17. Rowe, S.L., S. Lee, and J.P. Stegemann, *Influence of thrombin concentration on the mechanical and morphological properties of cell-seeded fibrin hydrogels.* Acta Biomater, 2007. **3**(1): p. 59-67.

18. Svensson, A., et al., *Bacterial cellulose as a potential scaffold for tissue engineering of cartilage.* Biomaterials, 2005. **26**(4): p. 419-431.

19. Ulrich, T.A., et al., *Probing cellular mechanobiology in three-dimensional culture with collagen-agarose matrices.* Biomaterials, 2010. **31**(7): p. 1875-84.

20. Rao, R.R., et al., *Matrix composition regulates three-dimensional network formation by endothelial cells and mesenchymal stem cells in collagen/fibrin materials.* Angiogenesis, 2012. **15**(2): p. 253-264.

21. Merino, J.C., B. Martin, and J.M. Pastor, *Mechanical Indentation Tester Designed to Control and Measure in Real-Time the Microhardness Process.* Measurement Science & Technology, 1991. **2**(8): p. 740-743.

22. Mirshams, R.A. and R.M. Pothapragada, *Correlation of nanoindentation measurements of nickel made using geometrically different indenter tips.* Acta Materialia, 2006. **54**(4): p. 1123-1134.

23. Tsakalakos, T., *The Bulge Test - a Comparison of Theory and Experiment for Isotropic and Anisotropic Films.* Thin Solid Films, 1981. **75**(3): p. 293-305.

24. Liu, K.K. and B.F. Ju, *A novel technique for mechanical characterization of thin elastomeric membrane.* Journal of Physics D-Applied Physics, 2001. **34**(15): p. L91-L94.

25. Drury, J.L., R.G. Dennis, and D.J. Mooney, *The tensile properties of alginate hydrogels.* Biomaterials, 2004. **25**(16): p. 3187-3199.

26. Deng, C.X., X. Hong, and J.P. Stegemann, *Ultrasound imaging techniques for spatiotemporal characterization of composition, microstructure, and mechanical properties in tissue engineering.* Tissue Eng Part B Rev, 2016.

27. Ophir, J., et al., *Elastography - a Quantitative Method for Imaging the Elasticity of Biological Tissues.* Ultrasonic Imaging, 1991. **13**(2): p. 111-134.

28. Garra, B.S., et al., *Elastography of breast lesions: Initial clinical results.* Radiology, 1997. **202**(1): p. 79-86.

29. Hoeks, A.P.G., et al., *Non-invasive measurement of mechanical properties of arteries in health and disease.* Proceedings of the Institution of Mechanical Engineers Part H-Journal of Engineering in Medicine, 1999. **213**(H3): p. 195-202.

30. Levinson, S.F., M. Shinagawa, and T. Sato, *Sonoelastic Determination of Human Skeletal-Muscle Elasticity.* Journal of Biomechanics, 1995. **28**(10): p. 1145-1154.

31. Lubinski, M.A., S.Y. Emelianov, and M. O'Donnell, *Speckle tracking methods for ultrasonic elasticity imaging using short-time correlation.* IEEE Trans Ultrason Ferroelectr Freq Control, 1999. **46**(1): p. 82-96.

32. Bilgen, M. and M.F. Insana, *Deformation models and correlation analysis in elastography.* J Acoust Soc Am, 1996. **99**(5): p. 3212-24.

33. Nightingale, K., et al., *Acoustic radiation force impulse imaging: In vivo demonstration of clinical feasibility.* Ultrasound in Medicine and Biology, 2002. **28**(2): p. 227-235.

34. Nightingale, K.R., et al., *On the feasibility of remote palpation using acoustic radiation force.* J Acoust Soc Am, 2001. **110**(1): p. 625-34.

35. Doherty, J.R., et al., *Acoustic radiation force elasticity imaging in diagnostic ultrasound.* IEEE Trans Ultrason Ferroelectr Freq Control, 2013. **60**(4): p. 685-701.

36. Lizzi, F.L., et al., *Radiation-force technique to monitor lesions during ultrasonic therapy.* Ultrasound Med Biol, 2003. **29**(11): p. 1593-605.

37. Walker, W.F., F.J. Fernandez, and L.A. Negron, *A method of imaging viscoelastic parameters with acoustic radiation force.* Phys Med Biol, 2000. **45**(6): p. 1437-47.

38. Viola, F., et al., *A novel ultrasound-based method to evaluate hemostatic function of whole blood.* Clin Chim Acta, 2010. **411**(1-2): p. 106-13.

39. Viola, F., et al., *Sonorheometry: a noncontact method for the dynamic assessment of thrombosis.* Ann Biomed Eng, 2004. **32**(5): p. 696-705.

40. Mauldin, F.W., Jr., et al., *Monitored steady-state excitation and recovery (MSSER) radiation force imaging using viscoelastic models.* IEEE Trans Ultrason Ferroelectr Freq Control, 2008. **55**(7): p. 1597-610.

41. Rao, R.R., et al., *Effects of hydroxyapatite on endothelial network formation in collagen/fibrin composite hydrogels in vitro and in vivo.* Acta Biomater, 2014. **10**(7): p. 3091-7.

42. Gudur, M.S., et al., *Noninvasive quantification of in vitro osteoblastic differentiation in 3D engineered tissue constructs using spectral ultrasound imaging.* PLoS One, 2014. **9**(1): p. e85749.

43. Cummings, C.L., et al., *Properties of engineered vascular constructs made from collagen, fibrin, and collagen-fibrin mixtures.* Biomaterials, 2004. **25**(17): p. 3699-706.

44. Nyborg, W., *Acoustic Streaming*, in *Physical Streaming*, W. Mason, Editor. 1965, Academic: New York. p. 265-331.

45. Torr, G.R., *The Acoustic Radiation Force.* American Journal of Physics, 1984. **52**(5): p. 402-408.

46. Gudur, M., et al., *Noninvasive, quantitative, spatiotemporal characterization of mineralization in three-dimensional collagen hydrogels using high-resolution spectral ultrasound imaging.* Tissue Eng Part C Methods, 2012. **18**(12): p. 935-46.

47. Chen, H., H. Shi, and T. Varghese, *Improvement of elastographic displacement estimation using a two-step cross-correlation method.* Ultrasound Med Biol, 2007. **33**(1): p. 48-56.

48. Berglund, J.D., R.M. Nerem, and A. Sambanis, *Viscoelastic testing methodologies for tissue engineered blood vessels.* J Biomech Eng, 2005. **127**(7): p. 1176-84.

49. Rowe, S.L. and J.P. Stegemann, *Microstructure and mechanics of collagen-fibrin matrices polymerized using ancrod snake venom enzyme.* J Biomech Eng, 2009. **131**(6): p. 061012.

50. Dey, A.B., P.K., *Parameter estimation of four-parameter viscoelastic Burger model by inverse analysis: case studies of four oil-refineries.* Interaction and Multiscale Mechanics, 2012. **5**(3): p. 211-228.

51. Hsiao, Y.S., R.E. Kumon, and C.X. Deng, *Characterization of Lesion Formation and Bubble Activities during High Intensity Focused Ultrasound Ablation using Temperature-Derived Parameters.* Infrared Phys Technol, 2013. **60**: p. 108-117.

52. Ye, X.Y., et al., *Structure and infrared emissivity of collagen/SiO2 composite.* Applied Surface Science, 2008. **254**(18): p. 5975-5980.

53. Ahearne, M., et al., *Characterizing the viscoelastic properties of thin hydrogel-based constructs for tissue engineering applications.* J R Soc Interface, 2005. **2**(5): p. 455-63.

54. Normand, V., et al., *New insight into agarose gel mechanical properties.* Biomacromolecules, 2000. **1**(4): p. 730-738.

55. Chandran, P.L. and V.H. Barocas, *Microstructural mechanics of collagen gels in confined compression: Poroelasticity, viscoelasticity, and collapse.* Journal of Biomechanical Engineering-Transactions of the Asme, 2004. **126**(2): p. 152-166.

56. Hong, H., C.M. McCullough, and J.P. Stegemann, *The role of ERK signaling in protein hydrogel remodeling by vascular smooth muscle cells.* Biomaterials, 2007. **28**(26): p. 3824-33.

57. Mohammadi, H., P.A. Janmey, and C.A. McCulloch, *Lateral boundary mechanosensing by adherent cells in a collagen gel system.* Biomaterials, 2014. **35**(4): p. 1138-49.

58. Bryant, S.J. and K.S. Anseth, *Hydrogel properties influence ECM production by chondrocytes photoencapsulated in poly(ethylene glycol) hydrogels.* J Biomed Mater Res, 2002. **59**(1): p. 63-72.

59. Weinand, C., et al., *Comparison of hydrogels in the in vivo formation of tissue-engineered bone using mesenchymal stem cells and beta-tricalcium phosphate.* Tissue Eng, 2007. **13**(4): p. 757-65.

60. Hunter, C.J., J.K. Mouw, and M.E. Levenston, *Dynamic compression of chondrocyte-seeded fibrin gels: effects on matrix accumulation and mechanical stiffness.* Osteoarthritis Cartilage, 2004. **12**(2): p. 117-30.

61. Kotlarchyk, M.A., et al., *Concentration independent modulation of local micromechanics in a fibrin gel.* PLoS One, 2011. **6**(5): p. e20201.

62. Raub, C.B., et al., *Noninvasive assessment of collagen gel microstructure and mechanics using multiphoton microscopy.* Biophys J, 2007. **92**(6): p. 2212-22

Chapter 4 Interrogation of Viscoelastic Properties in Heterogeneous Biomaterials

4.1 Introduction

The importance of mechanical factors in regulating cell and tissue function is clear. However, the ability to meaningfully leverage the principles of mechanobiology requires more and better information about the structure and function of the cellular microenvironment. Cells sense and respond to their mechanical environment through receptors and signaling pathways that coordinate such functions as differentiation, proliferation, migration, and matrix remodeling [1]. Mechanical behavior must therefore be considered when developing biomaterials to guide cell function, either as platforms to study cellular processes or as components of restorative therapies. Importantly, the fields of cell-matrix interactions and cellular mechanobiology have evolved over the past decade [2-4], from a focus on the passive mechanical properties of the extracellular environment to a growing realization that the dynamic and complex nature of extracellular mechanics must be considered. In particular, recent work has demonstrated that nonlinear elastic [5-7] and viscoelastic [8-10] behaviors of the extracellular matrix affect cells in ways that transcend the simple elastic response.

While the impact of both passive and dynamic mechanical signals on cell behavior is undisputed, our understanding of mechanobiology is hampered by a lack of information about the local physical properties of the cellular microenvironment on length scales that cells sense [11, 12]. Native tissues are composed of cells surrounded by a network of fibrillar glycoproteins and hydrated proteoglycans. This composite structure gives rise to scale-dependent heterogeneity as well as complex mechanical properties and behaviors. A variety of biomaterial systems have been

developed to mimic key aspects of the structure of native extracellular matrix, including hydrogels composed of natural proteins [13-15], polysaccharide matrices [16] and synthetic polymers [17]. Such materials are used widely in studying cellular mechanobiology. However, the mechanical properties of heterogeneous materials can depend on the resolution at which they are examined, such that microscale structure-function relationships can be distinct from the macroscale mechanical properties. In addition, the high water content and combination of solid and fluid elements in these materials results in time-dependent and viscoelastic behavior.

A variety of methods have been applied to measure mechanical properties of native tissues and hydrogel biomaterials. However, microscale testing of soft materials with high water content can be challenging. Most studies have used conventional, macroscale techniques such as tensile [18, 19] and compressive testing [20, 21], or shear rheology [22-24], which cannot discriminate microscale heterogeneity in materials, nor can they provide insight into interior architectures. A much smaller number of studies have probed microscale properties. For example, atomic force microscopy and nanoindentation have been applied to mature bone but only sparingly to tissues and hydrogel materials [25-27]. However, these techniques suffer from high variability and provide only two-dimensional (2D) surface maps of material properties. Optical trapping of particles embedded in hydrogel matrices has been used for oscillatory dynamic mechanical analysis [28], but provides deformations only on the nanoscale and is only feasible for small, thin samples. Notably, all of these techniques require physical contact or manipulation of the samples, which hinders longitudinal assessment of developing tissues.

Here we demonstrate a novel ultrasound-based approach that can noninvasively characterize the complex microscale mechanical properties of heterogeneous, three-dimensional (3D), soft biomaterials over time. Our approach capitalizes on the ability of ultrasound waves to

penetrate and interact with components in a material at depth and without contact. Besides imaging material morphology and structure (recently reviewed in [29, 30]), ultrasound elastography uses either direct physical compression or remote deformation using acoustic radiation force [31-36], for visualization of relative tissue stiffness (e.g. to identify tumors). A few studies have reported the use of acoustic radiation force to assess relative elastic and viscoelastic properties of a sample [37-40], but have been limited to measuring only bulk properties of samples suspended in solution.

Our technique, named multimode ultrasound viscoelastography (MUVE), uses interleaved ultrasound pulses at two distinct center frequencies to both deform and image soft hydrogel samples at microscale resolution. Focused ultrasound pulses at low frequency (e.g. 1-3 MHz) are used to noninvasively apply a controlled body force (e.g. acoustic radiation force) to selected regions within the sample. Concurrent ultrasound imaging at high frequency (e.g. 10-50 MHz) allows creation of 3D spatial maps of the interior features of the sample, as well as measurement of time-dependent sample deformation or strain at any desired location within the sample. The strain in the sample over time and location are then used to generate a set of quantitative parameters that describe both the elastic and viscoelastic properties of the material. Here, we report on the application of MUVE to characterizing both the bulk and local mechanical properties of commonly used hydrogel biomaterials and demonstrate the ability to discriminate between phases in multiphase materials. We characterize the spatial resolution and detectivity of the technique, and compare MUVE to other commonly-used mechanical measurement methods. This work highlights the distinct ability of MUVE to noninvasively probe the local mechanical properties of soft biomaterials at depth and at the cellular scale.

4.2 Materials and Methods

4.2.1 Synthesis of HA-Agarose Microbeads

Agarose solution (50.0 mg/ml) was prepared by dissolving agarose powder (Sigma Aldrich, St. Louis, MO) in deionized water. Nano-grade hydroxyapatite (HA) solution was prepared at 200 mg/ml in Dulbecco's modified Eagle's medium-low glucose (DMEM; Life Technologies, Grand Island, NY) and sonicated for an hour before use. HA-agarose beads were fabricated by an oil-in-water emulsion method. 1 ml mixture of 80% agarose solution, 5% HA solution, and 15% deionized water was injected into 75 ml polydimethylsiloxane (PDMS; PMX-200,100 cS; Xiameter) under constant stirring using an impeller. Emulsification was carried out at 37 ˚C for 5 min and then on ice for 30 min. To obtain HA-agarose beads of 10-1000 μm diameters, the stirring speed was set to 400 and 500 rpm. HA-agarose beads in PDMS were collected through centrifugation and washing with phosphate buffered saline.

4.2.2 Fabrication of Hydrogel Constructs

To illustrate MUVE's capability of delineating multi-phase multi-material constructs, 40.0 mg/ml HA-agarose beads were embedded in 5.0 mg/ml HA-doped agarose, 2.0 mg/ml HA-doped collagen, and 2.0 mg/ml HA-doped fibrin hydrogels. To determine the size resolution, 40.0 mg/ml HA-agarose beads with various diameters were embedded in 5.0 mg/ml HA-doped agarose gel. HA-doped agarose gel of 5.0, 10.0, 20.0, 30.0 and 40.0 mg/ml containing 40.0 mg/ml HA-agarose beads were tested to determine the detectable contrast in hydrogel composition. For comparing MUVE, nanoindenter, and shear rheometer, HA-doped agarose hydrogels (5.0, 10.0, 20.0, 30.0, and 40.0 mg/ml) and HA-doped fibrin hydrogels (2.0, 6.0 and 10.0 mg/ml) were tested. All hydrogel constructs contained 10.0 mg/ml nano-grade HA.

HA-doped agarose hydrogels were prepared as discussed previously [41, 42]. Briefly, 50.0 mg/ml agarose stock solution was mixed with deionized water and 5% 200mg/ml HA stock solution to obtain selected final agarose concentration. 250 μl of the mixture was injected into a

custom mold. HA-agarose beads were transferred into the mixture, and the mixture was allowed to gel at 4ºC for 30 min. Agarose hydrogel constructs were 9 mm in diameter and 3-4 mm in height.

HA-doped fibrin and collagen hydrogels were fabricated as discussed previously. HA-doped collagen hydrogels were synthesized by mixing 50% 4.0 mg/ml collagen Type I (MP Biomedicals, Solon, OH) in 0.02 N acetic acid, 20% 5X-concentrated Dulbecco's modified Eagles' medium (5X-DMEM; Invitrogen, Carlsbad, CA), 10% fetal bovine serum (FBS; Invitrogen), 5% DMEM, and 5% 200 mg/ml HA stock solution. HA-doped fibrin hydrogels were generated by mixing 83% fibrinogen stock solution (4.0, 12.0, and 20.0 mg/ml), 10% FBS, 2% 50 UT thrombin (Sigma Aldrich) and 5% HA stock solution. 250 µl of the HA-collagen or HA-fibrin mixture were injected into a 48 well plate, and HA-agarose beads were transferred into the mixture for make multi-phase constructs. The mixture was incubated at 37ºC for 30 min for gelation. HA-collagen and HA-fibrin constructs were 10 mm in diameter and 2-3 mm in thickness.

4.2.3 Multimode Ultrasound Viscoelastography (MUVE)

Experimental Setup, Data Acquisition, and Analysis – As described previously [41], the MUVE setup consisted of a 2 MHz FUS transducer (H148; Sonic Concepts, Woodinville, WA; 62.5 mm focal distance, -6 dB focal length of 8.0 mm, -6 dB beam width of 1.5 mm) collinearly aligned with a 10 MHz imaging transducer (Olympus, Waltham, MA; focal distance at 55 mm, –6 dB beam width of 1 mm). The FUS transducer was driven by a waveform generator (33220A; Agilent, Santa Clara, CA) and a power amplifier (75A250; Amplifier Research, Souderton, PA) to deliver a series pulses (1 Hz PRF with 99% duty cycle and 0.7 MPa acoustic pressure) for an 180 s total duration. The imaging transducer was driven by a pulser/receiver (5900 PR; Olympus) to send and acquire signals at 1 Hz or 50 Hz PRF. The imaging pulses were initiated 20 s before the FUS pulses and terminated 150 s after the FUS pulses. Synchronization of the FUS and imaging

pulses was achieved using a pulse/delay generator (Model 565; BNC, San Rafael, CA). Backscattered signals acquired by the imaging transducer were recorded at 250 MSamples/s and stored on an oscilloscope (54380B, Agilent, Santa Clara, CA) for offline analysis.

Hydrogel constructs were first imaged using a high-resolution VEVO 770 imaging system (VisualSonics Inc., Toronto, Canada) to obtain grayscale B-mode and 3D images, as well as raw backscattered data for attenuation measurements [43] (**Table 4-1**). Then samples were placed in a custom holder with agar gel padding for mechanical testing with MUVE. From MUVE, a time series of RF signals were acquired and Hilbert transform was applied to generate M-mode images. Two-step cross-correlation [44] was used to compare signals to the baseline signals before compression to determine displacements within the sample. Displacement values were assigned to each pixel to create displacement color maps (**Figure 4-1**).

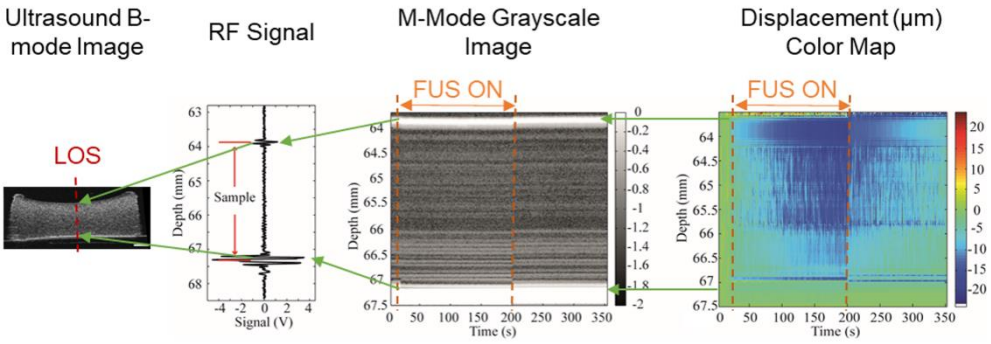

Figure 4-1. MUVE Signal processing procedure. At a selected line of sight (LOS; red dashed line), a series of radio-frequency (RF) signals was acquired before, during and after the focused ultrasound (FUS) pulses, which generates a motion-mode (M-mode) ultrasound image. Using a two-step cross-correlation method, the displacement along the LOS over time was determined and a displacement color map was generated by assigning the displacement value to each pixel. Green arrows indicate sample surfaces.

Mechanical Parameter Extraction – Displacements near the surface of the construct and near the surface of the HA-agarose bead were extracted and presented as displacement-time curves to illustrate mechanical property differences between the hydrogel and bead. To account for differences in sample attenuation coefficient and resulted differences in acoustic radiation force,

compliance was computed by normalizing strain with the stress induced by acoustic radiation force. The ARF acts as a body force in the construct, and the induced stress in the ARF cylinder with radius R_0 and length l_0 was computed as:

$$\sigma_0 = \frac{\int_V F dv}{S_{FUS}} = \frac{\int_0^{R_0}\int_0^{l_0} F(r,z')2\pi r dr dz'}{S_{FUS}}, \quad (1)$$

where S_{FUS} is the FUS bean cross sectional area and the ARF, $F[\mathrm{N/m^3}]$, at a location with radius r and depth z was calculated under a plane wave assumption as:

$$F(r,z) = \frac{2\alpha(r,z)I'(r,z)}{c} = \frac{2\alpha(r,z)I(r,z)e^{-2\alpha(r,z)\cdot z}}{c}, \quad (2)$$

where $\alpha[\mathrm{m^{-1}}]$ is the absorption coefficient, $c[\mathrm{m/s}]$ is the speed of sound in the sample, and $I'[W/m^2]$ is the *in situ* acoustic intensity approximated by the free field intensity *I(r,z)* multiplied by the attenuation factor.

Table 4-1. Sample thickness, attenuation, experienced acoustic radiation force (ARF) as a body force, and creep time for HA-doped agarose and fibrin hydrogels at selected concentrations. Values are shown as mean ± SEM, n = 4.

Construct Type	Concentration (mg/ml)	Sample Thickness (mm)	Attenuation Coefficient (dB/MHz/cm)	ARF (body force, μN)	Creep Time (s)
HA-doped Agarose	5	3.16 ± 0.06	0.198 ± 0.005	5.72 ± 0.24	180
	10	3.15 ± 0.03	0.216 ± 0.004	6.21 ± 0.10	
	20	3.18 ± 0.05	0.231 ± 0.002	6.71 ± 0.14	
	30	3.25 ± 0.06	0.243 ± 0.002	7.20 ± 0.09	
	40	3.23 ± 0.07	0.254 ± 0.003	7.48 ± 0.23	
HA-doped Fibrin	2	2.60 ± 0.08	0.231 ± 0.004	5.48 ± 0.23	
	8	2.43 ± 0.06	0.239 ± 0.005	5.31 ± 0.23	
	10	2.38 ± 0.05	0.252 ± 0.005	5.48 ± 0.18	

The mechanical property was quantified by the maximum strain (max|ε(t)|), residual strain (max|ε(t)|, creep time constant (τ_c), recovery time constant (τ_R) and instantaneous elastic modulus (R_1). Maximum compliance was defined as the highest value of compliance in creep and residual compliance was defined as the steady-state compliance at the end of recovery. Creep and recovery

time constants were derived by fitting the creep and recovery compliance over time with exponential functions. To avoid subjectivity, the instantaneous elastic modulus was derived by fitting the creep compliance with Burger's four-parameter model [45] (**Figure 4-2**):

$$\varepsilon_{creep}(t) = \frac{\sigma_0}{R_1} + \frac{\sigma_0 t}{\eta_1} + \frac{\sigma_0}{R_2}\left[1 - \exp\left(-\frac{R_2}{\eta_2}t\right)\right] . \quad (3)$$

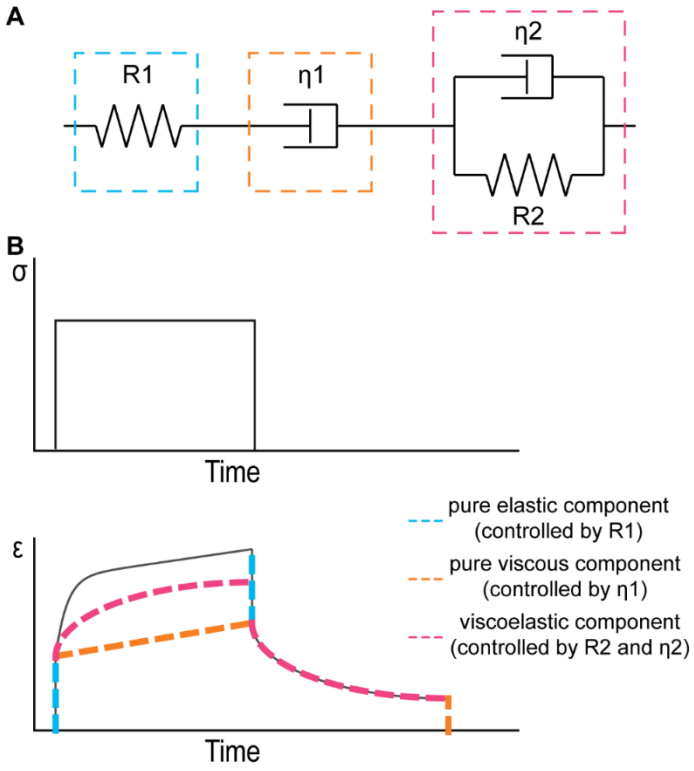

Figure 4-2. A) Spring-dashpot schematic of the Burger's four parameter model. B) Schematic showing the strain-time curve of a viscoelastic material under a step function stress. The strain can be decomposed into three components: a pure elastic component governed by R1 (blue), a pure viscous component governed by η1 (orange), and a viscoelastic component corresponding to the spring and dashpot in parallel governed by R2 and η2 (pink).

Limit of Detection (LOD) – To determine the limit of detection for spatial resolution, the diameter of the microbead was estimated as the distance between the depth where the displacement drops to 5.24 μm (mean displacement at the surface of HA-agarose bead) and the bottom of the construct. The true diameter was determined as the distance between the first positive peak corresponding to the HA-agarose bead surface and the first peak corresponding to the bottom of

the bead in the RF signal. Linear regression of the estimated size against the true size was determined, and the limit of detection was defined as

$$LOD = 3\frac{s}{b}, \quad (4)$$

where s is the standard deviation of the regression and b is the slope of the regression [46].

To determine the LOD for detectivity, the difference between the displacement at the surface of the construct and at the surface of the HA-agarose bead was computed and plotted against the agarose concentration difference between the hydrogel and the bead. Linear regression was applied and LOD was computed as in Eq. (4).

4.2.4 Nanoindentation

Nanoindentation on HA-doped agarose hydrogels and HA-doped fibrin hydrogels was performed using Hysitron TriboIndenter (Hysitron, MN) with a flat-punch probe. A load function of 0.8 s pre-loading, 40.0 s hold time and 0.8 s unload time to mimic the step stress function applied with MUVE (**Table 4-2**). A peak force of 2.0 to 40 μN was applied to the constructs to generate displacement over 1 μm and under 5 μm. Compliance was computed as strain normalized by the peak stress. Maximum compliance (max|J(t)|), creep time constant (τ_c), and instantaneous elastic modulus (R_1) were calculated as described in the previous section. Creep during the hold-time was used for obtaining R_1 by fitting data to the Burger's model to reduce the effect of the slower loading speed compared to MUVE.

Table 4-2. Nanoindentation pre-load, maximum load, load time, hold time and unload time for HA-doped agarose and fibrin hydrogels at selected concentrations. While maintaining the same load, hold and unload time, pre-load was adjusted to accurately determine zero-position and maximum load was adjusted to ensure the maximum sample deformation was under 5µm.

Construct Type	Concentration (mg/ml)	Pre-load (µN)	Max load (µN)	Load Time (s)	Hold Time (s)	Unload Time (s)
HA-doped Agarose	5	1.5	2	0.8	40	0.8
	10	1.5	5			
	20	1.5	10			
	30	5	20			
	40	5	40			
HA-doped Fibrin	2	1.5	2			
	8	1.5	2			
	10	1.5	2			

4.2.5 Shear Rheometry

The storage modulus (G'), and the loss modulus (G'') were determined using AR-G2 rheometer (TA Instruments, New Castle, DE). A 20 mm parallel plate (500 µm apart) and a Peltier stage were used for performing the shear rheometry analysis. Agarose and fibrin gels were casted in-situ by quickly injecting 250 µL of freshly prepared hydrogel mixture directly in the parallel plates. Tests were conduction ($n \geq 3$) at 37˚C for a 15 min time sweep at 1% strain and angular frequency of 1 rad s-1. The storage modulus and loss modulus values were calculated by taking the average values of the linear portion of the curves.

4.2.6 Statistical Analysis

Results were presented as mean ± SEM. Student's two-tailed t-test for unpaired samples was performed to determine differences between groups. Differences were considered statistically significant at $P < 0.05$.

4.3 Results and Discussion

4.3.1 Viscoelastic Characterization using MUVE

MUVE uses co-linearly aligned ultrasound pulses at separate frequencies to both deform and image soft biomaterial samples (**Figure 4-3**A).

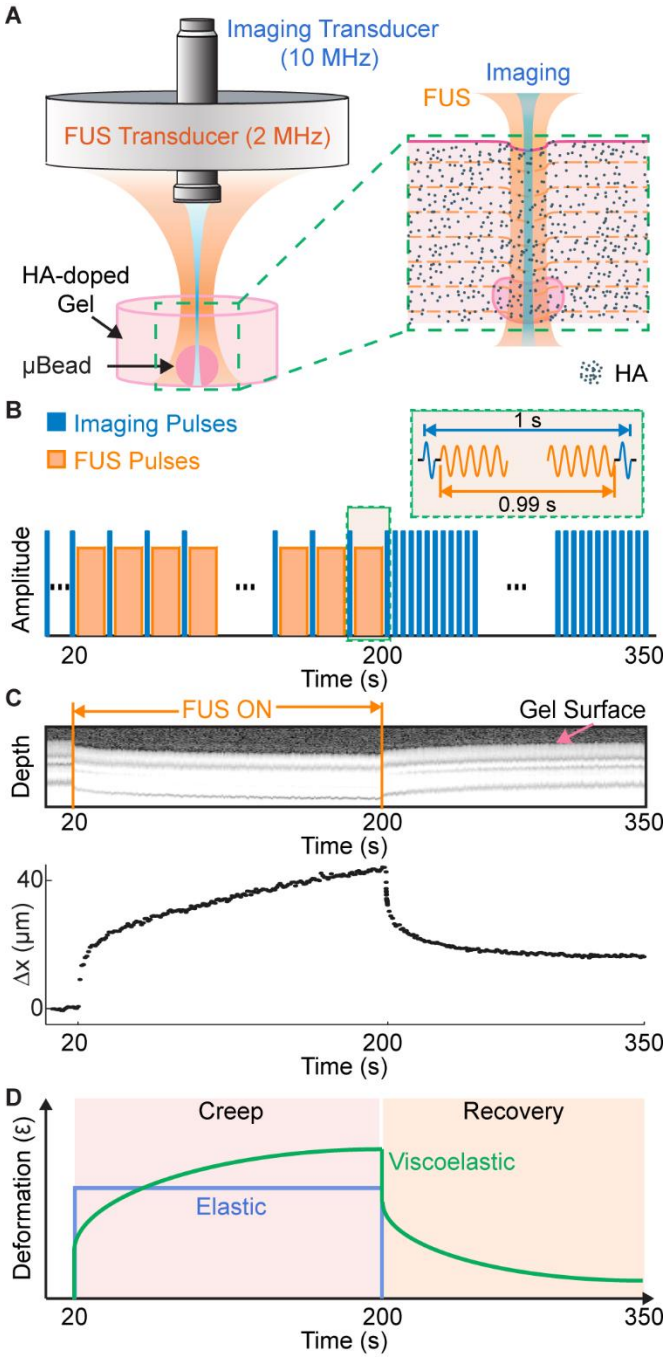

Figure 4-3. A) Schematic diagram of transducer set-up and expanded view of sample in MUVE. B) Schematic trace of the protocol for interleaving focused ultrasound (FUS) pushing and imaging pulses during MUVE for creep testing. C) B-mode image of agarose hydrogel sample showing deformation during application of FUS. D) Schematic of deformation versus time traces for elastic and viscoelastic materials during creep testing.

An annular focused ultrasound (FUS) transducer (2 MHz) is used to apply "pushing" pulses to the sample. The acoustic radiation force (ARF) associated with the "pushing" pulses deforms the sample within a confined volume determined by the focused ultrasound beam profile. A high frequency imaging transducer (10 MHz) is nested in the annular space of the pushing transducer for high resolution pulse-echo imaging and detection of the ARF-induced deformation in the sample over time. Since the ARF is a body force, it acts throughout the volume of the applied ultrasound beam.

We implemented MUVE for testing in creep mode, in which a constant force is applied to the sample and deformation is monitored over time, using interleaved pushing and imaging pulses (**Figure 4-3**B). Ultrasound M-mode imaging was applied before, during, and after sample deformation. FUS was applied to deform the sample for a period of 180 s. To maintain an essentially constant force, the pulse repetition frequency (PRF) was set to 1 Hz at a duty cycle of 99.99%, leaving a short "off" interval of 10 ms for pulse-echo imaging at 1 s intervals to detect sample deformation. The ultrasound imaging data clearly showed sample dimensions and the deformation in the materials over the duration of the creep test (M-mode images and corresponding displacement curve, **Figure 4-3**C). The characteristic deformation over time curve of a sample provides insight into the viscoelastic behavior of the material (**Figure 4-3**D). Purely elastic materials (blue curve) deform instantaneously to a degree determined by their stiffness, and maintain a constant deformation until the load is removed, at which point they recoil fully to their original dimensions. In contrast, viscoelastic materials (green curve) continue to deform over time under a constant load (this behavior is termed "creep"), and also exhibit time-dependent and incomplete recovery when the load is removed. Viscoelastic behavior in hydrogels and tissues is caused by rearrangement of fluid and solid components in the material structure over time.

4.3.2 Material Properties of Multiphase Biomaterials

An advantage of MUVE is that it can be used to spatially characterize multiphase biomaterials. To demonstrate this ability, we prepared constructs consisting of commonly-used hydrogel biomaterials (agarose, collagen, and fibrin) doped with hydroxyapatite (HA) to enhance scattering of the ultrasound signals. These constructs also had embedded within them a high concentration agarose microbead, which was included in the constructs at the time of gel formation, serving as an inclusion with properties distinct from the surrounding hydrogel. Grayscale B-mode ultrasound imaging in 2D (**Figure 4-4**A) and 3D (**Figure 4-5**) showed diffuse distribution of the HA throughout the constructs. In each of the three different matrices, the denser agarose microbead (white arrows) can be visualized. MUVE characterization was performed in these constructs at a line of sight (LOS1) adjacent to the microbead (dashed yellow line), as well as at a LOS2 that included the microbead (dashed red line). Heat maps that represent deformation as function of depth and time before, during, and after sample deformation (**Figure 4-4**B) and the displacement-time curves at the sample surface (**Figure 4-4**C) at LOS1 adjacent to the microbead revealed the properties of the bulk matrix from the applied creep test. Force-induced displacement in the matrix showed characteristic behavior of each of the hydrogel materials (**Figure 4-4**C). Agarose exhibited essentially elastic behavior, with instantaneous deformation of about 10 μm, little creep over time, and recovery to close to the initial dimensions. In contrast, the fibrillar collagen and fibrin hydrogels exhibited a marked creep response, as characterized by increasing deformation over time after application of the constant acoustic force. Collagen and fibrin both showed a relatively rapid recovery response, and collagen recovered to close to its pre-strained dimensions, while fibrin did not.

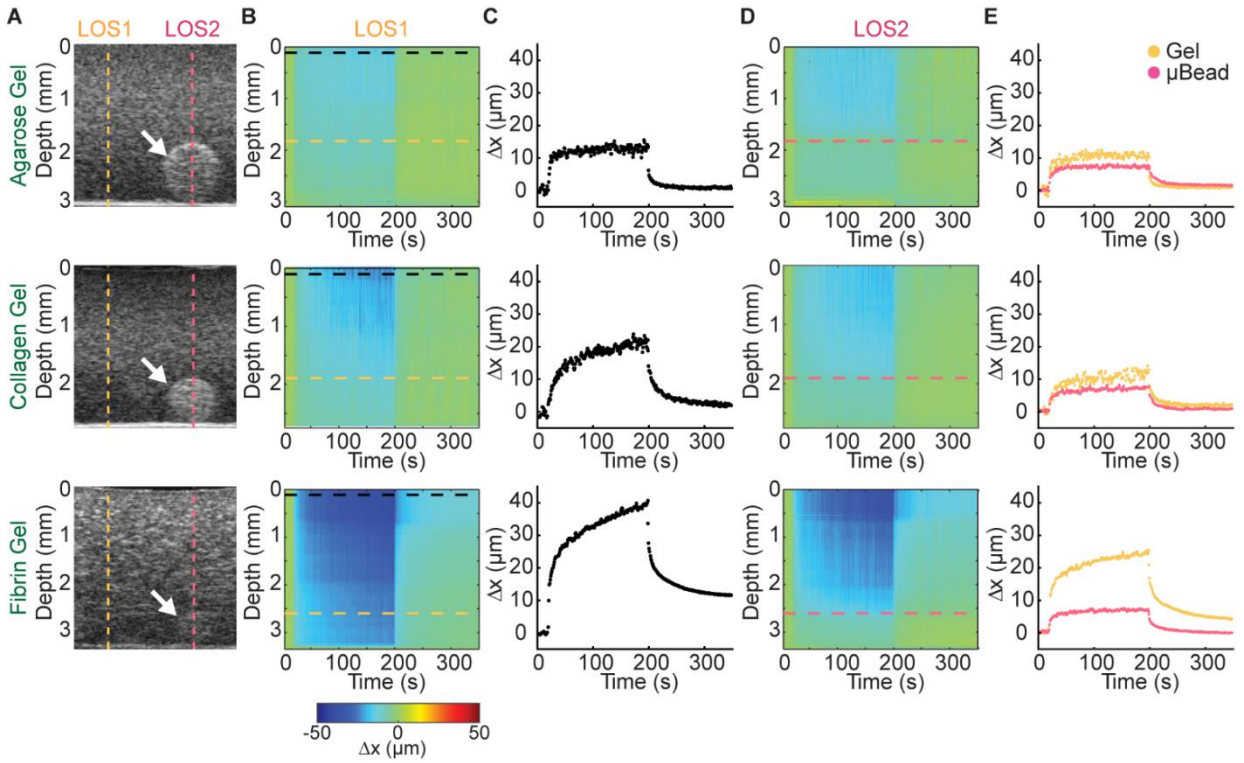

Figure 4-4. A) Grayscale images of HA-doped agarose, collagen and fibrin hydrogels containing HA-doped agarose bead (white arrow). Dashed lines indicate a line of sight (LOS) through a location in the sample without (yellow line) and with (red line) the microbead. B) Displacement color maps corresponding to LOS without microbead. C) Peak displacement profile of the sample at the same depth as the microbead. D) Displacement color map corresponding to a location with the microbead. E) Peak displacement profiles of the LOS without (yellow trace) and with (red trace) the microbead.

Deformation heat maps generated at LOS2 including the microbeads (**Figure 4-4**D) showed decreased deformation at the location of the microbead, due to its high agarose concentration and therefore relatively stiffer matrix compared to the surrounding matrix. In each case, the microbead can be distinguished from the surrounding matrix material by examining its response to the pushing pulse and the resulting displacement-over-time curve (**Figure 4-4**E). In the agarose hydrogel, both the microbead and the surrounding gel exhibited little creep-characteristic behavior, but as expected, the stiffer 40 mg/mL microbead deformed less than the surrounding 5 mg/mL gel. In the collagen and fibrin materials, the agarose microbead can again easily be identified from the surrounding gel, both through its lower degree of deformation and by

its distinctly more elastic behavior, as demonstrated by the shape of the displacement over time curve. It is important to note that even if the microbead is indistinguishable from the surrounding matrix in grey-scale B-mode imaging (fibrin bead in **Figure 4-4**A), MUVE is able to detect it based on its mechanical property (**Figure 4-4**E).

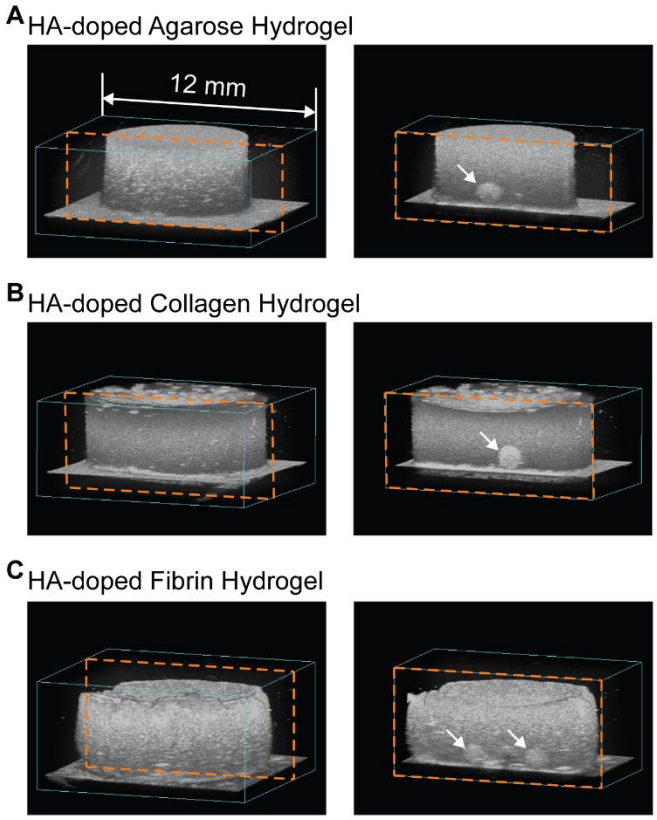

Figure 4-5. 3D rendered ultrasound images of HA-doped (A) agarose, (B) collagen and (C) fibrin hydrogels containing HA-doped agarose bead (white arrows). Left column shows the entire construct. Right column shows a cross-section containing the HA-doped agarose bead.

We obtained strain-time curve from the deformation over time data to allow extraction of a set of parameters that describe viscoelastic material behavior (shown schematically in **Figure 4-6**A and **Figure 4-2**). The panels in **Figure 4-6**B-F show these extracted parameters from a series of experiments similar to those presented in **Figure 4-4**. An instantaneous elastic modulus (R1, **Figure 4-6**) was derived by fitting the strain data with Burger's Viscoelastic Model [45]. This parameter represents the initial elastic response of the material, which is reflective of the elastic

modulus. MUVE showed that fibrin was the least stiff, and that the agarose and collagen materials had similar stiffness at the concentrations used. As would be expected, these quantitative results also show that the embedded high concentration agarose microbead was stiffer than the surrounding matrix and its properties were independent of the surrounding material. The maximum strain (Max(ε), **Figure 4-6**C) is a measure of the degree of creep after instantaneous deformation and reflects time-dependent behavior of the materials. Fibrin exhibited a significantly greater creep response than the agarose and collagen gels. These data also show that creep over time of the embedded microbead was significantly less than the surrounding gels, and was again essentially invariant across the embedding matrices.

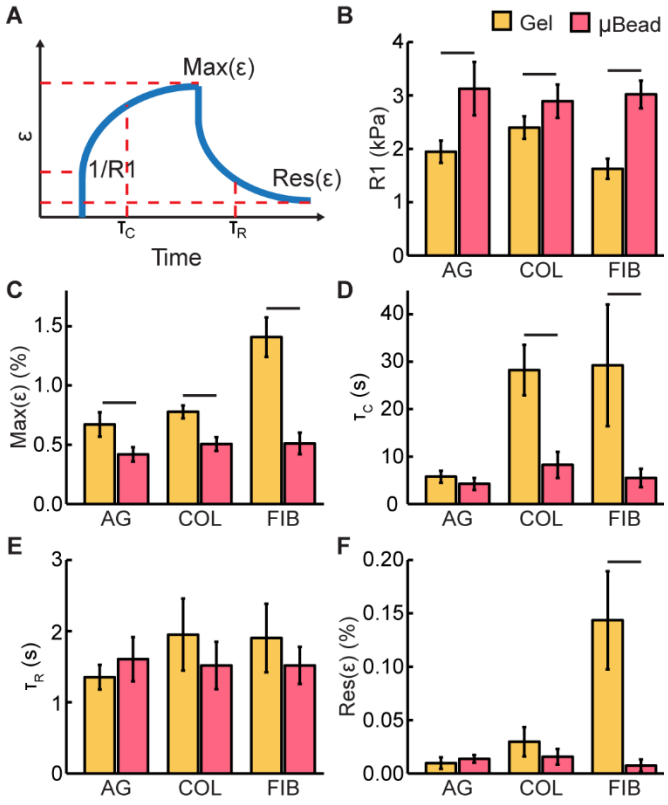

Figure 4-6. A) Schematic showing parameters used to characterize material properties. Parameters derived from creep tests on agarose, collagen, and fibrin hydrogels performed at LOS without (yellow bars) and with (red bars) the microbead: B) instantaneous elastic modulus (R1), C) maximum strain (Max(ε)), D) creep time constant (τ_C), E) relaxation time constant (τ_R), E) residual strain (Res(ε)). Lines above bars indicate $P < 0.05$, n =4.

Curve fitting of the strain-versus-time plots was used to extract time constants for the rate of transition to the creep and recovery phases of the mechanical tests. The larger creep time constant (τ_C, **Figure 4-6**D) for collagen and fibrin corresponded to a more gradual transition to the extended state, relative to the agarose bulk gel and microbead, indicating more viscous influence on material behavior. Interestingly, the recovery time constant (τ_R, **Figure 4-6**E) was similar across materials, and was relatively rapid compared to the creep response. However, the residual strain (Res(ε), **Figure 4-6**F) showed that both agarose and collagen underwent essentially complete recovery to their original dimensions, whereas fibrin exhibited plastic (non-recovered) deformation.

Taken together, these data demonstrate how MUVE can be used to spatially quantify both bulk and regional properties in soft hydrogel matrices. The displacements produced in these experiments were in the range of 5-50 μm, which is at the scale that cells sense through cell-surface receptors and the cytoskeleton [47]. Importantly, the technique can probe regions inside materials and characterize spatial variation in material properties, as demonstrated by the ability to identify and measure the properties of microbeads embedded in surrounding matrices. Finally, all of this testing can be performed under physiological conditions (temperature, pH) and both the deformation and imaging of the sample is entirely noninvasive, allowing longitudinal nondestructive imaging of samples over time.

4.3.3 Spatial Resolution and Detection Sensitivity

The ability to discriminate between materials or between regions within a material based on their mechanical properties is important in characterizing heterogeneity and structure in multiphase materials. The spatial resolution of MUVE depends primarily on the resolution of the pulse-echo ultrasound imaging system being used to acquire signals. The lateral resolution is

determined by the lateral beam width, and is about 450 μm for the 10 MHz system used in this study. The axial resolution can be estimated based on the axial resolution of ultrasound elastography [48]. In this study, the axial resolution was estimated to be about 225 μm.

To experimentally validate the axial resolution of our system, we used a two-phase hydrogel construct to determine the spatial resolution at which MUVE can differentiate between high concentration agarose microbeads of specified sizes (from 300-1000 μm in diameter) embedded in a surrounding low concentration agarose gel (**Figure 4-7**A). The high concentration agarose microbeads could be detected using B-mode imaging (white arrows in **Figure 4-7**B), though as the size decreased, it is difficult to discriminate the microbead from the surrounding matrix. Importantly, heat maps of sample deformation during the application of MUVE (**Figure 4-7**C) revealed the location of the microbead, as evidenced by smaller deformation of the more concentrated microbead matrix. In addition, deformation over time traces (**Figure 4-7**D) clearly revealed the distinct behavior of the high concentration agarose microbead (red trace) and the surrounding agarose gel (magenta trace). As expected, both materials exhibited the characteristic pseudo-elastic behavior of agarose. However, the degree of deformation in the stiffer microbead was significantly smaller than the surrounding hydrogel. A plot of microbead diameter as measured by MUVE versus the nominal microbead diameter (**Figure 4-7**E) showed strong agreement (R=0.93). The limit of MUVE spatial resolution was estimated using the standard deviation and linear regression of this curve [46], and indicated that the current MUVE system can discriminate objects on a size scale of approximately 221 μm, close to the theoretical value of 225 μm.

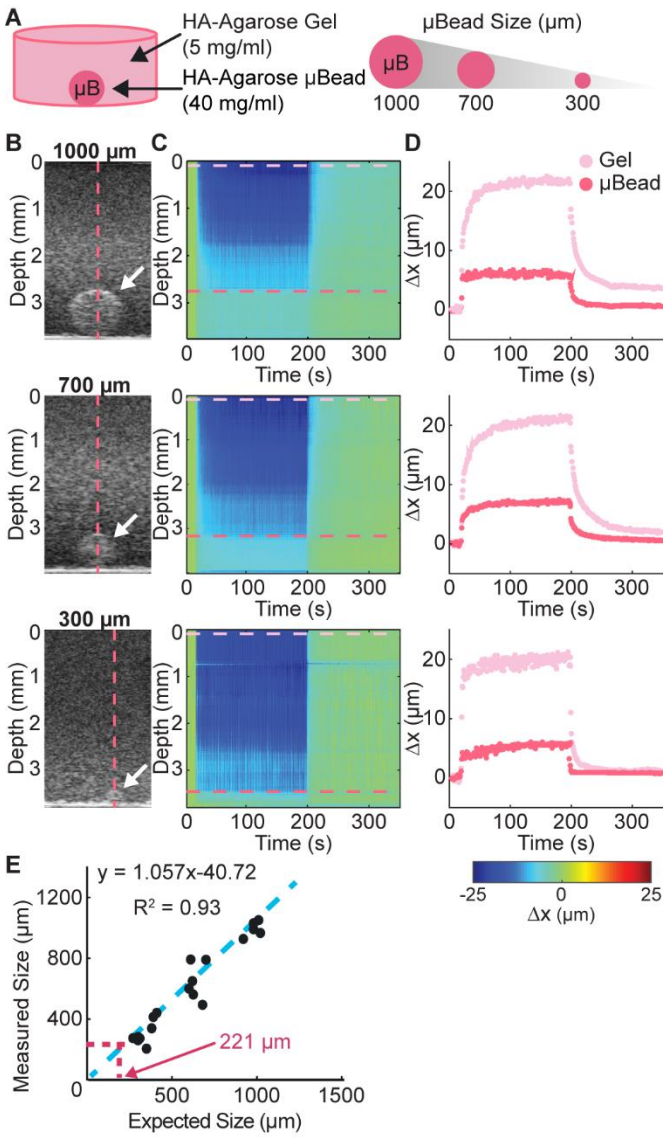

Figure 4-7. A) Schematic of sample configuration showing high concentration agarose microbead embedded within a surrounding hydrogel. Microbead size was varied to determine the spatial resolution of MUVE. B) Grayscale image of sample and microbead (white arrow). C) Color map of deformation through depth of the sample over time. D) Peak displacement profile of the surrounding hydrogel (pink trace) and the embedded microbead (red trace). E) Plot of measured size of microbead versus actual size, showing theoretical size resolution of MUVE.

Detection sensitivity refers to the capability of MUVE to differentiate between materials based on compositional or mechanical property differences. It depends on the minimal detectable difference in displacements due to local spatial variation of material properties, and is also influenced by the signal-to-noise ratio (SNR) of the system. At a given SNR, the displacement of

a material depends on its mechanical properties and the applied force. Since the deforming ARF is constant in our system, any differences in displacements are caused by variations in the mechanical properties of the sample. Therefore, the detection sensitivity can be derived based on the minimal detectable displacement difference.

We assessed the detection sensitivity of MUVE experimentally using agarose constructs of varying concentration (from 5 to 40 mg/mL), that contained an embedded high concentration agarose microbead (40 mg/mL, 1000 μm diameter, **Figure 4-8**A). As the difference in matrix concentration between the microbead and the surrounding matrix decreased from 35 mg/mL to 0 mg/mL, the contrast in grayscale (B-mode) images decreased as expected (**Figure 4-8**B), since the acoustic impedance mismatch between the materials diminishes as the concentrations become more similar. Deformation of the sample during MUVE application as shown in heat maps (**Figure 4-8**B) revealed a similar trend. Similarly, deformation over time traces (**Figure 4-8**C) showed a narrowing of the distance between the trace for the microbead (red trace) and the trace for the surrounding gel (magenta trace) as the difference in matrix concentration between the two phases became smaller. The displacement traces exhibited the characteristic shape for agarose, with a relatively rapid initial deformation and recovery response, and a low degree of creep. Linear regression of the difference in peak displacement versus the difference in agarose concentration between the microbead and surrounding gel (**Figure 4-8**D) showed a strong positive correlation ($R=0.93$). Linear regression was used to estimate that the minimum concentration difference that MUVE can detect in this system is about 10 mg/mL, which corresponds to approximately 0.2 kPa for agarose. In this case, matrix deformation caused directly by MUVE was converted into mechanical properties data, which in turn is reflective of sample composition.

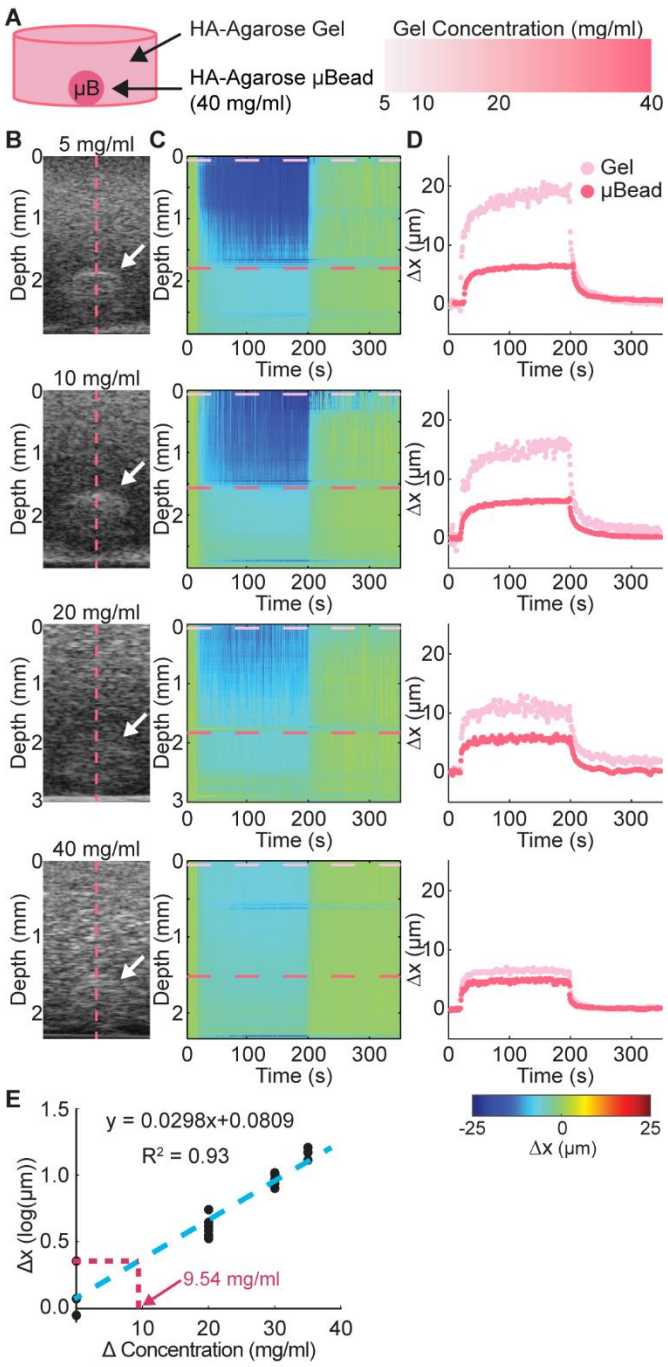

Figure 4-8. A) Schematic of sample configuration showing high concentration (40 mg/ml) agarose microbead embedded within a surrounding hydrogel. Hydrogel concentration was varied to determine the detectivity of MUVE. B) Grayscale image of sample and microbead (white arrow). C) Color map of deformation through depth of the sample over time. D) Peak displacement profile of the surrounding hydrogel (pink trace) and the embedded microbead (red trace). E) Plot of measured deformation difference versus actual concentration, showing theoretical detectivity of MUVE.

4.3.4 Comparison with Nanoindentation and Shear Rheometry

	Multimode Ultrasound Viscoelastography	Nanoindentation	Shear Rheometry
Set-up	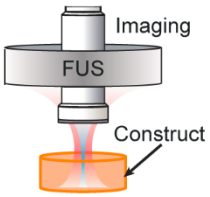	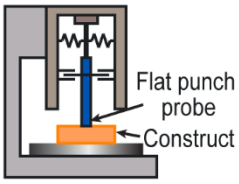	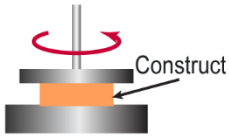
Load Functions	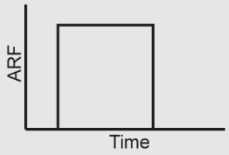	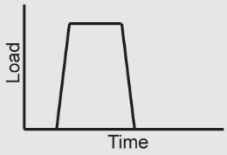	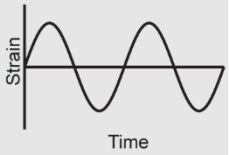
Load Source	acoustic radiation force (body force)	contact force	contact force
Load Mode	compressive	compressive	shear/tangential
Load Application	instantaneous	ramped	cyclic
Localization	lateral & axial	lateral	bulk only
Other	high resolution, microscale deformation	nano to microscale deformation	requires large sample volume

Figure 4-9. Table comparing key features of MUVE, nanoindentation, shear rheometry as methods for characterizing the mechanical properties of soft biomaterials.

We directly compared MUVE with two other techniques commonly used to characterize biomaterials: nanoindentation and shear rheometry (**Figure 4-9**). Each of these methods differs in how the load function is applied and generates a distinct set of parameters. Nanoindentation is typically used only to determine a compressive material modulus under small strains by compression at the surface. Often a reduced elastic modulus is reported [49], which takes into account system parameters, but is difficult to reconcile with very soft samples such as hydrogels. On some instruments, this technique can also be used to run creep tests at microscale deformations. However, the application of load is necessarily gradual and only 2D surface maps of material properties can be generated [50]. Shear rheometry applies tangential force, typically in torsion, and measures only bulk properties [22]. The storage and loss moduli it obtains reflect the elastic

and viscous components of material behavior, respectively. Nanoindentation and related compressive techniques, as well as shear rheometry, require contact with the sample and are therefore difficult to use for longitudinal studies of a specific sample.

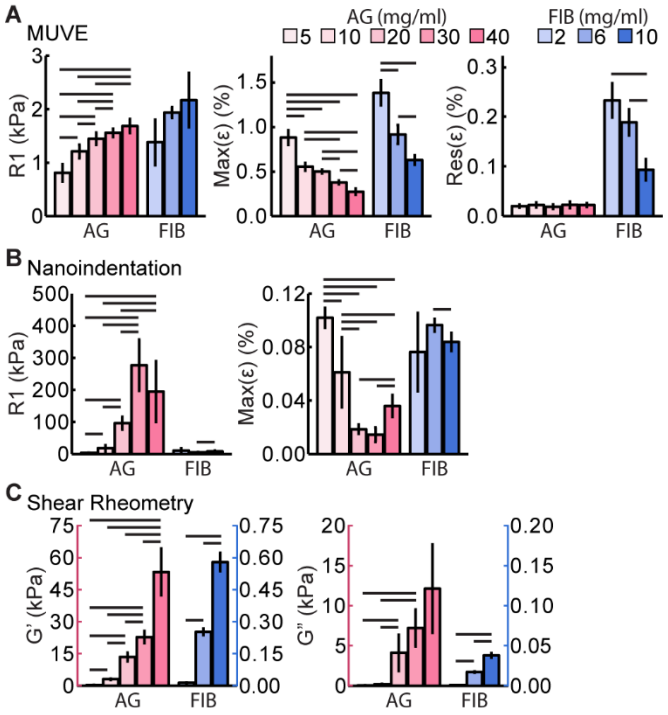

Figure 4-10. Mechanical property parameters of agarose (AG, pink bars) and fibrin (FB, purple bars) hydrogels at a range of concentrations: A) instantaneous elastic modulus (R1), maximum strain (Max(ε)), and residual strain (Res(ε)) as determined by MUVE (n = 4), B) instantaneous elastic modulus (R1) and maximum strain (Max(ε)) as determined by nanoindentation (n > 3), C) storage (G') and loss (G") modulus as determined by shear rheometry (n = 3). Lines above bars indicate $P < 0.05$.

Direct comparison of MUVE, nanoindentation, and shear rheometry was performed through mechanical characterization of agarose and fibrin hydrogels over a range of concentrations. Results using MUVE (**Figure 4-10**A, **Figure 4-11**A, C and E) show clear concentration-dependent increases in the stiffness parameter (R1) in both materials. The maximum strain value (Max(ε)), a measure of the degree of creep response, decreased in a concentration-dependent manner in both materials, suggesting that at higher matrix concentrations both agarose and fibrin behaved more like elastic materials. The residual strain (Res (ε)) in agarose was very

low in agarose and was constant across concentrations, reflecting more elastic behavior. Fibrin exhibited a markedly higher residual strain than agarose, which decreased with increasing concentration, again suggesting that a higher concentration leads to a more elastic matrix.

Analogous creep tests using nanoindentation (**Figure 4-10**B, **Figure 4-11**B, D and F) resulted in a less clear relationship between concentration and the stiffness parameter (R1) in agarose gels, and the method had insufficient sensitivity to distinguish between the fibrin concentrations tested. The maximum strain (Max(ε)) values measured by nanoindentation dropped sharply with increasing agarose concentration, but again this method could not distinguish between fibrin concentrations based on this parameter. Because nanoindentation requires sample contact with the probe, it cannot be used to measure residual strain. The variability and relatively low sensitivity of nanoindentation compared to MUVE when probing soft materials can be attributed to several factors. Because it is a contact-dependent method, adhesion between the probe tip and the sample surface can make it difficult to determine the zero strain position, leading to inaccuracy [51, 52]. This is a particular problem with fibrin materials because of their adhesive nature and high compliance. The rate of strain application is another main difference between creep testing using nanoindentation and MUVE. The full range of deformation of most nanoindentation techniques is small (approx. 5 μm), and often a level of pre-loading is required to determine the zero position. These limitations in working range necessitate a lower stress ramping rate, shorter creep duration and a lower maximum load for softer materials. These conditions are not ideal for satisfying the assumptions associated with the constitutive models for creep tests [53] and limit the sensitivity of the method. In contrast, MUVE applies an essentially instantaneous stress on the sample and can measure the both the zero strain position and subsequent strains noninvasively.

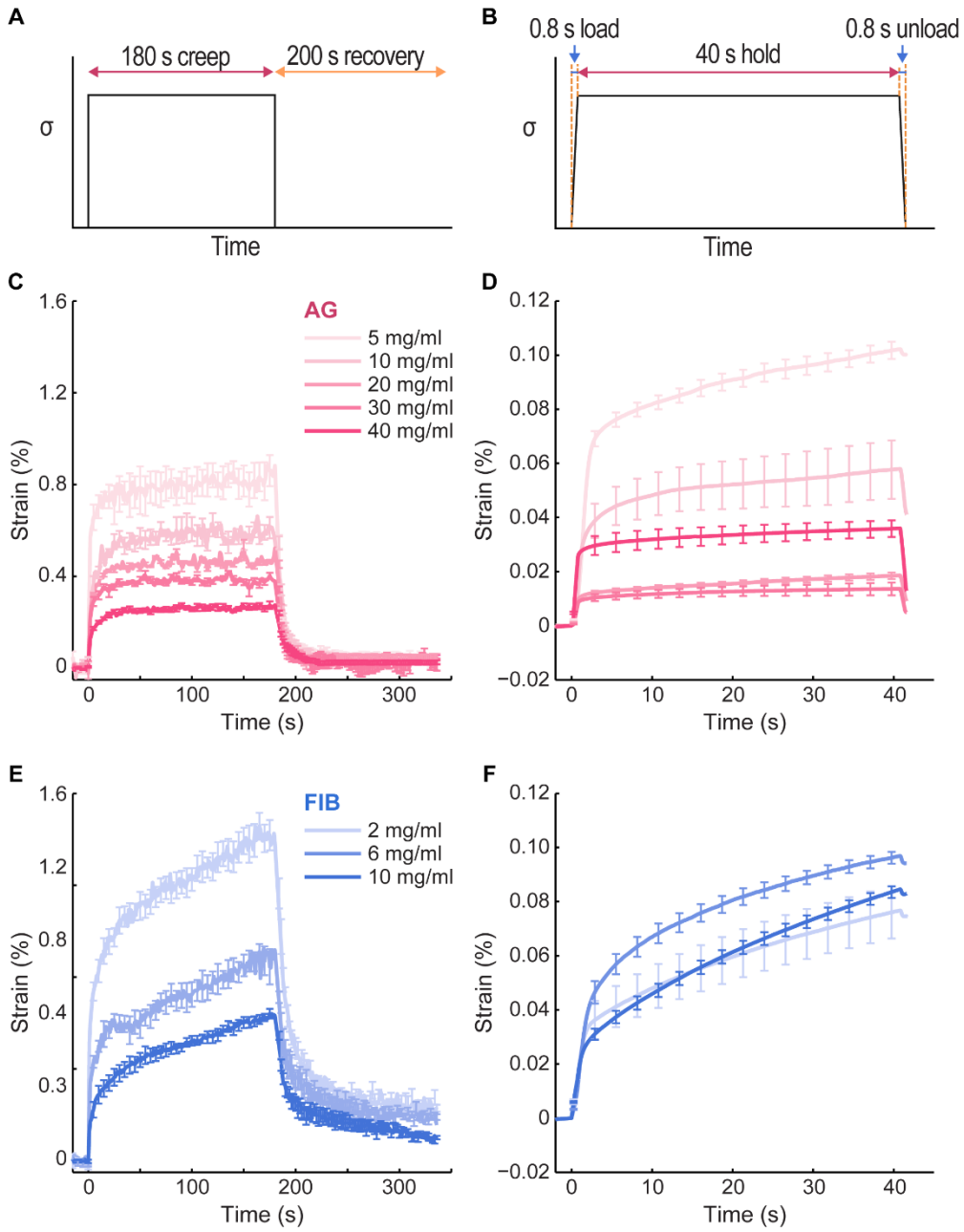

Figure 4-11. Schematic of load function for A) MUVE and B) Nanoindentaion and the induced strain-time curve of C) HA-doped agarose and D) fibrin hydrogels (left column: MUVE; right column: Nanoindentation) at selected concentrations. Curves show the mean ± SEM, n = 4 for MUVE and n>3 for Nanoindentation.

Measurement of macroscopic material properties using shear rheometry (**Figure 4-10**C) revealed clear positive relationships between concentration and both storage (G') and loss (G") moduli in both materials. These trends reflect that both material stiffness and viscous dissipation

increase with concentration in hydrogel matrices. Hydrogels are biphasic materials consisting of a solid network structure intermixed with a fluid component, and these two phases respond differently to shear and compression. The solid network tends to be more resistant in shear and tension than in compression, particularly when the network consists of fibrillar structures as in fibrin hydrogels. Under shear load, the solid network extends and supports most of the load, allowing the network and the fluid to move together with limited interstitial flow. Under compression, the network is buckled and the load is transferred to the fluid phase. This induces relative motion between the network and the solution, which causes interphase drag that is reflected in the time-dependent mechanical properties of the material [23]. These differences in microstructural deformation under shear and compression have been shown to affect overall macroscopic mechanical properties, such that very different properties data may be obtained depending on the testing mode [23]. In general, more compliant hydrogel materials are affected more strongly by the mode of mechanical testing [54].

4.5 Conclusion

These studies show that MUVE can be used to investigate and quantify mechanical behaviors and properties that are characteristic of soft biomaterials. The method can measure mechanical properties, as well as distinguish between materials based on their mechanical behavior. MUVE can provide quantitative data directly from stress-strain relationships, and more complex analysis is possible by fitting appropriate constitutive models and examining the relative contributions of elastic and viscous components. Importantly, the magnitude of the applied deformations is on a scale relevant to cells and their contacts with the extracellular matrix.

A key feature of MUVE is that the ARF is a body force acting on all scattering elements throughout the sample within the beam path. This allows MUVE to spatially interrogate the interior

of 3D materials and map regional heterogeneity at the microscale. The application of ultrasound pulses is also essentially instantaneous, providing a more ideal creep test that better reflects material properties. Importantly, both the imaging and deforming pulses are applied noninvasively to samples in in situ with appropriate physiological conditions, such that MUVE is particularly useful for materials containing living cells and nondestructive longitudinal studies. We have previously used spectral ultrasound imaging to longitudinally monitor the composition of biomaterials and engineered tissue constructs [43, 55]. In addition, the ARF used to create compression during MUVE could also be used to apply defined forces to cells within hydrogel constructs, as a means of mechanically inducing desired phenotype changes. Therefore, by combining separate imaging and pushing transducers, it is potentially possible to apply controlled mechanical stimulation to a sample, while also monitoring the composition and mechanical properties and their spatial distribution. Taken together, these capabilities of advanced ultrasound systems offer a host of possibilities for soft biomaterials characterization and the development of novel mechanobiology-based approaches.

4.6 References

1. Humphrey, J.D., E.R. Dufresne, and M.A. Schwartz, *Mechanotransduction and extracellular matrix homeostasis.* Nature Reviews Molecular Cell Biology, 2014. **15**(12): p. 802-812.
2. Khademhosseini, A. and R. Langer, *A decade of progress in tissue engineering.* Nature Protocols, 2016. **11**(10): p. 1775-1781.
3. Kurniawan, N.A., P.K. Chaudhuri, and C.T. Lim, *Mechanobiology of cell migration in the context of dynamic two-way cell-matrix interactions.* Journal of Biomechanics, 2016. **49**(8): p. 1355-1368.
4. Tibbitt, M.W., et al., *Progress in material design for biomedical applications.* Proceedings of the National Academy of Sciences of the United States of America, 2015. **112**(47): p. 14444-14451.

5. Hall, M.S., et al., *Fibrous nonlinear elasticity enables positive mechanical feedback between cells and ECMs.* Proceedings of the National Academy of Sciences of the United States of America, 2016. **113**(49): p. 14043-14048.

6. Storm, C., et al., *Nonlinear elasticity in biological gels.* Nature, 2005. **435**(7039): p. 191-194.

7. Wen, Q. and P.A. Janmey, *Effects of non-linearity on cell-ECM interactions.* Experimental Cell Research, 2013. **319**(16): p. 2481-2489.

8. Chaudhuri, O., et al., *Substrate stress recovery regulates cell spreading.* Nature Communications, 2015. **6**.

9. Chaudhuri, O., et al., *Hydrogels with tunable stress recovery regulate stem cell fate and activity.* Nature Materials, 2016. **15**(3): p. 326-+.

10. Sommerfeld, S.D. and J.H. Elisseeff, *Time to Relax: Mechanical Stress Release Guides Stem Cell Responses.* Cell Stem Cell, 2016. **18**(2): p. 166-167.

11. Oyen, M.L., *Mechanical characterisation of hydrogel materials.* International Materials Reviews, 2014. **59**(1): p. 44-59.

12. Xiao, Y., et al., *Mechanical Testing of Hydrogels in Cartilage Tissue Engineering: Beyond the Compressive Modulus.* Tissue Engineering Part B-Reviews, 2013. **19**(5): p. 403-412.

13. Meghezi, S., B. Drouin, and D. Mantovani, *Collagen hydrogel-based scaffolds for vascular tissue regeneration: Mechanical and viscoelastic characterization*, in *Characterization of Polymeric Biomaterials*, M.C. Tanzi and S. Fare, Editors. 2017. p. 397-439.

14. Sadat-Shojai, M., M.-T. Khorasani, and A. Jamshidi, *3-Dimensional cell-laden nano-hydroxyapatite/protein hydrogels for bone regeneration applications.* Materials Science & Engineering C-Materials for Biological Applications, 2015. **49**: p. 835-843.

15. Silva, R., B. Fabry, and A.R. Boccaccini, *Fibrous protein-based hydrogels for cell encapsulation.* Biomaterials, 2014. **35**(25): p. 6727-6738.

16. Diekjurgen, D. and D.W. Grainger, *Polysaccharide matrices used in 3D in vitro cell culture systems.* Biomaterials, 2017. **141**: p. 96-115.

17. Loo, Y. and C.A.E. Hauser, *Bioprinting synthetic self-assembling peptide hydrogels for biomedical applications.* Biomedical Materials, 2016. **11**(1).

18. Nie, X., et al., *Dynamic Tensile Testing of Soft Materials.* Experimental Mechanics, 2009. **49**(4): p. 451-458.

19. Gianola, D.S. and C. Eberl, *Micro- and nanoscale tensile testing of materials.* Jom, 2009. **61**(3): p. 24-35.

20. Karimi, A. and M. Navidbakhsh, *Material properties in unconfined compression of gelatin hydrogel for skin tissue engineering applications.* Biomed Tech (Berl), 2014. **59**(6): p. 479-86.

21. Wang, Z.X., A.A. Volinsky, and N.D. Gallant, *Crosslinking Effect on Polydimethylsiloxane Elastic Modulus Measured by Custom-Built Compression Instrument.* Journal of Applied Polymer Science, 2014. **131**(22).

22. Chen, D.T.N., et al., *Rheology of Soft Materials*, in *Annual Review of Condensed Matter Physics, Vol 1*, J.S. Langer, Editor. 2010. p. 301-322.

23. Knapp, D.M., et al., *Rheology of reconstituted type I collagen gel in confined compression.* Journal of Rheology, 1997. **41**(5): p. 971-993.

24. Vanderhooft, J.L., et al., *Rheological Properties of Cross-Linked Hyaluronan-Gelatin Hydrogels for Tissue Engineering.* Macromolecular Bioscience, 2009. **9**(1): p. 20-28.

25. Ebenstein, D.M., *NANOINDENTATION OF SOFT TISSUES AND OTHER BIOLOGICAL MATERIALS*. Handbook of Nanoindentation with Biological Applications, ed. M.L. Oyen. 2010. 279-324.

26. Liu, K., M.R. VanLandingham, and T.C. Ovaert, *Mechanical characterization of soft viscoelastic gels via indentation and optimization-based inverse finite element analysis.* Journal of the Mechanical Behavior of Biomedical Materials, 2009. **2**(4): p. 355-363.

27. Zhu, Y., et al., *Determination of mechanical properties of soft tissue scaffolds by atomic force microscopy nanoindentation.* Journal of Biomechanics, 2011. **44**(13): p. 2356-2361.

28. Kotlarchyk, M.A., E.L. Botvinick, and A.J. Putnam, *Characterization of hydrogel microstructure using laser tweezers particle tracking and confocal reflection imaging.* Journal of Physics-Condensed Matter, 2010. **22**(19).

29. Deng, C.X., X. Hong, and J.P. Stegemann, *Ultrasound Imaging Techniques for Spatiotemporal Characterization of Composition, Microstructure, and Mechanical Properties in Tissue Engineering.* Tissue Engineering Part B-Reviews, 2016. **22**(4): p. 311-321.

30. Doherty, J.R., et al., *Acoustic Radiation Force Elasticity Imaging in Diagnostic Ultrasound.* Ieee Transactions on Ultrasonics Ferroelectrics and Frequency Control, 2013. **60**(4): p. 685-701.

31. Drakonaki, E.E., G.M. Allen, and D.J. Wilson, *Ultrasound elastography for musculoskeletal applications.* British Journal of Radiology, 2012. **85**(1019): p. 1435-1445.

32. Evans, A., et al., *Quantitative shear wave ultrasound elastography: initial experience in solid breast masses.* Breast Cancer Research, 2010. **12**(6).

33. Nightingale, K., et al., *Acoustic radiation force impulse imaging: In vivo demonstration of clinical feasibility.* Ultrasound in Medicine and Biology, 2002. **28**(2): p. 227-235.

34. Ophir, J., et al., *Elastography: ultrasonic estimation and imaging of the elastic properties of tissues.* Proceedings of the Institution of Mechanical Engineers Part H-Journal of Engineering in Medicine, 1999. **213**(H3): p. 203-233.

35. Sandrin, L., et al., *Transient elastography: A new noninvasive method for assessment of hepatic fibrosis.* Ultrasound in Medicine and Biology, 2003. **29**(12): p. 1705-1713.

36. Varghese, T., *Quasi-Static Ultrasound Elastography.* Ultrasound clinics, 2009. **4**(3): p. 323-338.

37. Guzina, B.B., et al., *Viscoelastic characterization of thin tissues using acoustic radiation force and model-based inversion.* Physics in Medicine and Biology, 2009. **54**(13): p. 4089-4112.

38. Liu, D. and E.S. Ebbini, *Viscoelastic property measurement in thin tissue constructs using ultrasound.* Ieee Transactions on Ultrasonics Ferroelectrics and Frequency Control, 2008. **55**(2): p. 368-383.

39. Schmitt, C., A.H. Henni, and G. Cloutier, *Characterization of blood clot viscoelasticity by dynamic ultrasound elastography and modeling of the rheological behavior.* Journal of Biomechanics, 2011. **44**(4): p. 622-629.

40. Walker, W.F., F.J. Fernandez, and L.A. Negron, *A method of imaging viscoelastic parameters with acoustic radiation force.* Physics in Medicine and Biology, 2000. **45**(6): p. 1437-1447.

41. Hong, X., J.P. Stegemann, and C.X. Deng, *Microscale characterization of the viscoelastic properties of hydrogel biomaterials using dual-mode ultrasound elastography.* Biomaterials, 2016. **88**: p. 12-24.

42. Cummings, C.L., et al., *Properties of engineered vascular constructs made from collagen, fibrin, and collagen-fibrin mixtures.* Biomaterials, 2004. **25**(17): p. 3699-3706.

43. Gudur, M., et al., *Noninvasive, Quantitative, Spatiotemporal Characterization of Mineralization in Three-Dimensional Collagen Hydrogels Using High-Resolution Spectral Ultrasound Imaging.* Tissue Engineering Part C-Methods, 2012. **18**(12): p. 935-946.

44. Chen, H., H. Shi, and T. Varghese, *Improvement of elastographic displacement estimation using a two-step cross-correlation method.* Ultrasound in Medicine and Biology, 2007. **33**(1): p. 48-56.

45. Berglund, J.D., R.M. Nerem, and A. Sambanis, *Viscoelastic testing methodologies for tissue engineered blood vessels.* Journal of Biomechanical Engineering-Transactions of the Asme, 2005. **127**(7): p. 1176-1184.

46. Sanagi, M.M., et al., *Comparison of Signal-to-Noise, Blank Determination, and Linear Regression Methods for the Estimation of Detection and Quantification Limits for Volatile Organic Compounds by Gas Chromatography.* Journal of Aoac International, 2009. **92**(6): p. 1833-1838.

47. Quinn, T.M., et al., *Mechanical compression alters proteoglycan deposition and matrix deformation around individual cells in cartilage explants.* J Cell Sci, 1998. **111 (Pt 5)**: p. 573-83.

48. Righetti, R., J. Ophir, and P. Ktonas, *Axial resolution in elastography.* Ultrasound in Medicine and Biology, 2002. **28**(1): p. 101-113.

49. Ebenstein, D.M. and L.A. Pruitt, *Nanoindentation of soft hydrated materials for application to vascular tissues.* Journal of Biomedical Materials Research Part A, 2004. **69A**(2): p. 222-232.

50. Fischer-Cripps, A.C., *A simple phenomenological approach to nanoindentation creep.* Materials Science and Engineering a-Structural Materials Properties Microstructure and Processing, 2004. **385**(1-2): p. 74-82.

51. Kaufman, J.D. and C.M. Klapperich, *Surface detection errors cause overestimation of the modulus in nanoindentation on soft materials.* Journal of the Mechanical Behavior of Biomedical Materials, 2009. **2**(4): p. 312-317.

52. Ebenstein, D.M. and L.A. Pruitt, *Nanoindentation of biological materials.* Nano Today, 2006. **1**(3): p. 26-33.

53. Cheng, L., et al., *Flat-punch indentation of viscoelastic material.* Journal of Polymer Science Part B-Polymer Physics, 2000. **38**(1): p. 10-22.

54. White, C.C., et al., *Viscoelastic characterization of polymers using instrumented indentation. II. Dynamic testing.* Journal of Polymer Science Part B-Polymer Physics, 2005. **43**(14): p. 1812-1824.

55. Gudur, M.S.R., et al., *Noninvasive Quantification of In Vitro Osteoblastic Differentiation in 3D Engineered Tissue Constructs Using Spectral Ultrasound Imaging.* Plos One, 2014. **9**(1)

Chapter 5 Enhancement of Osteogenic Differentiation and Mineral Deposition Using Focused Pulsed Acoustic Straining (FPAS)

5.1 Introduction

Dynamic mechanical stimulation plays a critical role in regulating cell function and fate [1-3], especially for mesenchymal stem cells (MSCs) which are highly sensitive to mechanical stimuli [4]. MSCs have the potential to take multiple lineages including osteogenesis, chondrogenesis and adipogenesis [5, 6]. Control over the MSC differentiation is critical in tissue regeneration as unbalanced differentiation can lead to bone metabolic disease [7, 8]. Various studies have shown that mechanical stimulations in the form of tensile, compressive, shear and vibrational load have been shown to effectively promote osteogenic differentiation in MSCs [9-17], while lack of mechanical stimulation can induce cell apoptosis [18].

A noninvasive approach to apply mechanical stimulation is to use low-intensity pulse ultrasound (LIPUS), which is a Food and Drug Administration (FDA) approved technique and has been widely used in *in vitro* and clinical studies [19]. In animal and clinical studies, it has been shown to strengthen callus [20], accelerate fracture healing [21, 22], and effectively treat delayed unions [23] and nonunion [24, 25] . Various studies have investigated the effect of LIPUS on stem cells, preosteoblastic cells and bone cells [26-28] in both monolayer cultures and 3D scaffolds and shown that LIPUS promotes cell proliferation and osteogenic differentiation [29-32] and chondrogenesis [33] while suppressing adipogenesis [34, 35]. Energy transmitted via LIPUS can act on integrin, mechanosensitive ion channels and gap junctions, and promote focal adhesion formation and matrix deposition [36-40]. LIPUS has been found to trigger various biochemical

events in the cellular level [41-44] and several signaling pathways including integrin/phosphatidylinositol 3-OH kinase (PI3K)/Akt and ROCK-Cot/Tpl2-MEK-extracellular regulated kinase (ERK) pathway are involved in the mechanotransduction associated with LIPUS [40, 45-48]. Effective LIPUS intensities ranges from 10 to 300 mW/cm^2 for different applications [49-51]. Other than intensity, transducer center frequency, duty cycle, pulse repetition frequency (PRF) and treatment duration can all influence the outcome of LIPUS [52-55] and a typical combination of 1.5 MHz center frequency, 20% duty cycle, 1 kHz PRF, 30 mW/cm^2 intensity for 20 min daily treatment has been widely accepted and used. Further enhancement in acceleration fracture healing and promoting osteogenesis has been achieved when combining LIPUS with other mechanical stimuli such as microgravity, vibration or cyclic strain [31, 56, 57].

In this work, we took advantages of the capability of acoustic radiation force (ARF) to induce microscale deformation [58, 59] and developed an ultrasound-based treatment to apply cyclic compression on cellular constructs to enhance osteogenic differentiation and mineral deposition. This stimulation method utilizes ultrasound with higher intensity (around 15 W/cm^2), higher duty cycle (50%) and lower PRF (0.2 to 10 Hz) compared to conventional LIPUS, and induces cyclic deformation at the cell scale (3 to 50 μm) in the cellular collagen/fibrin (COL/FIB) hydrogels seeded with hMSCs. We examined the influence of the treatment on cell viability in COL/FIB hydrogels at selected ultrasound intensities and pulse repetition frequency (PRF). We also investigated how PRF, treatment dosage and osteogenic medium supplements influence osteogenesis. As cells differentiate and remodel the matrix, the mechanical properties of the cellular constructs change over time. We characterized the strain profiles at selected time points and explored the influence of adaptively changing the treatment intensities. This work focuses on

utilizing therapeutic ultrasound in a distinct mode to cyclically compress engineered tissue constructs at the cell scale to promote osteogenesis in conjunction with cell therapy.

5.2 Materials and Methods

5.2.1 Cell Culture

Human mesenchymal stem cells (RoosterBio, Frederick, MD) were cultured in Dulbecco's modified Eagle's medium (DMEM; Life Technologies, Grand Island, NY) supplemented with 10% fetal bovine serum (FBS; Life Technologies) and 1% penicillin and streptomycin (P/S: Life Technologies). Media was changed every three days and cells were used at passage 4 to 6.

5.2.2 Collagen/Fibrin Cellular Hydrogel Fabrication

Collagen/Fibrin composite hydrogels were fabricated as previously described [60]. Briefly, bovine skin type I collagen (MP Biomedicals, Solon, OH) and bovine fibrinogen (MP Biomedicals, Solon, OH) were prepared at 4.0 mg/ml in 0.02 N acetic acid and DMEM respectively. Collagen and fibrinogen solution at 40/60 volume ratio were then mixed with 10% DMEM, 10% FBS, 20% 5X-concentrated DMEM, 5% 0.1 N NaOH (Sigma Aldrich, St. Louis, MO), 2% 50 UT/ml thrombin (Sigma), and cell suspension in DMEM, which yielded a final total protein concentration of 2.0 mg/ml and a cell concentration of 0.5×10^6 cells/ml. A 500 µl mixture was then injected into a 24-well plate and incubated at 37 °C for 30 min to form the hydrogel.

Cellular constructs were cultured in growth media (GM) containing of α-MEM (Life Technologies) without ascorbic acid supplemented with 10% FBS and 1% P/S. To induce osteogenic differentiation, constructs were cultured in osteogenic medium (OM) containing GM with 10 mM beta-glycerol phosphate (β-GP; Sigma), 50 µg/ml ascorbic acid 2-phosphate (Sigma) and 100 nm dexamethasone (DEX; Sigma). All medium was changed every other day.

5.2.3 Focused Pulsed Acoustic Straining Treatment Development

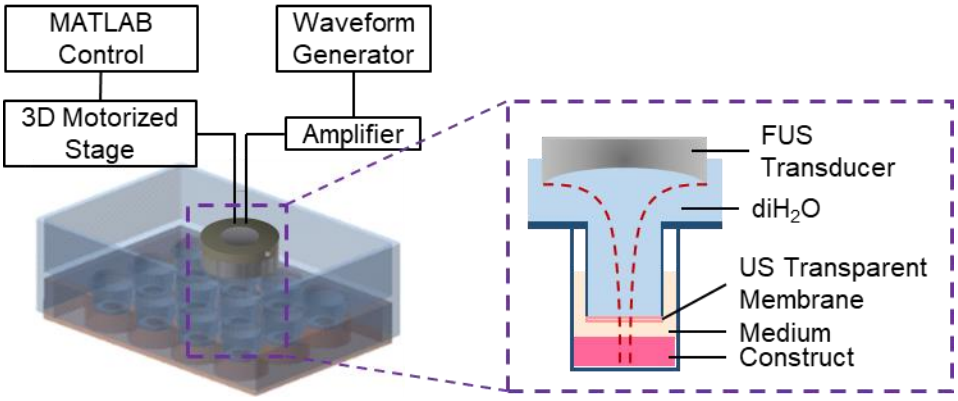

Figure 5-1. Experimental setup for focused pulsed acoustic straining.

Local cyclic compression on cellular constructs was applied using a 2 MHz FUS transducer with an annular aperture (H148; Sonic Concepts, Woodinville, WA). The transducer was calibrated using a hydrophone (HNR-0500; Onda, Sunnyvale, CA) to map the 3D beam profile in free field. It has a 6 dB axial beam depth of 8.0 mm and a lateral beam width of 1.5 mm. To raster scan the entire construct, the FUS was mounted to a 3D motorized stage and a custom MATLAB script was used to create a 5 x 5 scanning grid with 2 mm spacing (**Figure 5-1**). Straining was applied at each location for 5 s to minimize thermal effects. A custom 24-well plate lid with inserts was used to separate the medium in the well plate from the diH_2O in the transducer housing **(Figure 5-2**) to create sterile environment for the cellular constructs. An ultrasound transparent membrane was attached at the bottom of the insert to ensure maximum transmission of the ultrasound energy. The transducer was driven by a signal generator (33220A; Agilent, Santa Clara, CA) and a power amplifier (75A250; Amplifier Research, Souderton, PA) to deliver acoustic radiation force in a pulsed manner for cyclic compression of the constructs. Ultrasound pulses with 50% duty cycle, pulse repetition frequency (PRF) of 10, 1, and 0.2 Hz at an acoustic pressure level of 0.7 MPa (16.7 W/cm2) was applied. Constructs were treated for a total of 30 min or 6 h

(two 3 h sessions) daily. Bottom of the well plate was submerged in a 37 °C water bath during the treatment.

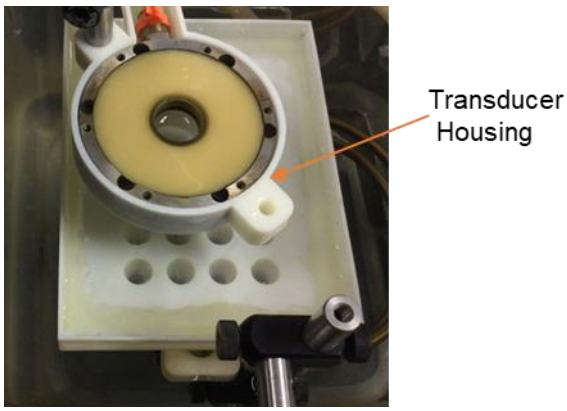

Figure 5-2. FUS transducer in custom built housing.

5.2.4 Cell Viability

Cell viability was assessed with a commercially available vital staining kit (Live/Dead®, Molecular Probes, Eugene, OR) as previously described [61]. Cellular constructs were washed with phosphate buffered saline (PBS) three times, incubated in a solution containing 1 μm calcein-AM and 2 μm ethidium homodimer at 37 °C for 45 min, followed by another PBS wash before imaging on a fluorescence microscope. Cell viability was quantified using ImageJ software (National Institute of Health, Bethesda, MD).

5.2.5 DNA, Alkaline Phosphatase and Calcium Quantification

Cellular DNA content, alkaline phosphatase (ALP) activity and calcium were quantified as previously [61]. Briefly, for DNA content and ALP activity assessment, constructs were permeabilized in 0.2% Triton-X 100 (Sigma) in PBS and sonicated to break down the matrix. DNA was measured using the Quanti-iT^{TM} Picogreen® kit (Invitrogen) following the manufacturer's protocol. To measure the ALP activity, sample lysate was mixed with 5.0 mM p-nitrophenol substrate (Sigma) in 1.5 M 2-amino-2-methyl-1-propanol (Sigma) buffer. The reaction was carried

out in 37 °C for 30 min, and samples were read spectrophotometrically at 405 nm. For calcium quantification, samples were dissolved in 1 N acetic acid on a shaker plate overnight. Sample lysate was then assayed with the orthocresolphthalein complex one (OCPC) method.

5.2.7 Ultrasound Volume Quantification, Spectral Ultrasound Imaging (SUSI) and Multimode Ultrasound Viscoelastography (MUVE)

Construct volume, spectral characteristics and viscoelastic properties were assessed as previously described [59, 62, 63]. Briefly, cellular constructs were imaged with a 55 MHz probe (Vevo 708) on the VEVO 770 imaging system (VisualSonics Inc., Toronto, Canada) to acquire 3D and radio-frequency signals for assessing construct volume and spectral parameters at day 0, 7, 14, and 21. Volume of the construct was measured by integrating the cross-sectional areas from the 3D image data using a built-in semi-automated algorithm. As a means to assess mineralization, acoustic concentration was obtained from spectral ultrasound imaging analysis by applying linear fit to the calibrated and gated power spectrum of the engineered constructs. Viscoelastic properties were measured using the Multimode Ultrasound Viscoelastography (MUVE) system by applying a 180 s compressive acoustic radiation force with the 2 MHz FUS transducer while imaging the deformation with a 10 MHz imaging transducer [59]. The maximum compliance and recovery time constants are reported.

5.2.6 Statistical Analysis

All quantitative data were presented as mean ± standard error, and analyzed with one-way analysis of variance (ANOVA) followed by multiple comparison. The difference is considered significant if $p < 0.05$. n = 3 samples for cell viability, biochemical assays and ultrasound characterizations.

5.3 Results and Discussion

5.3.1 Cell Viability

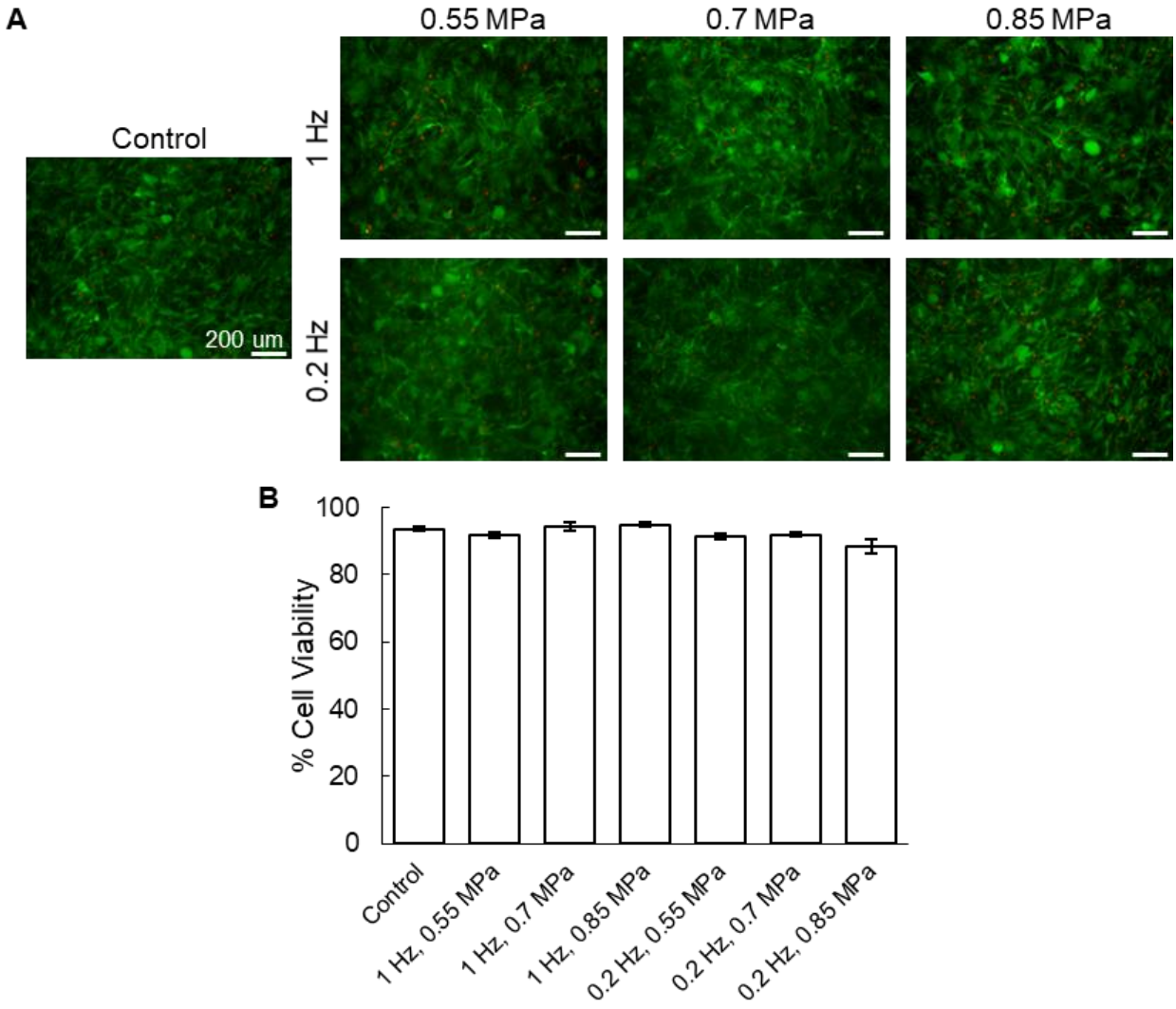

Figure 5-3. A) Visualization and B) quantification of cell viability after 3 days of exposure to focused pulsed acoustic straining with 1 and 0.2 Hz PRF, 0.55, 0.70 and 0.85 MPa acoustic pressure. N = 3.

Based on our previous studies on characterizing the viscoelastic properties of protein hydrogels [64], acoustic radiation force (ARF) can be applied to strain cellular constructs as a body force. Acoustic pressure level between 0.55 MPa and 0.85 MPa has been shown to induce microscale deformation (3 to 50 μm) in the tissue constructs without raising the temperature in the

sample over 2 °C. To cyclically compress the constructs, ARF was applied in a pulsed manner with 50% duty cycle and the transducer was moved with a motorized stage to treat the entire construct. To assess the safety of the treatment, collagen/fibrin (COL/FIB) composite hydrogels encapsulated with human mesenchymal stem cells (hMSCs) were exposed to focused pulsed acoustic straining for 30 min daily for three days with two selected PRFs (1 Hz and 0.2 Hz) and three acoustic pressure levels (0.55, 0.70, 0.85 MPa). In all conditions, cell viability in the COL/FIB hydrogels were above 85% with no significant difference between any ultrasound treated groups and the untreated control group (**Figure 5-3**). These results clearly show that the experimental setup and the ultrasound straining treatment did not comprise cell survival in the hydrogels.

5.3.2 Pulse Repetition Rate

Pulse repetition frequency (PRF) is a key factor in designing the waveform for cyclic stress application. With the same duty cycle and acoustic pressure level, same amount of total energy is delivered to the sample within a given period of time regardless of the PRF. However, the PRF changes the induced deformation in the COL/FIB hydrogels due to their viscoelastic properties, which exhibit time-dependent deformation behavior [65]. To characterize the strain profile at selected PRF, a 10 MHz transducer was used to monitor the sample deformation while the sample was deformed with the focused ultrasound (FUS) transducer. As shown in **Figure 5-4**, at 10 Hz PRF, the sample was deformed more frequently yet with a lower maximum strain in each cycle compared to samples treated with lower PRF. As PRF decreases to 1 Hz and 0.2 Hz, hydrogels were allowed to creep or a longer period of time in each cycle which results in higher maximum deformation but fewer cycles can be delivered within a given time frame. At 0.2 Hz, the hydrogel also had the longest time (2.5 s) to recover.

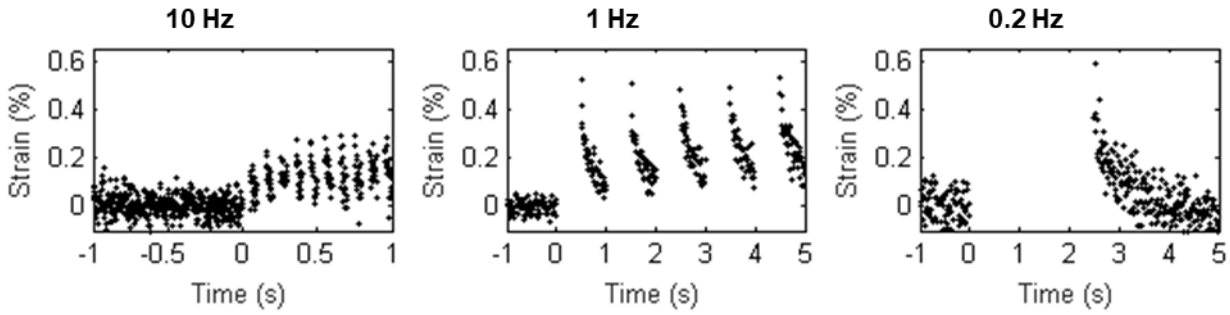

Figure 5-4. Representative images of strain behavior of COL/FIB cellular hydrogels when exposed to ARF at 10, 1, and 0.2 Hz.

To assess the influence of PRF and resulted difference in induced strain behavior on osteogenic differentiation, cellular constructs cultured in osteogenic medium were treated with acoustic straining at 0.7 MPa acoustic pressure with 10, 1 and 0.2 Hz PRF for 30 min daily till day 7. Bright field images of the constructs were taken at day 7 (**Figure 5-5**A) and calcium deposits were observed in constructs cultured in osteogenic medium, with higher coverage for constructs treated with 1 Hz and 0.2 Hz. DNA content (**Figure 5-5**B), alkaline phosphatase (ALP) activities (**Figure 5-5**C) and calcium content (**Figure 5-5**D) were quantified at day 0, 3, 5 and 7. There was no significant difference between any conditions at day 0, 3, and 5. At day 7, there was a significant decrease in DNA content in samples treated with 1 Hz PRF ultrasound compared to the untreated osteogenic samples. ALP activity was significantly higher in the 1 Hz treated group at day 3 and day 5. The 0.2 Hz group even though showed a similar level of ALP activity to the untreated group before day 5, it showed the highest level of ALP activity at day 7. On the other hand, the 10 Hz PRF group showed similar level of ALP to the untreated group at all four time points. To assess the mineralization, the 1 Hz PRF group started mineralization earlier and the calcium amount was highest among the groups (15.3% increase compared to the untreated group). The 0.2 Hz group showed the second highest calcium deposition (11.86% increase compared to the untreated group) while the 10 Hz group showed similar calcium content as the untreated counterpart. The results

clearly showed that the 1 Hz and 0.2 Hz has more enhancement in osteogenic differentiation and mineralization compared to the 10 Hz treatment. As the PRF is associated with the induced strain profile, these results indicate that a sufficiently high maximum deformation in each strain cycle can crucial for the stimulation to make effects and the total number of strain cycles may not impose as much influence.

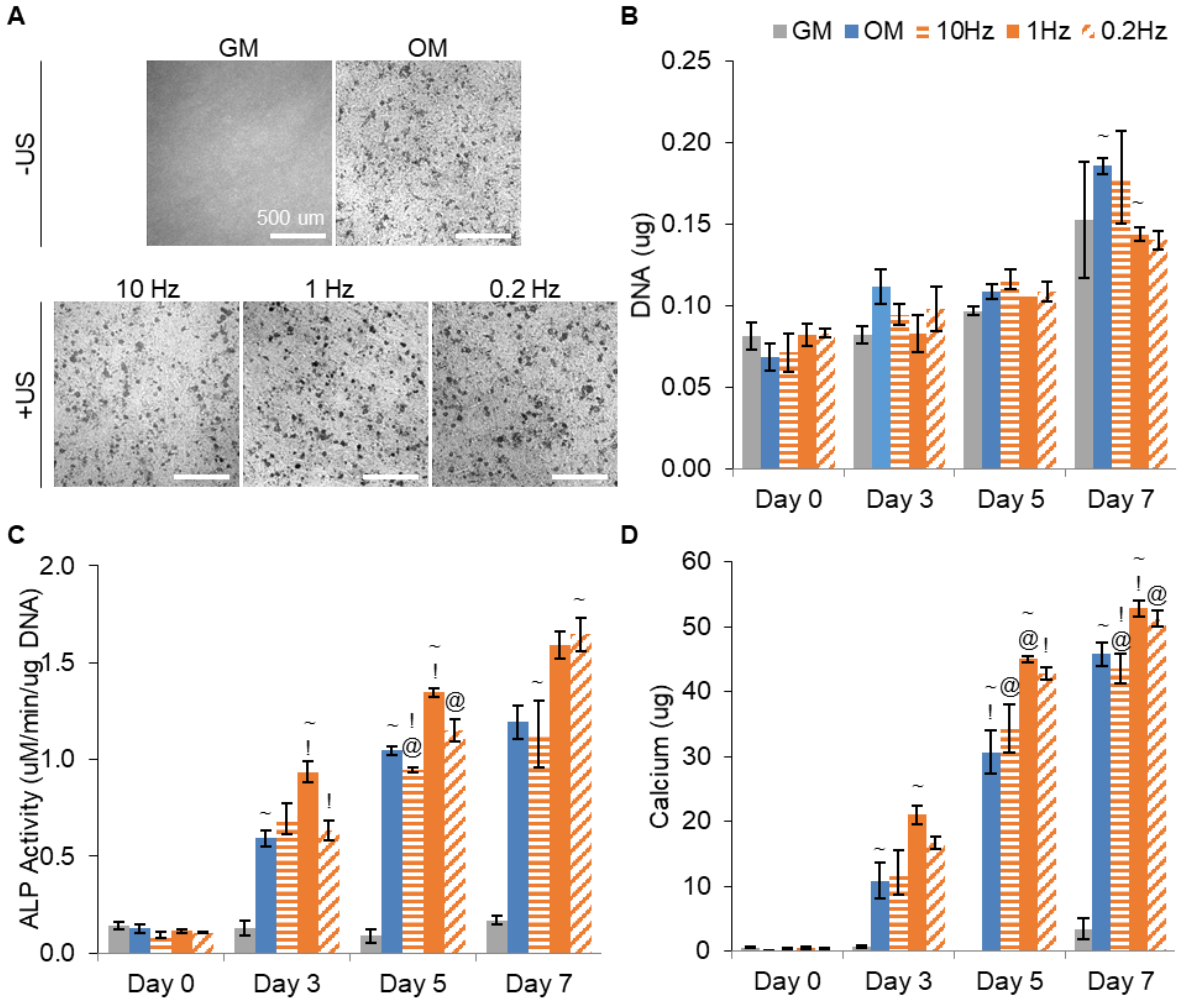

Figure 5-5. A) Bright field images, B) DNA quantification, C) ALP activity and D) calcium of cellular constructs in growth medium, osteogenic medium without ultrasound treatment and constructs exposed to ultrasound treatment with 10, 1, and 0.2 Hz PRF in osteogenic medium. N = 3. Symbols above the bars indicate significant differences ($p < 0.05$).

5.3.3 Treatment Dosage

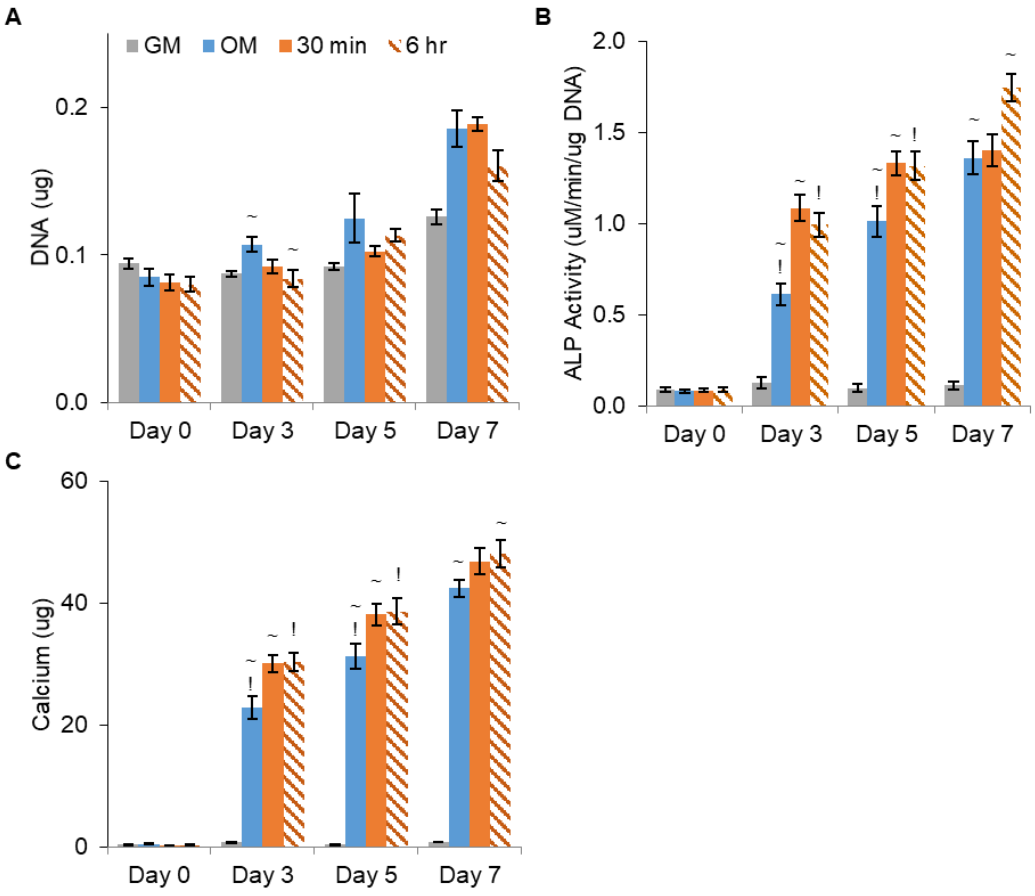

Figure 5-6. A) DNA, B) ALP activity and C) calcium of untreated cellular constructs in GM and OM and constructs in osteogenic medium exposed to ultrasound treatment for 30 min and 6 h daily. N = 3. Symbols above the bars indicate significant differences ($p < 0.05$).

We then investigated effects of ultrasound treatment dosage on osteogenesis. Cellular constructs were either treated for 30 min daily or treated for 3 h twice day (6 h total daily). The effects of stimulation was assessed with ALP activity normalized to DNA content and calcium deposition (**Figure 5-6**). DNA content was similar across different testing groups, with no significant difference between the 30 min and the 6 h group. The ultrasound treated groups, either with 30 min or 6 h daily treatment, showed significantly higher ALP activity and calcium than the untreated control group at day 3 and day 5. Samples exposed to 6 h daily treatment showed slightly

higher ALP level and calcium content than the 30 min group at day 7, but no significance was observed. These results showed that the extended treatment has a slightly more beneficial effect for enhancing osteogenic differentiation and promoting mineral deposition, yet no significant difference was found. Similar results was shown in LIPUS studies when comparing 10 and 30 min daily treatment [66]. The insensitivity to extended treatment duration may indicate a habituated response to the stimulation.

5.3.4 Osteogenic supplements

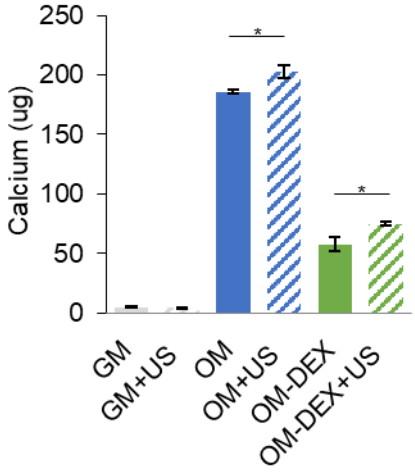

Figure 5-7. Calcium quantification of untreated and ultrasound treated cellular constructs cultured in GM, OM and OM with no DEX at day 21. N = 3. Symbols above the bars indicate significant differences ($p < 0.05$).

Chemical cues like osteogenic supplements can be strong osteogenic inductive for MSCs, but are usually not available *in vivo* [9]. We investigated the effects of ultrasound treatment with different medium conditions: GM (no osteogenic supplement), OM (with ascorbic acid, β-GP, and dexamethasone), and OM-DEX (with ascorbic acid and β-GP, no dexamethasone). Cellular constructs in three different types of medium were exposed to ultrasound stimulation for 30 min everyday till day 14, and the calcium content was assayed at day 21 (**Figure 5-7**). Ultrasound stimulation itself without any osteogenic supplements did not induce any mineral deposition in the

cellular constructs. When combined with complete supplements with or without dexamethasone, the ultrasound treatment significantly increased the calcium deposition at day 21 by 9.2% and 30.6% respectively. Even though the ultrasound treatment failed to induce osteogenic differentiation without the chemical supplements, the effect was more substantially when limited osteogenic supplements were provided.

5.3.4 Ramping Treatment Intensity

From **Figure 5-6**C, we noticed that the percentage increase in calcium induced by the ultrasound treatment was highest at day 3 (31.7%) and gradually decreased at day 5 (21.7%) and day 7 (10.4%), which indicates a progressively diminishing effect of the ultrasound treatment over time. This decrease in enhancement effects could be due to limited differentiation and mineralization potential of the constructs or the drop in effectiveness of straining over time. As cellular constructs mineralize, the cells remodel the surrounding matrix, which causes hydrogel compaction and induce changes in mechanical properties of the matrix. The change in hydrogel viscoelasticity will further change the straining level over time when constructs are exposed to a constant acoustic pressure level. As shown in **Figure 5-8**, with the progression of cell differentiation, the COL/FIB hydrogels compacted over time with an initial sample thickness around 2 mm at day 0 to under 0.5 mm at day 21. The construct volume also decreased from 278.0 ± 7.46 mm^3 to 29.8 ± 2.51 mm^3. Using the spectral ultrasound imaging analysis for assessing mineralization, there was significant increase in the acoustic concentration at day 7, 14 and 21 indicating accumulation of calcium deposits. Mechanical properties were assessed with the MUVE system, and significant decreases in maximum compliance were detected, indicating an increase in hydrogel stiffness over time. There was also a significant decrease in recovery time constant at day 21, indicating a decrease in viscosity as the cellular constructs mineralize.

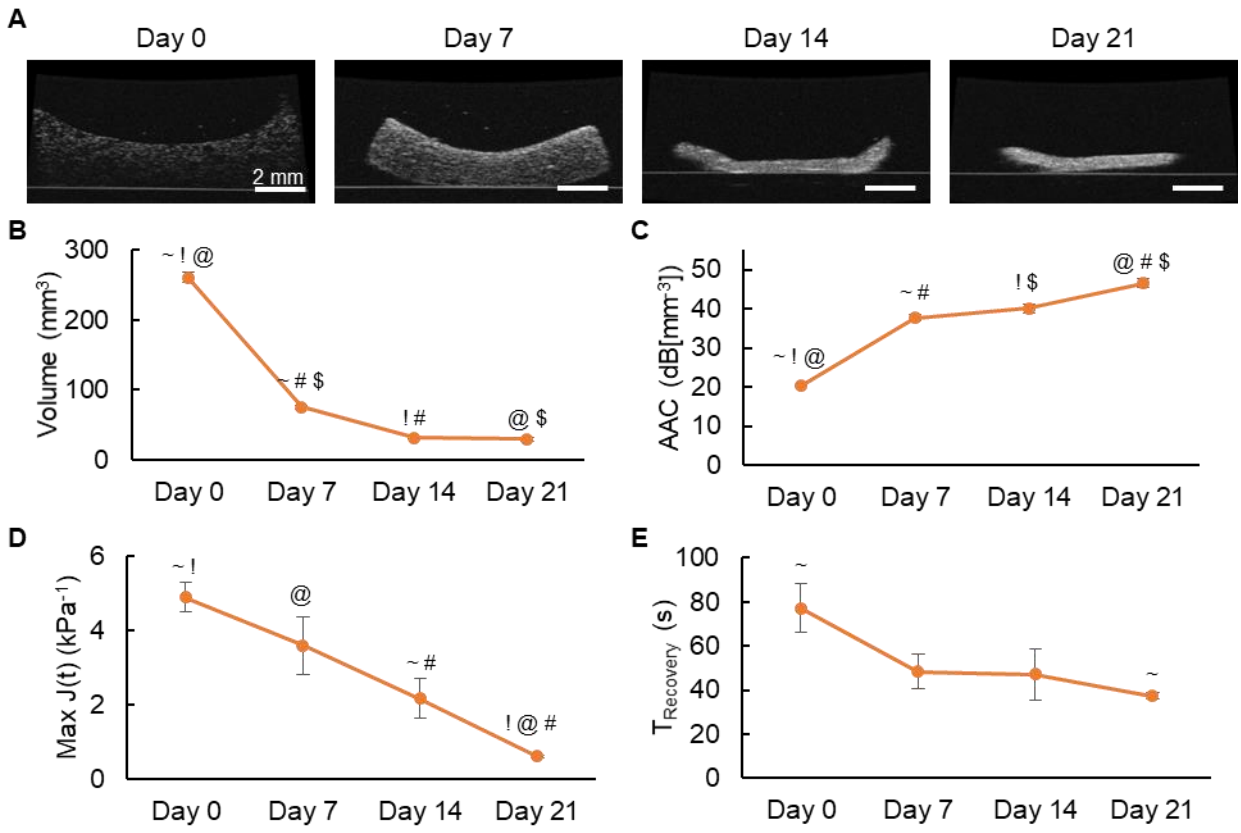

Figure 5-8. A) Grayscale ultrasound images B) Volume measured from ultrasound 3D scanning, C) average acoustic concentration (AAC) from spectral analysis, D,E) maximum compliance and recovery time constants measured with MUVE of osteogenic COL/FIB constructs at day 0, 7, 14, and 21. N = 3. Symbols above the bars indicate significant differences ($p < 0.05$).

To determine the amount of induced compression over time, strain at different acoustic pressure levels at day 0, 7 and 14 was measured. Strain-time curves at 0.60, 0.65, 0.70, 0.75 and 0.80 MPa with 1 Hz PRF at three selected time points are shown in **Figure 5-9**A. At any individual time point, the maximum strain in each cycle increased with higher acoustic pressure level. However, the acoustic pressure levels had less impact on the magnitude of maximum strain at later time points. Additionally, the day 0 constructs exhibited highest amount of residual strain due to the high fluid content in the constructs initially, which resulted in higher viscosity and therefore more unrecoverable deformation. The maximum strain in the last cycle (5^{th} cycle) of the strain measurement are shown in **Figure 5-9**B, and it shows that the maximum strain at a given acoustic pressure level decreases over time. Starting with 0.6 MPa pressure at day 0 (blue bars), to obtain

the same amount of maximum strain (yellow dashed line), an acoustic pressure level of 0.7 MPa and 0.75 MPa at day 7 (red bars) and day 14 (green bars) is required respectively. The total strain over the five cycles of straining are shown in **Figure 5-9**C. Similar to the maximum strain, the cumulative strain increase with the acoustic pressure level. To obtain the same amount of total strain, a higher acoustic pressure is needed at later time points. The cumulative strain was computed as the addition of strain magnitude in each cycle, which is the difference between the maximum strain and the resting strain at the beginning of the cycle. At day 0, the residual strain in each strain cycle were higher which gives a smaller magnitude of strain in each cycle. As **Figure 5-9**C shows, the difference in total strain between day 0 and day 14 was not as significant as in the maximum strain (**Figure 5-9**B).

To investigate the potential of further enhancing the effects of ultrasound stimulation by adaptively change the treatment intensity, four stimulation intensity schemes including constant 0.6 or 0.7 MPa pressure throughout the 14 days treatment, and incrementing the acoustic pressure level from 0.6 or 0.7 MPa at day 0 to 0.8 MPa at day 14 on a daily basis (**Figure 5-10**A). Increasing the acoustic pressure level from 0.6 to 0.8 MPa ensured the average maximum strain was above 0.39% (yellow line in **Figure 5-9**B) and an average total strain above 1.17% (yellow line in **Figure 5-9**C). On the other hand, ramping the acoustic pressure from 0.7 to 0.8 MPa would give an average total strain above 2.17% (orange line in **Figure 5-9**C), but the average maximum strain under 0.7 MPa pressure at day 0 (0.86%) would not be maintained at later time points (orange line in **Figure 5-9**B).

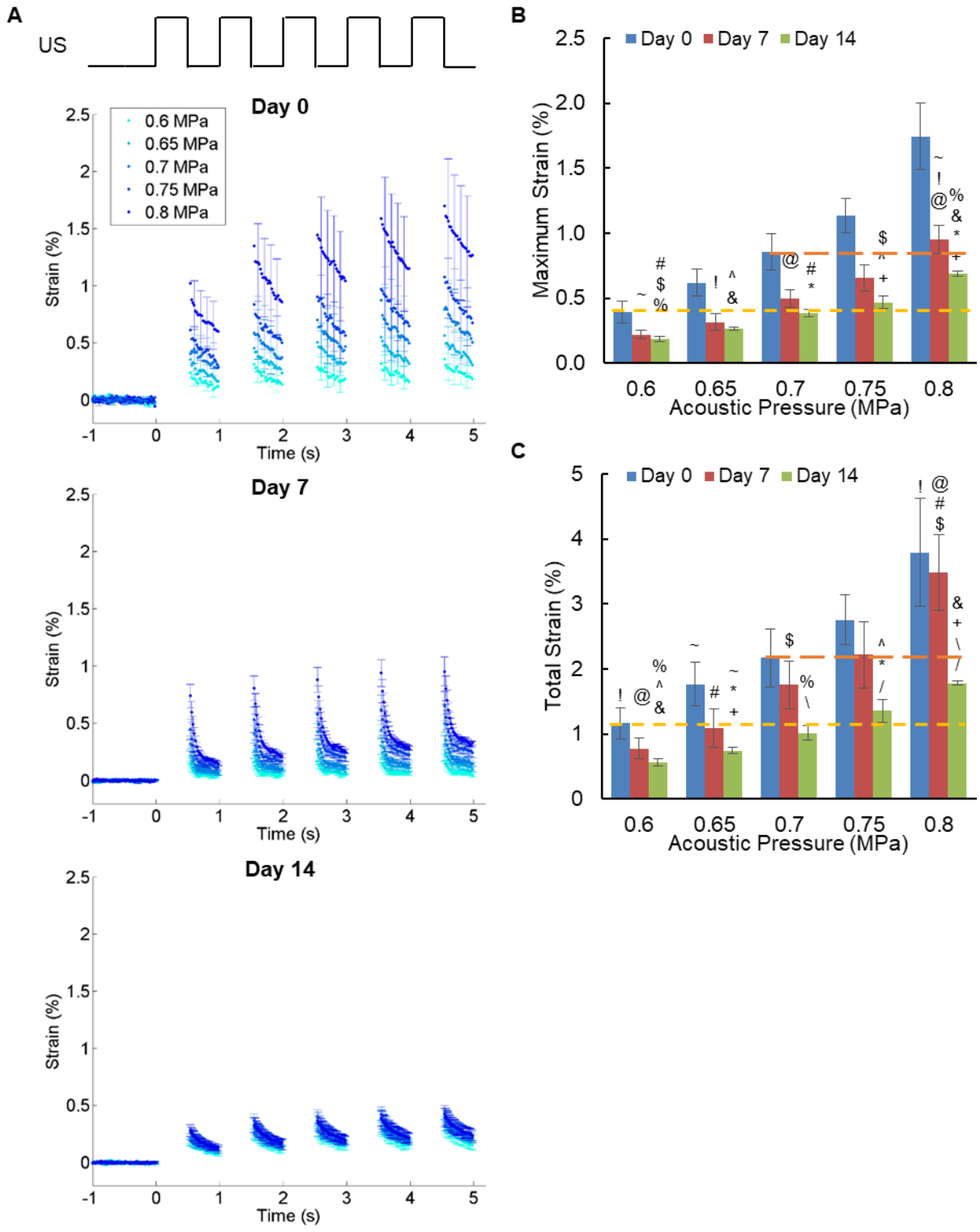

Figure 5-9. A) strain curves B) maximum strain in the last cycle and C) total strain in hydrogels when treated with 0.6, 0.65, 0.7, 0.75 and 0.8 MPa acoustic pressure at day 0, 7, and 14. N = 6. Symbols above the bars indicate significant differences ($p < 0.05$).

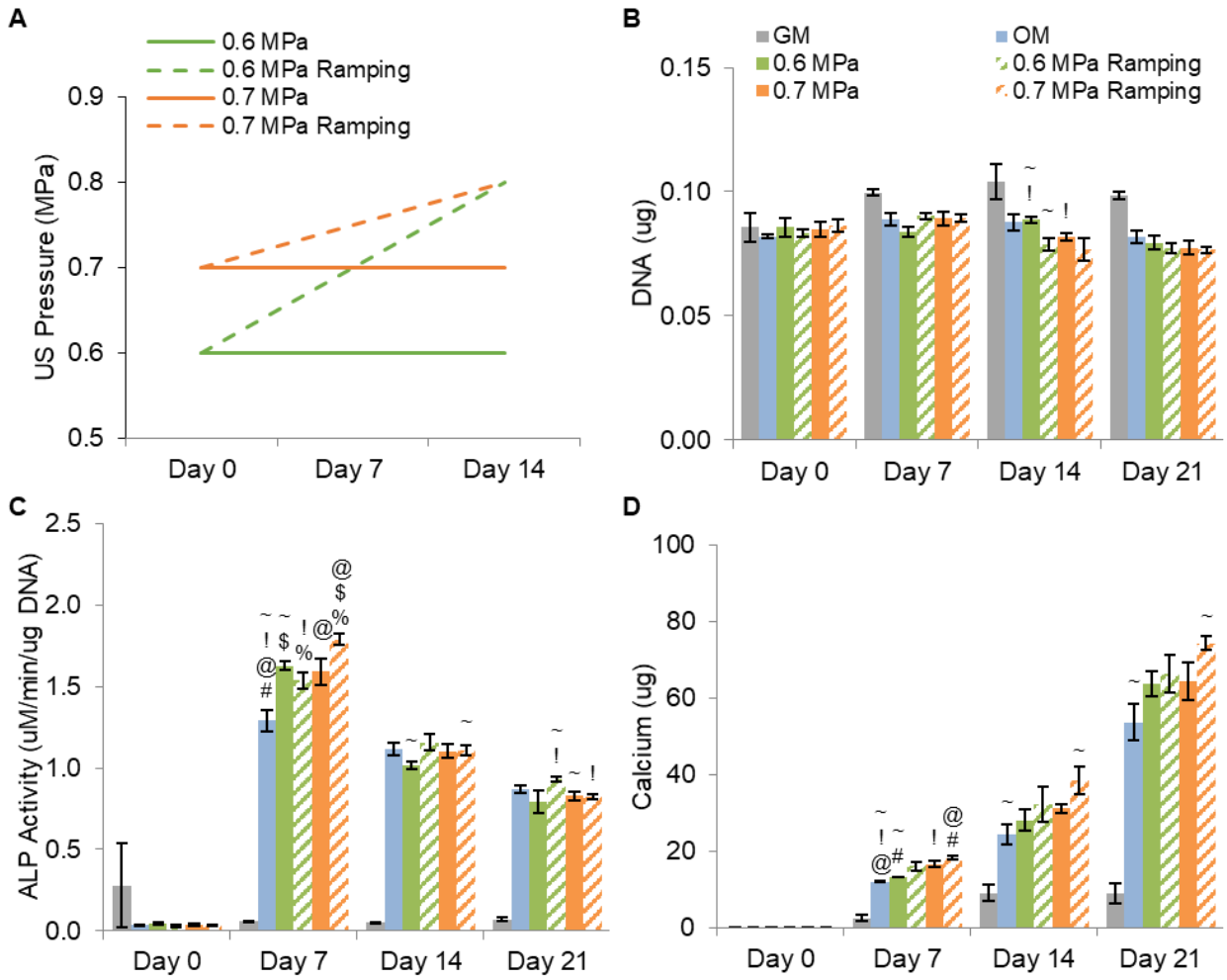

Figure 5-10. A) Acoustic pressure level of the four selected treatment scheme. B-D) quantification of DNA, ALP activity and calcium of constructs exposed to constant acoustic pressure at 0.6 and 0.7 MPa and ramping acoustic pressure from 0.6 and 0.7 MPa at day 0 to 0.8 MPa at day 14. N = 3. Symbols above the bars indicate significant differences ($p < 0.05$).

The cellular constructed were treated with the selected acoustic pressure scheme till day 14, and the DNA content, ALP activity and calcium deposition were quantified at day 0 , 7, 14, and 21 (**Figure 5-10**B to D). There was no significant difference in DNA amount across groups at day 0, 7 and 21. At day 14, the DNA amount in the 0.6 MPa group was significantly higher than that in the 0.6 MPa ramping and 0.7 MPa group. For ALP activity, all treated groups had a significantly higher expression at day 7 compared to the untreated group. The similar effects from the 0.6 MPa and the 0.7 MPa group indicate that the difference in the maximum strain at these two

pressure levels did not drastically change the cell differentiation. Both pressure levels may have reached an effective strain threshold to trigger osteogenic differentiation or the difference in the strain at these two pressures was not substantial enough to cause any difference in cell response [67, 68]. The 0.7 MPa ramping group showed significantly higher ALP activity at day 7 compared to applying constant 0.7 MPa pressure. Calcium was also found to be highest in the 0.7 MPa ramping group at day 7, 14 and 21 (38.4% increase compared to untreated), which indicates additional enhancement in promoting osteogenic differentiation and of treating the constructs with higher intensity over time to account for the change in construct mechanical properties.

5.5 Conclusion

These results show that the acoustic radiation force can be applied locally to cellular constructs in a pulsed manner to induce microscale deformation and promote osteogenic differentiation and calcium deposition. Due to the viscoelastic nature of the COL/FIB composite hydrogels, the PRF plays a critical role in determining the straining profile. Moreover, applying the stimulation dynamically over time addresses the change in the mechanical properties as the cells differentiate and remodel the matrix, and further enhanced the effects of the ultrasound treatment. This stimulation technique has the advantages of straining cellular constructs noninvasively at the cellular scale with temporal and spatial control, which gives the potential of *in vivo* applications together with our previously developed compositional [62, 63] and mechanical characterization [59] techniques to monitor and foster cell and tissue development.

5.6 References

1. Altman, G.H., et al., *Cell differentiation by mechanical stress.* Faseb Journal, 2001. **15**(14): p. 270-+.

2. Buckley, M.J., et al., *OSTEOBLASTS INCREASE THEIR RATE OF DIVISION AND ALIGN IN RESPONSE TO CYCLIC, MECHANICAL TENSION INVITRO.* Bone and Mineral, 1988. **4**(3): p. 225-236.

3. Duncan, R.L. and C.H. Turner, *MECHANOTRANSDUCTION AND THE FUNCTIONAL-RESPONSE OF BONE TO MECHANICAL STRAIN.* Calcified Tissue International, 1995. **57**(5): p. 344-358.

4. Kelly, D.J. and C.R. Jacobs, *The Role of Mechanical Signals in Regulating Chondrogenesis and Osteogenesis of Mesenchymal Stem Cells.* Birth Defects Research Part C-Embryo Today-Reviews, 2010. **90**(1): p. 75-85.

5. Minguell, J.J., A. Erices, and P. Conget, *Mesenchymal stem cells.* Experimental Biology and Medicine, 2001. **226**(6): p. 507-520.

6. Pittenger, M.F., et al., *Multilineage potential of adult human mesenchymal stem cells.* Science, 1999. **284**(5411): p. 143-147.

7. Qiu, W.M., et al., *Patients with high bone mass phenotype exhibit enhanced osteoblast differentiation and inhibition of adipogenesis of human mesenchymal stem cells.* Journal of Bone and Mineral Research, 2007. **22**(11): p. 1720-1731.

8. Verma, S., et al., *Adipocytic proportion of bone marrow is inversely related to bone formation in osteoporosis.* Journal of Clinical Pathology, 2002. **55**(9): p. 693-698.

9. Haasper, C., et al., *Osteogenic Differentiation of Human Bone Marrow Stromal Cells (hBMSC) by Cyclic Longitudinal Mechanical Strain and Dexamethasone.* Zeitschrift Fur Orthopadie Und Unfallchirurgie, 2008. **146**(5): p. 636-643.

10. Hamilton, D.W., T.M. Maul, and D.A. Vorp, *Characterization of the response of bone marrow derived progenitor cells to cyclic strain: Implications for vascular tissue engineering applications (vol 10, pg 361, 2004).* Tissue Engineering Part A, 2008. **14**(3): p. 461-461.

11. Kearney, E.M., et al., *Tensile Strain as a Regulator of Mesenchymal Stem Cell Osteogenesis.* Annals of Biomedical Engineering, 2010. **38**(5): p. 1767-1779.

12. Lee, I.C., et al., *The differentiation of mesenchymal stem cells by mechanical stress or/and co-culture system.* Biochemical and Biophysical Research Communications, 2007. **352**(1): p. 147-152.

13. Maredziak, M., et al., *The Effect of Low-Magnitude Low-Frequency Vibrations (LMLF) on Osteogenic Differentiation Potential of Human Adipose Derived Mesenchymal Stem Cells.* Cellular and Molecular Bioengineering, 2017. **10**(6): p. 549-562.

14. Pelaez, D., C.Y.C. Huang, and H.S. Cheung, *Cyclic Compression Maintains Viability and Induces Chondrogenesis of Human Mesenchymal Stem Cells in Fibrin Gel Scaffolds.* Stem Cells and Development, 2009. **18**(1): p. 93-102.

15. Li, Y.J., et al., *Oscillatory fluid flow affects human marrow stromal cell proliferation and differentiation.* Journal of Orthopaedic Research, 2004. **22**(6): p. 1283-1289.

16. Qi, M.C., et al., *Expression of Bone-related Genes in Bone Marrow MSCs after Cyclic Mechanical Strain: Implications for Distraction Osteogenesis.* International Journal of Oral Science, 2009. **1**(3): p. 143-150.

17. Sumanasinghe, R.D., S.H. Bernacki, and E.G. Loboa, *Osteogenic differentiation of human mesenchymal stem cells in collagen matrices: Effect of uniaxial cyclic tensile strain on bone morphogenetic protein (BMP-2) mRNA expression.* Tissue Engineering, 2006. **12**(12): p. 3459-3465.

18. Plotkin, L.I., et al., *Mechanical stimulation prevents osteocyte apoptosis: requirement of integrins, Src kinases, and ERKs.* American Journal of Physiology-Cell Physiology, 2005. **289**(3): p. C633-C643.

19. Wang, S.J., et al., *LOW-INTENSITY ULTRASOUND TREATMENT INCREASES STRENGTH IN A RAT FEMORAL FRACTURE MODEL.* Journal of Orthopaedic Research, 1994. **12**(1): p. 40-47.

20. Azuma, Y., et al., *Low-intensity pulsed ultrasound accelerates rat femoral fracture healing by acting on the various cellular reactions in the fracture callus.* Journal of Bone and Mineral Research, 2001. **16**(4): p. 671-680.

21. Brookes, M. and M. Dyson, *STIMULATION OF BONE REPAIR BY ULTRASOUND.* Journal of Bone and Joint Surgery-British Volume, 1983. **65**(5): p. 659-659.

22. Jung, Y.J., et al., *FOCUSED LOW-INTENSITY PULSED ULTRASOUND ENHANCES BONE REGENERATION IN RAT CALVARIAL BONE DEFECT THROUGH ENHANCEMENT OF CELL PROLIFERATION.* Ultrasound in Medicine and Biology, 2015. **41**(4): p. 999-1007.

23. Romano, C.L., D. Romano, and N. Logoluso, *LOW-INTENSITY PULSED ULTRASOUND FOR THE TREATMENT OF BONE DELAYED UNION OR NONUNION: A REVIEW.* Ultrasound in Medicine and Biology, 2009. **35**(4): p. 529-536.

24. Nolte, P.A., et al., *Low-intensity pulsed ultrasound in the treatment of nonunions.* Journal of Trauma-Injury Infection and Critical Care, 2001. **51**(4): p. 693-702.

25. Takikawa, S., et al., *Low-intensity pulsed ultrasound initiates bone healing in rat nonunion fracture model.* Journal of Ultrasound in Medicine, 2001. **20**(3): p. 197-205.

26. Chen, S.H., et al., *Effect of low intensity ultrasounds on the growth of osteoblasts*, in *2007 Annual International Conference of the Ieee Engineering in Medicine and Biology Society, Vols 1-16*. 2007. p. 5834-5837.

27. Tassinary, J.A.F., et al., *Therapeutic Ultrasound Stimulates MC3T3-E1 Cell Proliferation Through the Activation of NF-kappa B1, p38 alpha, and mTOR.* Lasers in Surgery and Medicine, 2015. **47**(9): p. 765-772.

28. Veronick, J., et al., *The effect of acoustic radiation force on osteoblasts in cell/hydrogel constructs for bone repair*. Experimental Biology and Medicine, 2016. **241**(10): p. 1149-1156.

29. Costa, V., et al., *Osteogenic commitment and differentiation of human mesenchymal stem cells by low-intensity pulsed ultrasound stimulation.* Journal of Cellular Physiology, 2018. **233**(2): p. 1558-1573.

30. Jaiswal, N., et al., *Osteogenic differentiation of purified, culture-expanded human mesenchymal stem cells in vitro.* Journal of Cellular Biochemistry, 1997. **64**(2): p. 295-312.

31. Uddin, S.M.Z. and Y.X. Qin, *Enhancement of Osteogenic Differentiation and Proliferation in Human Mesenchymal Stem Cells by a Modified Low Intensity Ultrasound Stimulation under Simulated Microgravity.* Plos One, 2013. **8**(9).

32. Zhou, X., et al., *Improved Human Bone Marrow Mesenchymal Stem Cell Osteogenesis in 3D Bioprinted Tissue Scaffolds with Low Intensity Pulsed Ultrasound Stimulation.* Scientific Reports, 2016. **6**.

33. Park, K., et al., *Therapeutic ultrasound effects on interleukin-1 beta stimulated cartilage construct in vitro.* Ultrasound in Medicine and Biology, 2007. **33**(2): p. 286-295.

34. Sun, J.S., et al., *In vitro effects of low-intensity ultrasound stimulation on the bone cells.* Journal of Biomedical Materials Research, 2001. **57**(3): p. 449-456.

35. Yang, R.S., et al., *Regulation by ultrasound treatment on the integrin expression and differentiation of osteoblasts.* Bone, 2005. **36**(2): p. 276-283.

36. Hsu, H.C., et al., *Ultrasound induces cyclooxygenase-2 expression through integrin, integrin-linked kinase, Akt, NF-kappa B and p300 pathway in human chondrocytes.* Cellular Signalling, 2007. **19**(11): p. 2317-2328.

37. Iwashina, T., et al., *Low-intensity pulsed ultrasound stimulates cell proliferation and proteoglycan production in rabbit intervertebral disc cells cultured in alginate.* Biomaterials, 2006. **27**(3): p. 354-361.

38. Jones, D.B., et al., *BIOCHEMICAL SIGNAL TRANSDUCTION OF MECHANICAL STRAIN IN OSTEOBLAST-LIKE CELLS.* Biomaterials, 1991. **12**(2): p. 101-110.

39. Liu, S.L., et al., *Investigation into the Effect of Acoustic Radiation Force and Acoustic Streaming on Particle Patterning in Acoustic Standing Wave Fields.* Sensors, 2017. **17**(7).

40. Simmons, C.A., et al., *Cyclic strain enhances matrix mineralization by adult human mesenchymal stem cells via the extracellular signal-regulated kinase (ERK1/2) signaling pathway.* Journal of Biomechanics, 2003. **36**(8): p. 1087-1096.

41. Arnsdorf, E.J., et al., *Mechanically induced osteogenic differentiation - the role of RhoA, ROCKII and cytoskeletal dynamics.* Journal of Cell Science, 2009. **122**(4): p. 546-553.

42. Baker, K.G., V.J. Robertson, and F.A. Duck, *A review of therapeutic ultrasound: Biophysical effects.* Physical Therapy, 2001. **81**(7): p. 1351-1358.

43. Hiyama, A., et al., *Synergistic effect of low-intensity pulsed ultrasound on growth factor stimulation of nucleus pulposus cells.* Journal of Orthopaedic Research, 2007. **25**(12): p. 1574-1581.

44. Puts, R., et al., *In-vitro Stimulation of Cells of the Musculoskeletal System with Focused Low-Intensity Pulsed Ultrasound (FLIPUS): Analyses of Cellular Activities in Response to the Optimized Acoustic Dose*, in *2014 Ieee International Ultrasonics Symposium*. 2014. p. 1630-1633.

45. Binderman, I., Z. Shimshoni, and D. Somjen, *BIOCHEMICAL PATHWAYS INVOLVED IN THE TRANSLATION OF PHYSICAL STIMULUS INTO BIOLOGICAL MESSAGE.* Calcified Tissue International, 1984. **36**: p. S82-S85.

46. Somjen, D., et al., *BONE REMODELING INDUCED BY PHYSICAL STRESS IS PROSTAGLANDIN-E2 MEDIATED.* Biochimica Et Biophysica Acta, 1980. **627**(1): p. 91-100.

47. Takeuchi, R., et al., *Low-intensity pulsed ultrasound activates the phosphatidylinositol 3 kinase/Akt pathway and stimulates the growth of chondrocytes in three-dimensional cultures: a basic science study.* Arthritis Research & Therapy, 2008. **10**(4).

48. Zhang, P., et al., *Osteogenic response of mesenchymal stem cells to continuous mechanical strain is dependent on ERK1/2-Runx2 signaling.* International Journal of Molecular Medicine, 2012. **29**(6): p. 1083-1089.

49. Angle, S.R., et al., *Osteogenic differentiation of rat bone marrow stromal cells by various intensities of low-intensity pulsed ultrasound.* Ultrasonics, 2011. **51**(3): p. 281-288.

50. Becerra, G.D., et al., *Evaluation of mesenchymal stem cell proliferation using different low intensity pulsed ultrasound intensities.* International Journal of Morphology, 2012. **30**(2): p. 621-626.

51. Kusuyama, J., et al., *Low Intensity Pulsed Ultrasound (LIPUS) Influences the Multilineage Differentiation of Mesenchymal Stem and Progenitor Cell Lines through ROCK-Cot/Tpl2-MEK-ERK Signaling Pathway.* Journal of Biological Chemistry, 2014. **289**(15): p. 10330-10344.

52. Freitas, L.S., et al., *Effect of therapeutic pulsed ultrasound on parameters of oxidative stress in skeletal muscle after injury*. Cell Biology International, 2007. **31**(5): p. 482-488.

53. Fu, S.C., et al., *Low-intensity pulsed ultrasound on tendon healing - A study of the effect of treatment duration and treatment initiation.* American Journal of Sports Medicine, 2008. **36**(9): p. 1742-1749.

54. Kristiansen, T.K., et al., *Accelerated healing of distal radial fractures with the use of specific, low-intensity ultrasound - A multicenter, prospective, randomized, double-blind, placebo-controlled study*. Journal of Bone and Joint Surgery-American Volume, 1997. **79A**(7): p. 961-973.

55. Monden, K., et al., *Effect of Low-intensity Pulsed Ultrasound (LIPUS) with Different Frequency on Bone Defect Healing.* Journal of Hard Tissue Biology, 2015. **24**(2): p. 189-197.

56. Hu, J.Z., et al., *Combined Application of Low-Intensity Pulsed Ultrasound and Functional Electrical Stimulation Accelerates Bone-Tendon Junction Healing in a Rabbit Model.* Journal of Orthopaedic Research, 2014. **32**(2): p. 204-209.

57. Kang, K.S., et al., *Effects of combined mechanical stimulation on the proliferation and differentiation of pre-osteoblasts.* Experimental and Molecular Medicine, 2011. **43**(6): p. 367-373.

58. Konofagou, E.E. and K. Hynynen, *Localized harmonic motion imaging: Theory, simulations and experiments*, in *2002 Ieee Ultrasonics Symposium Proceedings, Vols 1 and 2*, D.E. Yuhas and S.C. Schneider, Editors. 2002. p. 1895-1898.

59. Hong, X.W., J.P. Stegemann, and C.X. Deng, *Microscale characterization of the viscoelastic properties of hydrogel biomaterials using dual-mode ultrasound elastography.* Biomaterials, 2016. **88**: p. 12-24.

60. Rao, R.R., et al., *Matrix composition regulates three-dimensional network formation by endothelial cells and mesenchymal stem cells in collagen/fibrin materials.* Angiogenesis, 2012. **15**(2): p. 253-264.

61. Wang, L.M. and J.P. Stegemann, *Thermogelling chitosan and collagen composite hydrogels initiated with beta-glycerophosphate for bone tissue engineering.* Biomaterials, 2010. **31**(14): p. 3976-3985.

62. Gudur, M., et al., *Noninvasive, Quantitative, Spatiotemporal Characterization of Mineralization in Three-Dimensional Collagen Hydrogels Using High-Resolution Spectral Ultrasound Imaging.* Tissue Engineering Part C-Methods, 2012. **18**(12): p. 935-946.

63. Gudur, M.S.R., et al., *Noninvasive Quantification of In Vitro Osteoblastic Differentiation in 3D Engineered Tissue Constructs Using Spectral Ultrasound Imaging.* Plos One, 2014. **9**(1).

64. Hong, X., J.P. Stegemann, and C.X. Deng, *Microscale characterization of the viscoelastic properties of hydrogel biomaterials using dual-mode ultrasound elastography.* Biomaterials, 2016. **88**: p. 12-24.

65. Cummings, C.L., et al., *Properties of engineered vascular constructs made from collagen, fibrin, and collagen-fibrin mixtures.* Biomaterials, 2004. **25**(17): p. 3699-3706.

66. Katiyar, A., R.L. Duncan, and K. Sarkar, *Ultrasound stimulation increases proliferation of MC3T3-E1 preosteoblast-like cells.* Journal of therapeutic ultrasound, 2014. **2**: p. 1.

67. Tang, L., Z. Lin, and Y.M. Li, *Effects of different magnitudes of mechanical strain on Osteoblasts in vitro.* Biochemical and Biophysical Research Communications, 2006. **344**(1): p. 122-128.

68. Wang, J.H.C. and E.S. Grood, *The strain magnitude and contact guidance determine orientation response of fibroblasts to cyclic substrate strains.* Connective Tissue Research, 2000. **41**(1): p. 29-36.

Chapter 6 Summary, Conclusions and Future Directions

The central role of mechanobiology in tissue development and regeneration creates a need for tools to study the influence of both static and dynamic mechanical stimuli on developing tissue over time [1, 2]. Conventional mechanical characterization and stimulation methods that rely on contact surface force usually require special sample preparation, involve sample destruction, and have limited potential for *in vivo* applications. Ultrasound-based methods, on the other hand, utilizes acoustic radiation force that penetrate into the sample without contact and haven been applied for noninvasive imaging of tissue elasticity [3, 4]. However, their application for quantitative assessment of material properties, especially viscoelastic properties of soft materials with high water content, has not been exploited. For stimulating tissue development, low-intensity pulsed ultrasound has been widely used [5-7], yet the underlying mechanism of the method has remained unclear and no consensus in optimal parameters for directing stem cell differentiation has been reached.

6.1 Multimode Ultrasound Viscoelastography (MUVE)

Summary and Conclusion

We have developed a multimode ultrasound viscoelastography (MUVE) system to assess mechanical properties of engineered tissue constructs [8]. MUVE consists of a 2 MHz focused ultrasound (FUS) transducer to apply steady acoustic radiation force (ARF) to deform the sample, and a 10 MHz imaging transducer to monitor the deformation concurrently. We used MUVE to perform creep tests on hydroxyapatite (HA) – doped agarose, collagen and fibrin hydrogels of

selected concentrations, as well as cell-seeded collagen hydrogels at selected time points. MUVE maps the deformation and strain in the samples. We obtained quantitative local and bulk viscoelastic properties of the samples by fitting the strain-time curves at defined depth in the sample to relevant constitutive models. Results clearly showed differences between materials, concentrations and culture time.

We then further investigated MUVE's capability for measuring localized mechanical properties in three dimensions (3D). Dense agarose microbeads were embedded into agarose, collagen and fibrin hydrogels to form multiphase constructs. MUVE was used to map heterogeneities in these constructs and it clearly showed the distinctive viscoelastic behavior from the agarose microbead and its surrounding hydrogel. By varying the size of the agarose microbeads, we determined the MUVE system to have a spatial resolution of approximately 200 μm in both lateral and axial directions. The system can detect a 0.2 kPa difference between the agarose microbead inclusions and the surrounding agarose hydrogel. Comparison of MUVE, nanoindentation, and shear rheometry on testing agarose and fibrin hydrogels showed that MUVE generated more consistent results at the microscale especially for very soft materials.

Compare to other mechanical testing methods, since MUVE does not require a contact surface for applying stress, it does not impose as much restrictions in sample geometry and dimensions. This feature is extremely advantageous and critical when testing soft materials with high water content as establishing solid contact when deforming and avoiding sticking phenomenon during retraction while keeping samples hydrated can be quite challenging for these samples. In addition, the parameters we used with the MUVE system generated 5 – 50 μm deformation, which is on the cell scale and cannot easily be achieved and measured by other methods. Mechanical characterization at this scale can provide unique insights into matrix

mechanics and cell-matrix interaction. Moreover, MUVE applies acoustic radiation force to deform the sample with ultrasound imaging to monitor deformation, which enables mapping the viscoelastic properties in three dimensions and allows noninvasive testing. The system can be applied to detect heterogeneities and monitor tissue development longitudinally both *in vitro* and *in vivo*.

Future Directions

The MUVE system is quite versatile. It can be easily modified to test a variety of materials with various mechanical testing modes. One feature that can improve the system performance is to enable real-time deformation measurement and display. The system now acquires and stores the radiofrequency (RF) signals in the oscilloscope and data need to be exported and then processed to generate strain-time curve. To accomplish real-time strain measurement, we can feed the segmented RF data from the oscilloscope to the computer, and process the data as we perform the mechanical test. With the capability to provide real-time strain measurement, we can 1) quickly perform trial test and easily adjust the load function for the specific sample being tested; 2) abort test when unexpected large deformation is generated to ensure sample integrity and 3) develop strain-controlled testing mode like stress relaxation test. In addition to exploring strain-controlled testing modes, we can also manipulate the FUS pulses to perform stress-train test by ramping the acoustic pressure, and perform dynamic mechanical analysis by modulating the acoustic pressure with sinusoidal wave. These mechanical testing modes can help provide information of the material behavior under various types of load and make results from MUVE more comparable to other methods.

6.2 Focused Pulsed Acoustic Compression

Summary and Conclusion

We have adapted the MUVE system to implement a mechanical stimulation regimen for engineered tissue constructs based on localized microscale cyclic compressive strain using acoustic radiation force. A treatment system was built with custom designed parts to provide sterile environment for the cellular constructs and the FUS transducer was mounted on the 3D motorized stage to scan the whole constructs. We investigated the effect of pulse repetition frequency (PRF), acoustic intensity, and treatment dosage on osteogenesis and mineralization in collagen/fibrin (COL/FIB) hydrogels seeded with human mesenchymal stem cells (hMSCs) based on cell viability, DNA content, alkaline phosphatase (ALP) activity and calcium deposition. The COL/FIB hydrogels exhibit time-dependent strain behavior due to the viscoelastic properties, and the PRF can affect the number of strain cycles delivered within a given time frame and the magnitude of peak strain and residual strain. Among 10, 1.0 and 0.2 Hz PRF, the 1.0 Hz PRF yielded the highest ALP activity at day 3 and day 5, and a 15% increase in calcium deposition at day 7 compared to the untreated sham. No significant difference was found when treating the cellular constructs for 30 min versus 6 h per day. We observed that the cellular constructs changed in volume, composition and mechanical properties over time, and we adapted the treatment regimen to these changes by increasing the treatment intensity over time. By ramping the intensity over time, the treatment induced a 35% increase in mineralization at day 21 compared to the sham. In a separate study, we also investigated the effect of mechanical stimulation in combination with biochemical stimulation. The mechanical treatment did not induce osteogenesis with the absence of osteogenesis-inductive supplements. The effect of the mechanical treatment was also found to be more substantial when cellular constructs were cultured without dexamethasone.

This ARF-based mechanical stimulation present here utilizes ARF to induce measurable localized cyclic microscale deformation in the cellular constructs, which distinguishes it from the more widely used low-intensity pulsed ultrasound (LIPUS) treatment. We have optimized the parameters to initiate the osteogenesis and mineralization process earlier and achieved higher mineral deposition in the cellular construct. This technique again can be applied noninvasively, which contributes to its potential to provide mechanical intervention in engineered tissue at selected time points before and after implantation. Moreover, with the guidance of ultrasound imaging, the engineered tissue can be easily identified in the animal / patient and the cyclic strain can be applied locally to the site of interest. In addition, by using focused ultrasound transducer with different center frequency or focal distance, the technique can be applied to engineered tissue or native tissue with various thickness and at different depth. All these attributes give the technique the tenability to better mimic the native mechanical environment for the cells and tissue to develop in various applications.

Future Directions

Modulate the Treatment Regimen Dynamically

In our studies, we have found that dynamically adapting the stimulation regimen to state of the engineered tissue can have a significant impact. We also showed that focused pulsed acoustic strain can induce an increase in ALP and mineralization at as early as day 3, and the enhancing effect gradually diminishes over time when using a constant intensity. Studies using LIPUS [9, 10] found that the effects on ALP becomes significant around day 7 and day 14 for mineralization. These differences in the effective timing may suggest that the two treatment regimens act on the cellular constructs differently, as the cyclic acoustic strain has a stronger impact on the initiation of osteogenesis and mineralization while LIPUS promotes the matrix

deposition at a later stage. The effects of LIPUS treatment on fracture healing is believed to be associated with the pressure and strain gradient at the fracture site which depends on the attenuation of in the tissue [11-13]. This mechanism would explain the more effective enhancement in calcium deposition using LIPUS as the matrix deposition especially the mineral nodules contribute significantly to the attenuation in the engineered constructs which helps build the pressure gradient in the tissue. Understanding the difference in the underlying mechanism, it would be worthwhile to investigate the stimulation effects when combining the two treatment regimen or transitioning from one to another over time.

Synergistic Effects of Mechanical and Biochemical Cues

Even though studies have shown that mechanical stimuli alone can affect cell differentiation [14-16], biochemical cues are also crucial in cell fate determination. The results from our studies showed that the acoustic strain alone cannot direct mesenchymal stem cells into osteogenic lineage without the chemical cues. In addition, the treatment outcome was affected by the chemical stimulants provided. A potential next step would be to further explore the effects of combining biochemical and mechanical stimulation and investigate the interactions between the two factors. First, we can look into optimizing the stimulation regimen in a biochemical environment similar to that the engineered tissue will be exposed to after implantation, which would help us better design the treatment for *in vivo* applications. Another direction would be to investigate the optimal combination of biochemical cues and mechanical stimulation for desired differentiation direction. These studies will lead to more comprehensive understanding of the interactions between various factors in cell differentiation and tissue development. The knowledge from these studies can be applied to either more effectively pre-differentiate the cells before

implantation or to promote the cell differentiation and development *in situ* combining ultrasound mechanical stimulation with growth factor delivery.

Directing MSC Differentiation Lineage and Generating Multiphase Tissues

Mesenchymal stem cells have the potential to differentiate into multiple lineages. Studies have shown that MSCs can simultaneously differentiate to a mixture of cell phenotypes including both osteoblast and chondrocyte, and mechanical stimulation can be tailored to change the phenotype composition in the scaffold [17, 18]. The magnitude, frequency and treatment dosage are determining factors in controlling the treatment outcome. One of the future applications for the acoustic strain treatment is to direct stem cell differentiation in to specific lineages by manipulating the treatment parameters. Moreover, we have demonstrated that the technique allows localized application of acoustic radiation force and the stimulation can be delivered differently within the constructs, which is not achievable using bulk mechanical loading methods. The localized application of mechanical loading can potentially facilitate in the construction of cellular constructs with multiple tissue types and establishing the tissue interface, which is still challenging in tissue engineering. Future studies can be carried out to investigate effects of mechanical loading gradient in cell migration, cell differentiation and matrix deposition. The results of these studies can be used to develop an advanced treatment method that better mimics the natural mechanical loading environment at a multi-tissue interface, such as an osteochondral interface, for more effective defect repair and tissue function restoration.

6.3 Application of Spectral Ultrasound Imaging (SUSI) *in vivo*

Summary and Conclusion

This dissertation also presented our work of applying the previously developed spectral ultrasound imaging (SUSI) technique in an animal model for detecting heterotopic ossification. We used SUSI, micro computed tomography (μCT), and histology at 1, 2, 4, and 9 weeks post-injury to follow the progression of HO in the mice after an Achilles tenotomy and 30% total body surface area burn. Acoustic concentration and acoustic scatterer size derived from SUSI analysis distinguished the tissue from the burn/tenotomy mice model from the incision-only control mice. Using SUSI, HO was visualized as early as 1 week after injury while μCT did not detect mineralization by 4 weeks after injury. In addition, spectroscopic foci of HO present at 1 week that persisted throughout all time points correlated with the HO present at 9 weeks on micro CT imaging and histology.

This work showed our attempt and success of applying SUSI in an animal model to monitor mineralizing tissue over time. With the sensitivity of ultrasound imaging and SUSI analysis for detecting mineralizing tissue, HO foci can be detected as early as one week after the injury. The early diagnosis allows timely decision making based on quantitative metrics for pharmaceutical treatments, which can help avoid the potential side effects when administering medications to patients with injury but not developing HO, and negate the need of surgical intervention when HO progresses to a more matured stage. The study also demonstrated the potential of adapting MUVE and the acoustic strain system for in vivo applications.

Future Directions

Heterotopic ossification is often associated with high vascularization and tissue stiffening [19]. To allow even earlier and more reliable detection of HO, we can use contrast imaging with targeted microbubbles for detecting associated immune response and vessel formation. Moreover,

the MUVE system can be used to pinpoint localized mechanical properties at the sites with high risk of developing HO to assist in decision making process for medical intervention.

6.4 Thesis Conclusion and Outlook

This dissertation showcased our work on developing and applying novel ultrasound-based techniques for mechanical and compositional characterization as well as mechanical stimulation, and demonstrated their potentials for mechanobiology studies and other tissue engineering applications. Results have shown that with these techniques, we can obtain quantitative viscoelastic mechanical properties of soft materials and map heterogeneity in multiphase constructs. We can also noninvasively monitor the compositional and mechanical properties concurrently during tissue development. Pulsed acoustic radiation force can be applied to induce cyclic strain in engineered tissues to promote stem cell differentiation towards osteogenesis and accelerate mineralizing tissue maturation.

A future goal is to develop an integrated multimode ultrasound system combining MUVE, SUSI and ultrasound stimulation, and advances based on the current system can be made towards this future goal to combine SUSI and MUVE and to improve the mechanical loading system. The imaging transducer can be moved using the motorized stage with a small step size to mimic the motion of the imaging probe on the VEVO system and obtain 3D volumetric information of the sample. We can apply SUSI analysis with the RF data acquired with the imaging transducer in the MUVE system to characterize the sample composition. For the mechanical characterization, a slightly larger step size can be used when scanning across the sample since the mechanical testing is more time consuming. The mechanical testing results can be mapped onto the 3D volumetric imaging and be correlated with the SUSI analysis results for studying the structure-function correlations. For the mechanical stimulation, to more effectively treat large amount of cellular

constructs, we can combine multiple small-dimension focused ultrasound transducers into a 2D array and simultaneously power the transducers to treat multiple cellular construct. The transducer array can be connected to a linear actuator for scanning the sample. Future work may be needed to combine all three techniques, SUSI, MUVE and mechanical stimulation, into a compacted system when it becomes cost-effective.

This integrated system will help tremendously in advancing tissue engineering approaches by providing tools for better quality control, longitudinal monitoring of tissue development, and mechanically stimulating tissues for optimal outcomes. It can also be used in mechanobiology studies and provide unique insights into the roles of matrix composition, static mechanical environment, and dynamic mechanical stimuli.

6.5 References

1. Guilak, F., et al., *Biomechanics and mechanobiology in functional tissue engineering.* Journal of Biomechanics, 2014. **47**(9): p. 1933-1940.
2. Hao, J., et al., *Mechanobiology of mesenchymal stem cells: Perspective into mechanical induction of MSC fate.* Acta Biomaterialia, 2015. **20**: p. 1-9.
3. Nightingale, K., et al., *Acoustic radiation force impulse imaging: In vivo demonstration of clinical feasibility.* Ultrasound Med. Biol., 2002. **28**(2): p. 227-235.
4. Greenleaf, J.F., M. Fatemi, and M. Insana, *Selected methods for imaging elastic properties of biological tissues.* Annu. Rev. Biomed. Eng., 2003. **5**: p. 57-78.
5. Carina, V., et al., *Effect of low-intensity pulsed ultrasound on osteogenic human mesenchymal stem cells commitment in a new bone scaffold.* Journal of Applied Biomaterials & Functional Materials, 2017. **15**(3): p. E215-E222.
6. Raza, H., et al., *Effect of Low-Intensity Pulsed Ultrasound on Distraction Osteogenesis Treatment Time A Meta-analysis of Randomized Clinical Trials.* Journal of Ultrasound in Medicine, 2016. **35**(2): p. 349-358.
7. Zhou, X., et al., *Improved Human Bone Marrow Mesenchymal Stem Cell Osteogenesis in 3D Bioprinted Tissue Scaffolds with Low Intensity Pulsed Ultrasound Stimulation.* Scientific Reports, 2016. **6**.

8. Hong, X., J.P. Stegemann, and C.X. Deng, *Microscale characterization of the viscoelastic properties of hydrogel biomaterials using dual-mode ultrasound elastography.* Biomaterials, 2016. **88**: p. 12-24.

9. Angle, S.R., et al., *Osteogenic differentiation of rat bone marrow stromal cells by various intensities of low-intensity pulsed ultrasound.* Ultrasonics, 2011. **51**(3): p. 281-288.

10. Takayama, T., et al., *Low-intensity pulsed ultrasound stimulates osteogenic differentiation in ROS 17/2.8 cells.* Life Sciences, 2007. **80**(10): p. 965-971.

11. Einhorn, T.A., *ENHANCEMENT OF FRACTURE-HEALING.* Journal of Bone and Joint Surgery-American Volume, 1995. **77A**(6): p. 940-956.

12. Mortazavi, S.M.J., S.A.R. Mortazavi, and M. Paknahad, *Mode & mechanism of low intensity pulsed ultrasound (LIPUS) in fracture repair.* Ultrasonics, 2016. **71**: p. 142-142.

13. Baker, K.G., V.J. Robertson, and F.A. Duck, *A review of therapeutic ultrasound: Biophysical effects.* Physical Therapy, 2001. **81**(7): p. 1351-1358.

14. Mauney, J.R., et al., *Mechanical stimulation promotes osteogenic differentiation of human bone marrow stromal cells on 3-D partially demineralized bone scaffolds in vitro.* Calcified tissue international, 2004. **74**(5): p. 458-68.

15. Uddin, S.M.Z. and Y.X. Qin, *Enhancement of Osteogenic Differentiation and Proliferation in Human Mesenchymal Stem Cells by a Modified Low Intensity Ultrasound Stimulation under Simulated Microgravity.* Plos One, 2013. **8**(9).

16. Zhou, X., et al., *Improved Human Bone Marrow Mesenchymal Stem Cell Osteogenesis in 3D Bioprinted Tissue Scaffolds with Low Intensity Pulsed Ultrasound Stimulation.* Scientific Reports, 2016. **6**.

17. Grayson, W.L., et al., *Spatial regulation of human mesenchymal stem cell differentiation in engineered osteochondral constructs: effects of pre-differentiation, soluble factors and medium perfusion.* Osteoarthritis and cartilage, 2010. **18**(5): p. 714-23.

18. Horner, C.B., et al., *Magnitude-dependent and inversely-related osteogenic/chondrogenic differentiation of human mesenchymal stem cells under dynamic compressive strain.* Journal of tissue engineering and regenerative medicine, 2016.

19. Ranganathan, K., et al., *Heterotopic Ossification: Basic-Science Principles and Clinical Correlates.* The Journal of bone and joint surgery. American volume, 2015. **97**(13): p. 1101-11.

Appendix A Spectral Ultrasound Imaging (SUSI) Procedure

Materials

1% Agarose gel padded dish, 55MHz 707B Probe or 35MHz 708 probe, phosphate buffered saline (PBS) or culture medium

SUSI Imaging Procedure

1. Power the system (one switch behind the machine, and one on the left side) and log into VEVO system and open the software (software automatically loads)
2. Immerse probe in PBS in a large container with distilled water
3. Initialize probe, choose operator, create and name new experiment
4. In B-mode, set imaging power, frame rate, and FOV size (with SectorX and SectorY)
5. Make sure probe has enough space to move, and initialize 3D in B-mode
6. In Digital RF mode, set number of lines per frame (250), choose data collection ROI, and initialize 3D
7. Put agarose gel pad on the stage, carefully place samples in the dish, and immerse probe in the dish above the sample
8. Frame Images and 3D Images:
    a. B-mode, power 100%, cardiac mode, 8.99mm range, 0.032mm step size
    b. Adjust probe position such that sample surface is at 4.5mm, which is the focus of the probe
    c. Adjust FOV such that it covers the whole sample while remaining some space in case the samples are different in size.
    d. Move the stage to image one end of the sample, note the reading of distance
    e. Image and store several frames of the sample, use “Scan/Freeze” to image and pause, use “Frame Store” to store frames
    f. Adjust sample position to be in the center of the scan range
    g. make sure the range covers the whole sample and Start 3D
    h. Save image using “Cine Store”

9. RF Data:
    a. “Mode” -> “Digital RF Mode”
    b. Adjust the red box in the image region, so it covers the whole sample and the agarose gel pad
    c. Adjust Settings: Power, 250 lines/frame, 3D mode, 8.99mm range, 0.2m step size (for example)
    d. Check by taking one frame at the center position, then look at different A-lines, check if the signal is saturated
    e. Start scan
    f. Save data using “Cine Store”

10. Attenuation Measurements
    a. In digital RF mode, uncheck 3D scan.
    b. Change frame number to 1.
    c. Move the transducer so that it focuses somewhere close to the agarose gel pad surface. Here, the agarose gel surface is set to be around 4.5mm from the probe.
    d. Adjust position of sample, choose a position at which there's some spacing between sample and agarose gel, and signal at the agarose gel surface is detectable in the image. Acquire one frame. Save using "Frame Store".
    e. Introduce water flow using a spatula or plastic syringe to move the sample out of FOV. Acquire one frame of the agarose gel pad without sample as reference. Save using "Frame Store".
    f. Repeat d & e to get total of 3 sets of measurements.

11. Before moving onto next sample, browse collected data, make sure several B-mode frames, 3D, digital RF, and 3 measurements of attenuation have been acquired and stored.
12. Repeat step 7-11 for all samples.
13. Store samples in PBS and put in the fridge with clear labels (name of sample, initials & date).
14. Fill agarose gel padded dish, wrap with parafilm, and store in fridge for future use.
15. Export images (in .tif for B-mode and .rdb for digital rf data); Or copy the VEVO file for the whole study from "E:\VEVO Data\ Permanent Study\" to a flash drive and work offline.

SUSI Data Analysis

1. Copy Vevo file into the VEVO system directory in "C:\Programs\Vevo\Permanent Study\"
2. Create subfolders under a parent folder for the study for Attenuation, RF Data, Exported Images, Analysis, Analysis Results, and empty folders for Control and Tumor, Sample, Attn (for attenuation data only).
3. Connect the VEVO toggle drive, open VEVO 770 software.
4. Label 3D images using "Image Label" function.
5. Label RF images as "sample_name_RF".
6. Label attenuation measurements as "sample_name_attn1" and "sample_name _attn1_ref", etc.
7. Export 3D rendered images:
    a. Open 3D image, "set-up" -> "3D mode"
    b. Check "rendered" and then "rendered". Choose to display one angle in the window.
    c. Save the 3D window image with proper sample name as tiff in "Exported Images"
    d. Change to front view, save the window image
    e. Repeat the same procedure for 3D images of all samples.
8. Export RF-data:
    a. Select a RF image without opening the file, click "Export Image" on top of the interface, export as "sample_name_RF" in rdi/rdb files to RF Data\ SampleFolder
    b. Do the same for other samples;
9. Export Attenuation Data
    a. Select an image without opening an image, export as rdi/rdb files into Attenuation\Sample1\Attn1 with name "sample_name_attn1".

    b. Save the corresponding reference image data in the same directory with name "sample_name_attn1_ref".
    c. Do the same for all other attenuation data.
10. Copy "Analysis" folder from last time. It has MATLAB scripts "UltraView", "attenuation_analysis", "surface-contour", "SUSI_analysis", "write_data_to_spreadsheet" and "data_summary".
11. Open "gi_gui.m" in MATLAB, run the script, preprocess all the rdi/rdb files exported from VEVO 770.
12. Load Calibration data. Here since RF data are collected with probe 707 with 50% power. Load "707-P50-B1-R5" from calibration folder. Display Aline 50. Find the time interval for the agarose gel signal. Here it's 1.43 to 1.52. This is useful for SUSI analysis.
13. Attenuation analysis. Open "Attenuation Analysis.m". change the directory, filename if necessary. Run the script and record attenuation values and speed of sound values in a spreadsheet.
14. Open "Surface_contour.m" and "SUSI_Analysis.m". Run "surface_contour" to draw contours around the sample. Remember the frames to be analyzed and corresponding A-line ranges, and copy the information into "SUSI_analysis.m"
15. Change the calibration file and type in "SUSI_ analysis.m". First set "ip.ImageOvelayChk" to 0. Run the script to analyze all RF data.
16. The slope, mbf, asd, aac values will be saved to "parameters.mat"
17. Open "write_to_spreadsheet.m" and adjust spreadsheet cell number according to fame number. Run the script to export parameter values to spreadsheet.
18. Run "data_summary.m" to read parameter values from spreadsheet and make plots.
19. Adjust ranges for the four parameters in "SUSI_analysis" and run the script again with "ip.ImageOverlayChk" = 1, and "ip.MustEvalChk" = 0 to save parametric images.
20. Summarize results in a presentation with 3D and B-mode images and representative parameter-overlaid images.

Appendix B Multimode Ultrasound Viscoelastography (MUVE) Procedure

1. Instrument set- up:
   A. BNC Model 565 Pulse/Delay Generator
      a) Channel A (HIFU Pulses)
         i. Enabled, Sync Source: To, Width: 0.99s, Delay:0
         ii. Pol: Active High, Out: TTL/CMOS
         iii. Mode: Burst, Burst: 180 Pulses
         iv. Gate: Disabled, Wait: 20 Pulses
         v. Ch: -DCBA-, Mux: -0001-
      b) Channel B (Imaging)
         i. Enabled, Sync Source: To, Width: 0.96s, Delay 0.015s
         ii. Pol: Active High, Out: TTL/CMOS
         iii. Mode: Burst, Burst: 200 Pulses
         iv. Gate: Disabled, Wait: 0 Pulses
         v. Ch: -DCBA-, Mux: 0010
      c) Sytem Settings
         i. Mode: Burst, Burst: 220 Pulses
         ii. Rate: per 1s
         iii. Gate/TRIG: Disabled, Level: 1V
   B. Function Generator Agilent 33220A (for Imaging)
      a) Pulse: 50Hz, 3Vpp, 0 offset, 20us width, 5ns edge time
      b) Burst: Externally triggered on rising edge, Gated, Neg
   C. Function Generator Agilent 33250A (for Pushing)
      a) Sine: 2MHz, 60mVpp, 0 offset,
      b) Burst: Externally triggered on rising edge, Gated, Pos
   D. Panametrics-NDT Model 5900PR 200MHz computer controlled Pulser/Receiver (for Imaging)
      a) Mode: P/E
      b) PRF: EXT-BNC
      c) Energy: 32uJ
      d) Damping: 50 Ohm
      e) HP FILT = 1 kHz
      f) LP FILT = 50 MHz
      g) ATTENUATORS = 00.0 dB
      h) GAIN: 54.0 dB
      i) RF OUTPUT PHASE= 180
   E. Agilent infiniuum 54830B DSO Oscilloscope (when acquiring data)
      a) Window: 700ns, 72.5us (adjustable)
      b) Segmented, 250 MSa/s, adjust segment number to ensure complete capture of segments

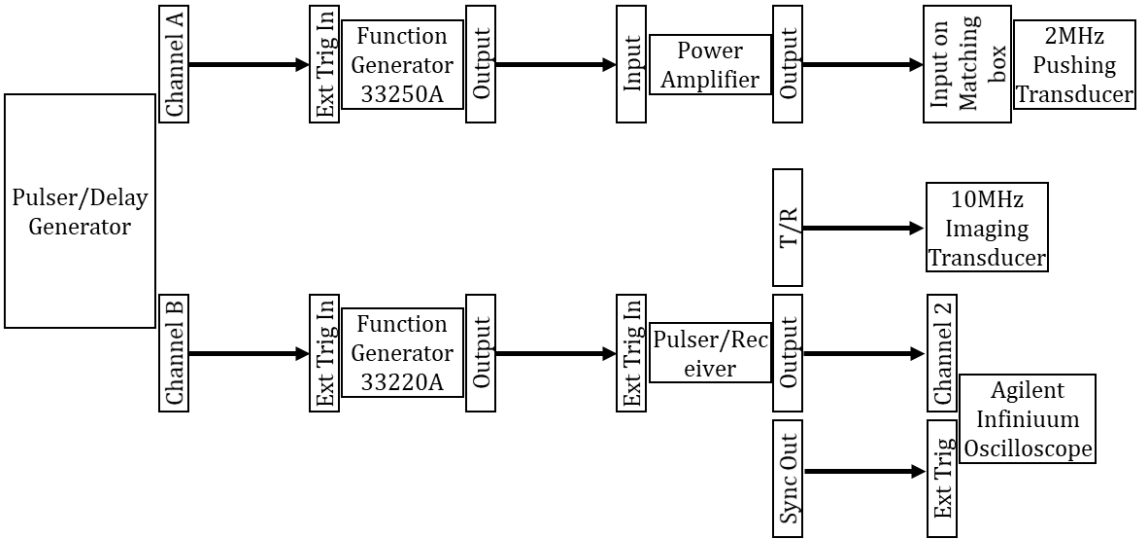

Figure B-1. MUVE system setup.

2. Alignment of Transducers**:** Set needle on 3D stage, make sure everything is level, and move needle with velmex control box to somewhere near the focus of the Pushing/Imaging transducer
3. Set Energy on Pulser/Receiver to 1uJ. Connect Pushing transducer (2MHz black annular transducer) to Pulser/Receiver T/R terminal
4. Turn PRF on Pulser/Receiver to 200Hz.
5. Adjust position of the needle using MATLAB script "Velmex.m" to move needle to the focus of the HIFU transducer. Focus of Pushing transducer is at 85us round trip. V_max ~ 2.1Vpp.
6. Turn PRF back to "EXT-BNC" and disconnect pushing transducer
7. Connect Imaging transducer to Pulser/Receiver T/R outlet, set energy to 32uJ. Adjust transducer position to focus at the needle. Imaging transducer focuses at 70us. V_max ~ 5.1Vpp.
8. Turn PRF back to "EXT-BNC" and disconnect imaging transducer.
9. Connect pushing transducer to Pulser/Receiver and double check the needle is still at Pushing transducer focus
10. Turn PRF back to "EXT-BNC", disconnect pushing transducer, and connect the imaging transducer to Pulser/Receiver
11. Move the needle out of the tank.
12. After imaging the sample with Vevo, place sample in the agar gel holder. Mount holder with sample on 3D motor. Slowly immerse the sample holder into water.
13. Move sample to the focus of the imaging transducer, and scan around to localize the sample center.
14. Pick a location to test. Set sample surface at 70us away with respect to the imaging transducer (round trip).
15. Adjust oscilloscope time and amplitude window to capture the whole sample. Also change the center of the time window to see the whole sample.

16. On oscilloscope, “System” -> “Acquisition”, change the acquiring mode to “Segmented”, Sampling Rate should be set to “250MSa/s”. Set # of segment to 1, and read the Points per segment. Increase the # of segments without losing the points per segment.
17. Turn Pulser/Receiver “PRF” to “Ext-BNC”.
18. Change the trigger setting on function generator for imaging to “N Cycle” and then switch back to “Gated”. This will reset the function generator triggering.
19. On oscilloscope, click “Control” -> “Run”.
20. On the Pulse/Delay Generator, press “Run|Stop” button.
21. Once acquiring data, #of segments on oscilloscope should increment by 2 every second till the pushing finishes. Then it will increment by 50 per second.
22. After acquisition, play the sequence and make sure interference occurs for the right segment number. Also check if there’s big difference between before and after.
23. If the interference occurred at the right timing, and no significant shift in sample location was observed, on oscilloscope: “File” -> “Save” -> “Waveform”. Name your dataset and save the data.
24. Repeat step 14 to 23 and test multiple locations in each sample. Save waveform after checking.
25. Once all data sets are collected, move sample outside the tank. Properly dispose or store sample. Wash the sample holder with bleach, and store water bath at room temperature. Turn off all instruments and Velmex. Remove water from tank so that the transducers are not soaked in the water over long period of time.